Experimental Investigation of Magnetic and Dielectric Properties of Metal Oxides

Thesis Submitted For The Degree Of

DOCTOR OF PHILOSOPHY (SCIENCE)

of

Jadavpur University

2023

By

Neepamala Giri

Department of Physics,

Jadavpur University,

Jadavpur, Kolkata - 700 032, India

JADAVPUR UNIVERSITY
JADAVPUR, KOLKATA-700032
INDIA

From: Prof. Ruma Ray
Professor
Department of Physics

Certificate from the Supervisor(s)

This is to certify that the thesis entitled "**Experimental Investigation of Magnetic and Dielectric Properties of Metal Oxides**" Submitted by ~~Sri~~ / Smt. **Neepamala Giri** who got ~~his~~ / her name registered on **15/04/2016** for the award of Ph. D. (Science) degree of Jadavpur University, is absolutely based upon his own work under the supervision of **Prof. Ruma Ray** and that neither this thesis nor any part of it has been submitted for either any degree / diploma or any other academic award anywhere before.

Ruma Ray 27.03.2023
(Ruma Ray)

(Signature of the Supervisor(s) date with official seal)

Dr. Ruma Ray
Professor
Department of Physics
Jadavpur University
Jadavpur, Kolkata-700 032

Dedicated to my parents……

Acknowledgement

Moments are significant not by the actual time but by their effect on us. My PhD journey is one of my memorable moments in my life. Although it has a complicated history, its trajectory has enriched my confidence. Along with good and bad experiences, I have grown more sensible, confident and vulnerable too. Apart from the confession part of my PhD journey, I have had the opportunity of meeting people who have left significant footprints on memory and knowledge. This thesis is a vestige of the unwavering support and encouragement from all of them, near and dear to me. Reaching at the edge of this journey, it is the ideal time to express my debts of gratitude to them for the support that I have received throughout my PhD journey.

First and foremost I would like to express my deep gratitude and sincere thanks to my supervisor, Prof. Ruma Ray for her valuable guidance, constant supporting and continuous encouragement throughout the course of my work. I am grateful to her for accepting me into her group and giving me the chance to prove myself in my crisis period. Apart from this, her way of training in the field of experimental condensed matter physics boost me to carry out my research work smoothly and successfully. Her enthusiasm, wide knowledge, evaluation efficiency and logical way of thinking have been great value for me. Her rich experience shaped the course of the research and sharpen its outcome.

I would like to convey my thankfulness and gratitude to Prof. Debnarayan Jana, Department of Physics, Calcutta University, Kolkata, for his selfless suggestions to achieve this stage of life.

I would like to thank Prof. Sourav Giri, Department of Solid State Physics, Indian Association for the Cultivation of Science, Kolkata, for his valuable advices and for giving me the opportunity to work in his research laboratory to carry out some of my experimental measurements.

I want to thank Koushik da, Ankita di, Alorika, Joyjeet, Tamal, Pradeepta and Sameek from Indian Association for the Cultivation of Science for helping me in my experimental works and their valuable suggestions out of their valuable time throughout my work. I express my warm and very special thanks to my labmates: Sanchari di, Archita di, Banhishikha, Payel and Simantini for their harmonic co-operation towards me. Apart from my own lab, I also thank all of my friends and seniors in other physics research labs in Jadavpur University. I would like to extend my thanks to all faculties and staffs of the Department of Physics, members of research section and Ph.D cell in Jadavpur University for various assistance and support. I would like to thank DST, Govt. of India for developing instrumental

facilities like Advance X-ray powder diffractometer (Bruker D8) and 7 T CFMS Mini VSM under FIST and DST PURSE II programme, respectively, at Jadavpur University and for INSPIRE Fellowship Scheme. I would like to acknowledge the SERB, DST, India for financial support in some of our experiments.

It is my pleasure to express my gratitude to Kalipada Da, from Seth Anandram Jaipuria College and Srijit Da, from Barasat Govt. College for their unconditional support and rich suggestions to complete my work.

A special dedication goes to my beloved husband, Dr. Balaram Dey for being my friend, philosopher and guide. Words cannot express my gratitude to him for holding me in so many ways from the very beginning. His invaluable advice and feedback on my research and continuous support have carried a great value to me.

My deepest gratitude and love from my heart to my grandfather Prof. Umakanta Giri, may he rest in peace. Without his guidance and motivation to take admission for Physics (Hons), I would not have been where I am today. Here I also want to express my heartiest gratitude to my teacher and second father, Mr. Amulya Kumar Jana who built the basic building block of my academic journey by very slow degrees. I am indebted to all my teachers for giving me the knowledge as forage of my life.

I would like to thank my lovely sister, Neela for her supporting in my research even being a student of different subject. I want to thank Moumita, Bhargabi, Datta da, Ritu, Sangita, Sulagna, Sritama and all of my friends for being in my life as my strength.

I would like to express my gratitude to my parents for their blessings in fulfilling my dream. I thank to my father, Dr. Nirmal Kr. Giri, for his implacable struggle and selfless sacrifices to make me educated in proper sense. This thesis will be incomplete if I not mention the name, Mrs. Sipra Giri, my mother and my best friend. There is lack of words to express my deepest honour and love towards her. She is the one who taught me the alphabets as well as the moral values of life. Her aspect towards life makes me enriched. From birth to all my achievements of my life would be impossible without her sacrifices and willing to see the world through my eyes. Thank you Maa, for sharing my sorrows, frustrations and healing them up by your love and care. I would like to extend my gratitude to my other family members, parents-in-laws and other in-laws family members for their endless support and love.

Finally, I would like to express my deepest appreciation to my beloved son "Naimesh", who is the source of my internal energy for the last two years. He

has given me the strength and encouragement throughout the challenging moments of completing my research work during the last two years.

I equally convey my gratitude to all of them, whom I cannot mentioned here due to the constraint of space, for their valuable assistance in this long journey.

I express my gratitude to the authors whose research reports provided fertile territory into which I ventured to gather material for this thesis. I am indebted to several people, some anonymous, who read this manuscript and made helpful suggestions.

Jadavpur University

Kolkata

March, 2023

Neepamala Giri 27/03/23

(Neepamala Giri)

Synopsis

Metal-oxides are drawing considerable attention of researcher and have been applied in diverse fields of applications because of their various properties, such as dielectrics, ferroelectricity, magnetism, superconductivity, optical spectroscopy, light emission, etc. Particularly, oxides of transition metals and rare earths display a very wide variety of complex structures and interesting properties. The conductivity of such oxides can vary from insulator to semiconductor to conductor. By suitable doping, their electronic and magnetic properties can be tailored and made them suitable for required applications such as smart sensor, energy storage, data storage, etc. Furthermore, nanostructured metal oxides such as nanoparticles and thin films are known to exhibit superior physical, chemical, mechanical and thermal properties as compared to the bulk materials, which make the nanophase structures indispensable tools in modern nanotechnology. The key to its applications demands the fundamental understanding of structural, electronic, dielectric, and magnetic properties.

The exchange bias (EB) phenomenon, which becomes an integral part of modern magnetism, has generated a growing interest in the scientific community due to its potential technological value. Since its discovery, several investigations on this phenomenon have been performed in many different systems such as ferromagnetic (FM) films on antiferromagnetic (AFM) single crystals and thin films, thin AFM-FM bilayer, multi-layered, core-shell structure of AFM oxide

nanoparticles, mixed-valent perovskites, etc. A large number of applications of these materials in advanced magneto-electronic devices such as hard disk drive, magnetic sensors, magneto resistive random access memory have gained much attention of researchers in recent days. In addition, there is the growing need of increasing the storage capacity of the magnetic material within a small volume as well as cost-effectiveness. The granular and epitaxial films can be used to fulfil the growing needs of memory and size reduction of magnetic recording media. However, the studies of EB effect on granular film are not much reported in existing literature. On the other hand, a hole doped perovskite cobaltates, is an another class of materials in which EB effect has been less studied compared to other manganites like $La_{1-x}Sr_xMnO_3$ (LSMO), $La_{1-x}Ca_xMnO_3$ (LCMO), etc., and cobaltates like $La_{1-x}Sr_xCoO_3$ (LSCO), $La_{1-x}Ca_xCoO_3$ (LCCO), etc. In this thesis work, therefore we have concentrated on such materials like nickel oxide (NiO) granular film, Zn doped NiO ($Ni_{1-x}Zn_xO$) ($0 \leq x \leq 0.05$) film and Sr doped $NdCoO_3$ polycrystalline nanoparticles to investigate the EB phenomena.

Granular NiO and $Ni_{1-x}Zn_xO$ film are prepared by sol-gel dip-coating technique on a silicon wafer substrate. Detailed structural investigations and the surface topology of both films have been performed by X-ray diffraction (XRD) and atomic force microscopy (AFM), respectively. For NiO film, a broad peak around temperature T=156 K is observed in the thermal variation of zero field cooled (ZFC) magnetization measured in 500 Oe magnetic field. Both the field cooled (FC) and ZFC magnetizations display a significant rise with decreasing

temperature at T < 25 K indicating the existence of a ferromagnetic (FM) component, possibly due to the uncompensated (UC) spins residing at the grain boundaries. The systematic and significant shifts in the magnetic hysteresis (MH) loops, known as EB effect, are observed when the sample is field cooled. For $Ni_{1-x}Zn_xO$ film, the magnetization measurement reveals the blocked state of $Ni_{0.95}Zn_{0.05}O$ below the temperature of 155 K, while the uncompensated spin is inferred for $Ni_{0.97}Zn_{0.03}O$ from the low temperature up-turn of the magnetization. A systematic shift of MH loop (EB effect) is also observed in field cooled mode in case of $Ni_{1-x}Zn_xO$ film and found to be strongly dependent on *x*. It should be mentioned that the pinning mechanism at the interface between antiferromagnetic core and the shell consisting of uncompensated spins leads to the EB effect in both the granular films.

The polycrystalline $Nd_{0.78}Sr_{0.22}CoO_3$ (NSCO) nanoparticles having 89 nm average particle size are synthesized by standard sol–gel techniques. Structural and morphological characterization is performed by X-ray diffraction and FESEM images. The magnetic properties such as magnetization, coercivity and EB phenomena in $Nd_{0.78}Sr_{0.22}CoO_3$ are investigated using commercial vibrating sample magnetometer (VSM). DC magnetization studies in the range 1.6 K to 300 K reveal the disordered magnetic phase below 36 K. Existence of this disordered magnetic phase is substantiated by the magnetic memory effect. A significant upturn in the ZFC magnetization below 4.5 K, signature of a dominant ferromagnetic (FM) component, is observed. This FM component may be

attributed to the uncompensated (UC) spins at the surface of $Nd_{0.78}Sr_{0.22}CoO_3$ nanoparticles. The presence of the interface of these two magnetic components with significantly different anisotropy results the exchange bias effect.

In addition, we have also focused on semiconducting oxide nanomaterials because of their novel optical, electrical and catalytic properties. Dielectric and transport properties of the semiconducting nanomaterial can be tuned by incorporating different dopant. Materials with a high dielectric constant play critical roles in a wide range of electronic applications and they can be used in high efficiency energy storage devices. The implementation of materials with such high dielectric constant is one of the several strategies developed to allow further miniaturization of microelectronic components, which is essential for the new generation devices in several applications such as medical electronics, space electronics, etc. Therefore, the requirement of materials with high dielectric constant in the field of microelectronics prompts us to study the transport and dielectric properties of materials. In this thesis work, the transport and dielectric properties of Al doped ZnO (AZO) and Zn doped NiO ($Ni_{1-x}Zn_xO$) (with $0 \leq x \leq 0.05$) nanoparticles have also been studied. Both the samples have been synthesized using chemical precipitation method with different doping concentrations. $Ni_{1-x}Zn_xO$ sample has been characterized by means of XRD method, FE-SEM and Transmission Electron Microscope (TEM), while AZO sample has been characterized by means of XRD method and FE-SEM.

In case of $Ni_{1-x}Zn_xO$ sample, the sizes of nanoparticles are calculated as 26 and 22 nm for x = 0.0 and 0.05, respectively. The optical band gap increases regularly with doping concentration (x), which is consistent with the particle size variation. It is observed that the dielectric constant (ε_r) increases gradually with x at high frequency (~ 2 MHz). The dc conductivity (σ_{dc}) is found to decrease with increase in Zn^{2+} doping at room temperature, which may be attributed to the reduction of oxygen vacancy via defect compensation mechanism. Temperature variation of σ_{dc} reveals the semiconducting nature with activation energies (E_a) of 110.2 meV for x = 0.0; 384.14 meV and 88.19 meV in the temperature range 303-383 K and 383-423 K, respectively, for x = 0.05. In case of AZO sample, dielectric constant (ε_r) and dielectric loss (tan δ) of $Zn_{1-x}Al_xO$ ($0 \leq x \leq 0.1$) are measured as a function of frequency (f) and doping concentration (x) at room temperature.

In summary, significant exchange bias effect and the variation of exchange bias field (H_E) with both the temperature as well as cooling field, have been identified in the granular polycrystalline NiO and $Ni_{1-x}Zn_xO$ film. An interesting phenomenon of EB effect has been explored in the hole doped cobaltates $Nd_{1-x}Sr_xCoO_3$ nanoparticles. These could aid a lot to the development of magnetic electronics. Besides, the enhancement of dielectric constant accompanied by the reduction in dielectric loss due to Zn doping in NiO nanoparticles makes $Ni_{0.95}Zn_{0.05}O$ a potential candidate for energy storage device. In addition, in case of Al doped ZnO nanoparticles, 3% Al is found to be the optimum dopant concentration for which dielectric constant becomes maximum. It is also found

that the dielectric constant of AZO nanoparticle decreases beyond 3% Al doping concentration indicating the importance of dopant concentration on the enhancement of dielectric constant, which is an essential information for the miniaturization of several microelectronic components in near future.

List of Publications

Thesis Related Publications

i. "Exchange bias and magnetic memory effect in hole doped $Nd_{0.78}Sr_{0.22}CoO_3$ nanoparticles", **N. Giri,** B. Biswas, P. Sengupta and R. Ray, Royel Society of Chemistry in Advance, 2022, 12, 26470–26475.

ii. "Doping Induced Dielectric and Transport Properties of $Ni_{1-x}Zn_xO$", **N. Giri,** A. Mondal, S.Sarkar and R. Ray., Journal of Materials Science: Materials in Electronics, 2020, 31, 12628-12637 .

iii. "Doping induced tailoring of exchange bias effect in granular $Ni_{1-x}Zn_xO$ film", **N. Giri,** S. Das, S. Sarkar, A. Mondal, S. Giri and R. Ray., Physica B : Condensed Matter, 2019, 570, 229-231.

iv. "Uncompensated grain boundary spin driven exchange bias effect in granular NiO film", S Das, **N. Giri,** S Sarkar, A Mondal, S Majumdar, S Giri and R Ray., Solid State Communication, 2019, 298, 113642.

v. "Structural and dielectric properties of $Zn_{1-x}Al_xO$ nanoparticles", **N. Giri,** A Mondal, S Sarkar and R Ray., AIP Conference Proceedings, 2018, 1953, 050011.

Others Publication

i. "Enhanced photocatalytic activity and enormous dielectricity of α-Fe_2O_3/reduced graphene oxide nanocomposites", S.Sarkar, **N.Giri,** A.Mondal, S. Sarkar and R. Ray, Indian J. Phys, 2019, 93, 449–458.

List of Publications

ii. "Spin glass like transition and exchange bias effect in Co_3O_4 nanoparticles anchored onto graphene sheets", S. Sarkar, A. Mondal, **N. Giri** and R. Ray, Physical Chemistry Chemical Physics, 2019, 21, 260 – 267.

iii. "Tuning the photocatalytic activity of ZnO by TM (TM = Fe, Co, Ni) doping", A. Mondal, **N. Giri,** S. Sarkar, S. Majumdar, R. Ray, Materials Science in Semiconductor Processing 2019, 91, 333– 340.

iv. "Facile Synthesis of Ni/NiO@GO Nanocomposites and its enhanced dielectric constant", S. Sarkar, **N. Giri,** A. Mondal and R. Ray, AIP Conference Proceedings, 2018,1953, 050016.

v. "Magnetic Properties of $Zn_{1-x}Ni_x$", A. Mondal, **N. Giri,** S. Sarkar and R. Ray, AIP Conference Proceedings, 2018, 1953, 120017.

vi. "Magnetic phase separation in diluted magnetic system: $Zn_{1-x}Fe_xO$", A. Mondal, S. Sarkar, **N. Giri** , S. Chatterjee and R. Ray., Acta Metall. Sin., 2017, 30(6), 521-527

Table of Contents

Table of Contents

Table of Contents

Table of Figures

Table of Figures

Table of Figures

Chapter 1

1 Aims and Alignments of Thesis

1.1 Motivation and Research Objectives

Exchange bias (EB) effect, an intriguing phenomenon in magnetism, has become an integral part of the research and development in modern treatment of magnetism due to its potential application in different fields of electronics, electrical engineering and magnetic devices. It triggers a significant attention owing to its applications in magnetic recording media [1], magneto-resistive sensors [2], spin valve devices [3], etc. It was first experimentally observed in 1956 by Meiklejohn and Bean in FM Co/AFM CoO core-shell nanoparticles [4, 5]. Since then avid research interest is seen in this topic. EB effect is basically a demonstration of the unidirectional anisotropy and indicated by the shift in magnetic hysteresis loop at low temperature. It arises due to pinning mechanism at the interface between two magnetic components containing significant difference in anisotropy [6]. Since its discovery, a large number of reports on EB effect are available in different systems such as FM films on AFM single crystals [7-8] and thin films [9-13], thin AFM-FM bilayer [6], multi-layered [14], core-shell structure [15], AFM oxide nanoparticles [16-18], etc. However, there is a growing need of increasing the storage capacity of the magnetic material within a small volume as well as cost-effectiveness. The granular and epitaxial films can be used to fulfil such growing needs of memory and size reduction of magnetic

recording media. However, the studies of EB on granular film (such as NiO, $Ni_{1-x}Zn_xO$) are not much reported in existing literature.

The hole doped perovskite manganites and cobaltates are another class of materials, which are the potential candidates in order to explore the abundant interfacial magnetic phenomena. Examples of such manganites and cobaltates materials are $La_{1-x}Sr_xMnO_3$ (LSMO), $La_{1-x}Sr_xCoO_3$ (LSCO), $La_{1-x}Ca_xCoO_3$ (LCCO), $Nd_{1-x}Sr_xCoO_3$ (NSCO), etc. An interesting phenomenon of exchange bias (EB) effect is the spontaneous phase separation, which has been explored in such hole doped perovskite manganites and cobaltates [19-28]. However, the EB effect is less studied in NSCO system [29-31] compared to the other manganites and cobaltates. Furthermore, the study on NSCO system is highly imperative to promote the potential applications in permanent magnet and high density magnetic storage device. In this thesis work, we have focused on these three systems (granular NiO film, $Ni_{1-x}Zn_xO$ film and NSCO) to investigate experimentally the EB phenomena. Furthermore, the objectives of the present thesis work are to offer a fundamental background of magnetic properties like EB effect, magnetic memory effect, and magnetization along with structural and morphological characterizations. This investigation could help us to find suitable materials in the development of magnetic electronics in near future [32].

Besides, the requirement of materials with high dielectric constant in the field of microelectronics prompts us to study dielectric properties of materials. The

materials with high dielectric constant could have the high capacitance and thereby, can store the maximum energy within a small volume element. Thus, the implementation of materials with high dielectric constant is one of the several strategies developed to allow further miniaturization of microelectronic components, which is essential for the new generation in several applications such as medical electronics, space electronics, etc [33]. Therefore, in addition to the magnetic properties, we have also focused on the transport and dielectric properties of semiconductor metal oxides nanoparticles. Recently, nanostructured semiconductor metal oxides are gradually attracting attention because of their fascinating electrical and optical properties [34-35]. Such semiconductor metal oxide nanoparticles (CuO, TiO_2, SnO_2, NiO, ZnO, etc.) have many areas of potential applications like spintronics devices, solar cell, gas sensors, etc [36-37]. Among these, NiO nanomaterials attract huge attention of researchers due to their excellent thermal stability that makes them suitable for microelectronics applications [38]. Furthermore, ZnO nanoparticle is another promising semiconductor having applications in optoelectronics devices due to their wide band gap [39]. In order to improve the electrical and optical properties of metal oxide semiconductors, doping is one of the effective method [40]. Conductivity as well as optical transparency of ZnO can be tailored by doping with extrinsic n-type dopants like Al, Ga, B, In [41-45]. On the other hand, doping of transition metals into NiO nanoparticles appraises the chance of being parasitic material for

several applications [46]. Therefore, we have focused on doped zinc oxide and nickel oxides, namely $Zn_{1-x}Al_xO$ ($0 \leq x \leq 0.1$) and $Ni_{1-x}Zn_xO$ ($0 \leq x \leq 0.05$) nanoparticles and our endeavour is to explore the structural, morphological, optical and transport properties of them.

1.2 Outline of Thesis

This thesis is organized as follows:

Chapter 1 contains the research motivations and outline of thesis.

Chapter 2 gives an introduction to the background of our research topic.

Chapter 3 contains the brief description of our studied samples.

Chapter 4 describes the experimental techniques, principles and measurements used in our work.

Chapter 5 represents exchange bias effect in granular NiO film due to uncompensated grain boundary spin along with the structural details of sample.

Chapter 6 describes structural characterization and exchange bias effect in granular $Ni_{1-x}Zn_xO$ film depending on doping concentration.

Chapter 7 provides the investigation on dielectric and transport properties of $Ni_{1-x}Zn_xO$ nanoparticles.

Chapter 8 presents the study on structural and dielectric properties of $Zn_{1-x}Al_xO$ nanoparticles.

Chapter 9 presents the exchange bias and magnetic memory effect in hole doped $Nd_{0.78}Sr_{0.22}CoO_3$ nanoparticles.

Chapter 10 describes the general conclusions of this thesis.

1.3 References

1. A. A. Glazer, A. P. Potapov and R. I. Tagirov, Sov. Phys. JETP. Lett., 15 (1972) 259.
2. L. Jogschies, D. Klaas, R. Kruppe, J. Rittinger, P. Taptimthong, A. Wienecke, L. Rissing and M.C. Wurz, Sensors, 15 (2015) 28665.
3. J. Nogués, J. Sort, V. Langlais, V. Skumryev, S. Suriñach, J. S. Muñoz and M. D. Baro, Phys. Rep., 422 (2005) 65.
4. W. H. Meiklejohn and C. P. Bean, Phys. Rev., 102 (1956) 1413.
5. W. H. Meiklejohn and C.P. Bean, Phys. Rev., 105 (1957) 904.
6. J. Nogués and I. K. Schuller, J. Magn. Mater., 192 (1999) 203.
7. T. J. Moran, J. M. Gallego and I. K. Schuller, J. Appl. Phys., 78 (1995) 1887.
8. A. E. Berkowitz and J. H. Greiner, J. Appl. Phys., 36 (1965) 3330.

9. Review: C.P. Bean, in: C.A. Neugebauer, J.B. Newkirk, D.A. Vermilyea (Eds.), Structure and Properties of Thin Films, Wiley, New York, 1960, p. 331.
10. Review: A. Yelon, in: M.H. Francombe, R.W. Hoffman (Eds.), Physics of Thin Films, vol. 6, Academic Press, New York, 1971, p. 205.
11. Review: AFM Properties: K. Fukamichi, J. Magn. Soc. Japan, 21 (1997) 1062.
12. R. Jungblut, R. Coehoorn, M. T. Johnson, J. aan de Stegge and A. Reinders, J. Appl. Phys., 75 (1994) 6659.
13. M. Takahashi, A. Yanai, S. Taguchi and T. Suzuki, Jpn. J. Appl. Phys., 19 (1980) 1093.
14. S. H. Lim, M. Murakami, S. E. Lofland, A. J. Zambano, L. G. Salamanca-Riba and I. Takeuchi, J. Magn. Magn. Mater., 321 (2009) 1955.
15. H. Al Chaghouri, F. Tuna, P. N. Santhosh and P. John Thomas, Solid State Commun., 230 (2016) 11.
16. S. A. Makhlouf, H. Al-Attar and R. H. Kodama, Solid State Commu., 145 (2008) 1.
17. T. N. Shendruk, R. D. Desautels, B. W. Southern and J. Van Lierop, Nanotech., 18 (2007) 455704.
18. Sk Sabyasachi, S. Majumdar and S. Giri, Solid State Commun., 151 (2011) 1515.

19. J. Wu and C. Leighton, Phys. Rev. B, 67 (2003) 174408.

20. J. C. Burley, J. F. Mitchell and S. Short, Phys. Rev. B, 69 (2004) 054401.

21. S. V. Trukhanov, M. V. Bushinsky, I. O. Troyanchuk and H. Szymczak, Journal of Experimental and Theoretical Physics, 99 (2004) 756.

22. M. Paraskevopoulos, J. Hemberger, A. Krimmel, and A. Loidl, Phys. Rev. B, 63 (2001) 224416.

23. K. Yoshii, A. Nakamura, H. Abe, M. Mizumaki, and T. Muro, J. Magn. Magn. Mater., 239 (2002) 85.

24. M. Patra, S. Majumdar, and S. Giri, J. Appl. Phys., 107 (2010) 033912.

25. K. P. Rajeev and A. K. Raychaudari, Phys. Rev., B 46 (1992) 1309.

26. P. Ganguly, N. Y. Vasanthacharya, C. N. R. Rao, and P. P. Edwards, J. Solid State Chem., 54 (1984) 400.

27. A. Maignau, C. Martin, M. Hervieu, and B. Raveau, Eur. Phys. J. B, 13 (2000) 41.

28. D. D. Stauffer and C. Leighton, Phys. Rev. B, 70 (2004) 214414.

29. A. Ghoshray, B. Bandyopadhyay, K. Ghoshray, V. Morchshakov, K. Bärner, I. O. Troyanchuk, H. Nakamura, T. Kohara, G. Y. Liu and G. H. Rao, Phys. Rev. B, 69 (2004) 064424.

30. Y. Yang, Chemical Engineering Transactions, 59 (2017) 961.

31. L. Zhang, X. Li, F. Wang, T. Wang and W. Shi, Materials Research Bulletin, 48 (2013) 1088.

32. H. Shirinova, L. D. Palma, F. Sarasini, J. Tirillo, M. Ramazanov, F. Hajiyeva, D. Sannino, M. Polichetti and A. Galluzzi, Chemical Engineering Transactions, 47 (2016) 103.
33. J. J. Licari and D. W. Swanson, Adhesives Technology for Electronic Applications (Second Edition), 2011, doi: 10.1016/B978-1-4377-7889-2.10005-1
34. M. Li, H. Bala, X. Lv, X. Ma, F. Sun, L. Tang and Z. Wang, Mater. Lett., 61 (2007) 690.
35. C. Wang, E. Shen, E. Wang, L. Gao, Z. Kang, C. Tian, Y. Lan and C. Zhang, Mater. Lett., 59 (2005) 2867.
36. K. Anandan and V. Rajendran, Nanosci. Nanotech., 2 (2012) 24.
37. C. Thangamani and K. Pushpanathan, J. Chem. Pharm. Sci., (2015) 111.
38. C. Thangamani and K. Pushpanathan, J. Chem. Pharm. Reseach, 8(8) (2016) 749.
39. M. Vadivel, R. R. Babu and K. Ramamurthi, Int. J. Chem Tech Res., 7(3) (2014) 1206.
40. D. Kohl, Sens. Actuators B, 1 (1990) 158.
41. T. Minami, H. Nanto and S. Takata, Jpn. J. Appl. Phys., 23 (1984) L280.
42. A. Sarkar, S. Ghosh, S. Chaudhuri and A. K. Pal, Thin Solid Films, 204 (1991) 255.

43. J. Steinhauser, S. Faÿ, N. Oliveira, E. Vallat-Sauvain and C. Ballif, Appl. Phys. Lett., 90 (2007) 142107.

44. V. Bhosle, A. Tiwari and J. Narayan, J. Appl. Phys., 100 (2006) 033713.

45. K. Das, P. Misra and L. M. Kukreja, J. Phys. D: Appl. Phys., 42 (2009) 165405.

46. J. Wang, L. Wei, L. Zhang, J. Zhang, H. Wei, C. Jiang and Y. Zhang, J. Mater. Chem., 22 (2012) 20038.

2 Introduction

Metal-oxides have drawn great attention of researcher and have been employed in diverse fields of applications because of their various properties, such as dielectrics, ferroelectricity, magnetism, superconductivity, optical spectroscopy, light emission, etc. Transition metal and rare earth oxides, in particular, exhibit a wide range of complicated structures and intriguing properties. Their electronic and magnetic properties can be tailored by appropriate doping and made them suitable for required applications such as smart sensor, energy storage, data storage, etc. Furthermore, nanostructured metal oxides such as nanoparticles and thin films are known to have superior physical, chemical, mechanical, thermal and biological properties as compared to the bulk materials, which make the nanophase structures indispensable tools in modern nanotechnology. The key to its applications in modern science and technology demands the fundamental understanding of structural, electronic, dielectric, and magnetic properties.

The development of modern science and technology would be hindered severely without the use of magnetic materials and devices. The history of magnetism dates back to as early as 800 BC, but scientists have started to realize and apply it in technological applications only since 18^{th} century. A chemical compound of iron and oxygen, known as loadstone, is the material in which magnetic property was observed for the first time. The magnetism develops in a magnetic material,

such as the earliest referred material loadstone, due to the electronic motion around the atomic nucleus as well as for the electronic spin. The magnetism draws significant attention owing to its stupendous application in human civilization. Electronics and electricity have been redefined due to the introduction of magnetic materials as key components in power supplies to be used in loudspeakers, earphones, motors, generators, and so on. However, a new dimension has been added up in the domain of magnetism, with the nobel prize winning discovery of giant magnetoresistance effect by A Fert and P Grünberg [1-2]. This has opened up a completely novel area of electronics, namely spintronics, characterized by the properties of spin and charge of the electrons [3-4]. Applications of this effect have revolutionized techniques for retrieving data from hard disks. It has also made the areas of magnetic recording, reading-writing head and storage devices in computers, audio-video systems as well as various magnetic sensors richer. Spintronics is such a flourishing field of science and technology that could become pioneer of all aspects of electronics in the near future.

GMR effect was first observed in a device containing an antiferromagnetic (AFM) conductive layer sandwiched between two soft ferromagnetic (FM) layers [1-2, 5]. One of these two FM layers is known as ‘pinned FM layer’ that kept contact with AFM layer and another one is ‘free FM layer’. It should be mentioned here that there is an exchange interaction between ‘pinned’ FM layer

and AFM layer, which makes the magnetization of 'pinned FM layer' fixed in particular direction. Because of this, the 'pinned FM layer' cannot respond to a magnetic field where the 'free FM layer' can. This exchange interaction results shifting and broadening of hysteresis loop of the FM/AFM systems, usually referred to as exchange bias (EB) effect [6-7]. Besides, the magnetization of 'free FM layer' can be oriented along parallel or antiparallel taking magnetization of 'pinned FM layer' as reference direction. The GMR effect is manifested by the difference in electrical resistance for parallel and antiparallel alignments of the magnetizations of two FM layers. Therefore, the exchange bias effect is the key element of all devices having FM/AFM layers with GMR.

In order to fulfil the modern integrated manufacturing needs of faster devices, the electrical properties of materials, along with the magnetic properties, have also triggered the attention of the researchers. One of the most important electrical properties is the dielectric properties of materials. Depending on these properties, various devices such as capacitors, microphones, ultrasonic generators, liquid crystal display, etc., can be fabricated. Recent progress in wireless communication technologies have grown interest in the materials having different unusual properties such as high dielectric constant, low dielectric loss and low values of temperature dependence of dielectric constant [8]. The materials with high dielectric constant could have the high capacitance and thereby, can store the maximum energy within a small volume element. Thus, the implementation

of materials with high dielectric constant could allow the further miniaturization of microelectronic components. Hence, it will not be exaggerated if advanced microelectronics is mentioned as the major reason behind the study of dielectric properties of materials.

The present thesis mainly consists of (i) magnetic properties such as exchange bias effect and magnetization of granular NiO and $Ni_{1-x}Zn_xO$ ($0 \leq x \leq 0.05$) film, polycrystalline nanoparticle $Nd_{0.78}Sr_{0.22}CoO_3$ and (ii) dielectric and optical properties of $Ni_{1-x}Zn_xO$ ($0 \leq x \leq 0.05$) and $Zn_{1-x}Al_xO$ ($0 \leq x \leq 0.1$) nanomaterials.

2.1 Magnetism

2.1.1 Historical Background

A mysterious phenomenon of attracting materials, lately known as Magnetism, was observed as early as 800 BC in a particular type of iron oxide, named Loadstone, in ancient Greece. The word "Magnetism" comes from the Greek word as loadstone was found in Magnesia, a district in northern Greece. Loadstone with its attracting properties was used for the first time for navigation purposes. It was in 1263, Pierre de Maricourt discovered two poles of the magnet during the mapping of loadstone using compass. Later in 1600, the Earth as a giant magnet was first discovered by William Gilbert. The beginning of an unprecedented era in science came through the concept of electromagnetism, first introduced by Hans Christian Oersted in 1820 and later explained by James Clerk

Maxwell in 19th century. Besides, Michael Faraday and Joseph Henry independently discovered the relationship between magnetic field and current. Faraday first invented generator and electric motor by experimental applications of electromagnetism. In the late 19th century, Pierre Curie proposed the dependence of magnetism on temperature, which prompted the researchers to the discovery of superconductivity. The contribution of superconductors in the field of magnetic levitation, quantum computers, magnetic sensor, transformer and generators and many more is undeniable in modern life. Therefore, the importance of magnetism in our daily life, not only on macroscopic scale like motor of washing machine but also on nano scale like hard disk of computer, makes it extremely rich application based scientific research domain.

2.1.2 Origin

According to the modern theories, the magnetism in solids originates due to orbital and spin motion of the electrons as well as spin of the nuclei. The motion of electron in an atom is equivalent to an electrical current loop creating a magnetic moment (μ). A number of such magnetic moments may align themselves in different directions to produce a net non-zero magnetic moment. It should be mentioned that the major contribution of magnetic moments comes from the spin of unpaired valence electrons. Depending on the alignment of those magnetic moments and the number of unpaired valance electron, the magnetism

in solids can be classified into different catagories such as diamagnetism, paramagnetism, ferromagnetism, anti-ferromagnetism and ferrimagnetism.

A solid gets magnetized in the presence of an external magnetic field and the resultant magnetic moment per unit volume developed inside the solid is called magnetization (M). The magnetization produced per unit external field is known as magnetic susceptibility (χ), which is a measure of the quality of the magnetic material.

$$\boldsymbol{\chi = M/H} \text{.....(2.1)}$$

where, H is the magnetic field intensity. A magnetic induction (B) will be produced inside the medium because of applied magnetic field and it is given as:

$$\boldsymbol{B = \mu_0(H + M) = \mu_0(1 + \chi)H} \text{ .....(2.2)}$$

$$\boldsymbol{\mu H = \mu_0(1 + \chi)H} \text{ .....(2.3)}$$

$$\boldsymbol{\mu = \mu_0(1 + \chi)} \text{.....(2.4)}$$

where, μ_0 and μ are the permeability of free space and medium, respectively. The value and sign of susceptibility is found to be different for different types of magnetism.

2.1.3 Classification

As discussed in the earlier section that there are different kinds of magnetism depending on the alignment of concerned magnetic moments and number of unpaired valance electrons, are shown in ***Figure 2.1*** and discussed as follow:

Diamagnetism, a very weak effect, is observed in solids such as ionic and covalent crystals with no unpaired electrons in atoms or ions. The diamagnetic behaviour is due to the changes in orbital motion of the electrons induced by the applied magnetic field. The induced magnetic moment is always directed opposite to the applied magnetic field resulting negative value of susceptibility ($\chi < 0$). Even though all materials are diamagnetic, often other forms of magnetism dominate over the observation of diamagnetism owing to the weak nature of the latter.

Paramagnetism is also a weak effect but, unlike diamagnetism, the magnetic moment is aligned along the field direction causing small but positive susceptibility ($0 < \chi << 1$). In the absence of magnetic field, randomly oriented magnetic moments causes no net magnetization. The presence of unpaired electrons in ions like transition and rare earth ions is mainly responsible for their paramagnetic behaviour.

Ferromagnetism is associated with the presence of permanent dipoles. Unlike para- magnetism, the magnetic moments of sub-lattices are aligned in a certain direction, resulting net non-zero magnetization, even in the absence of external magnetic field. This magnetization is known as spontaneous magnetization. It exists below a critical temperature, named Curie temperature (T_C), above which a ferromagnetic substance becomes paramagnetic due to its high thermal energy.

This is expressed by the Curie Weiss Law which connects the susceptibility (χ) and temperature (T).

$$\chi \propto \frac{1}{T-T_C} \quad \text{.....(2.5)}$$

For ferromagnetic (FM) material, χ possess large and positive value but it varies with field strength. The variation of magnetization with field strength exhibits the hysteresis curve, discussed later. On the contrary, when substance is kept below the T_C, the alignment of magnetic moments is controlled by exchange interaction between the spins of atoms. This interaction can be explained by Heisenberg model, where exchange energy between two atoms is shown by

$$U_{ex} = -2J_e\mu^2 cos\varphi \text{.....(2.6)}$$

J_e is the exchange integral, assumed to be same for any pair of atoms, φ is the angle between magnetic moments μ of interacting atoms. Generally, value of J_e depends on interatomic distance of atoms, positive for larger one and negative for smaller one. U_{ex} will be lower energy for positive J_e value with parallel arrangements of spins (φ=0), which favour magnetism. There are many elements like Ni, Co, Fe and a number of alloys and oxides such as MnBi, MnAs, CrO_2 which exhibit ferromagnetism.

Antiferromagnetism originates when spin moments of the neighbouring atoms are antiparallel. As the adjacent moments are equal and opposite to each other, the complete cancellation of moments results antiferromagnetic (AFM) order hard to detect experimentally. AFM materials can be considered as combination

of two equivalent ferromagnetic sub-lattices with opposite magnetization directions. In the absence of an external magnetic field, AFM materials exhibit no net magnetization. However, when a field is applied, a small magnetization appears in the direction of field which increases with increasing temperature. There is a characteristics temperature above which AFM order disappears and substance behaves as paramagnetic. This temperature is denoted as Neel temperature (T_N). Antiferromagnetism is exhibited by many compounds containing transition metals such as CoO, NiO, MnF_2, etc.

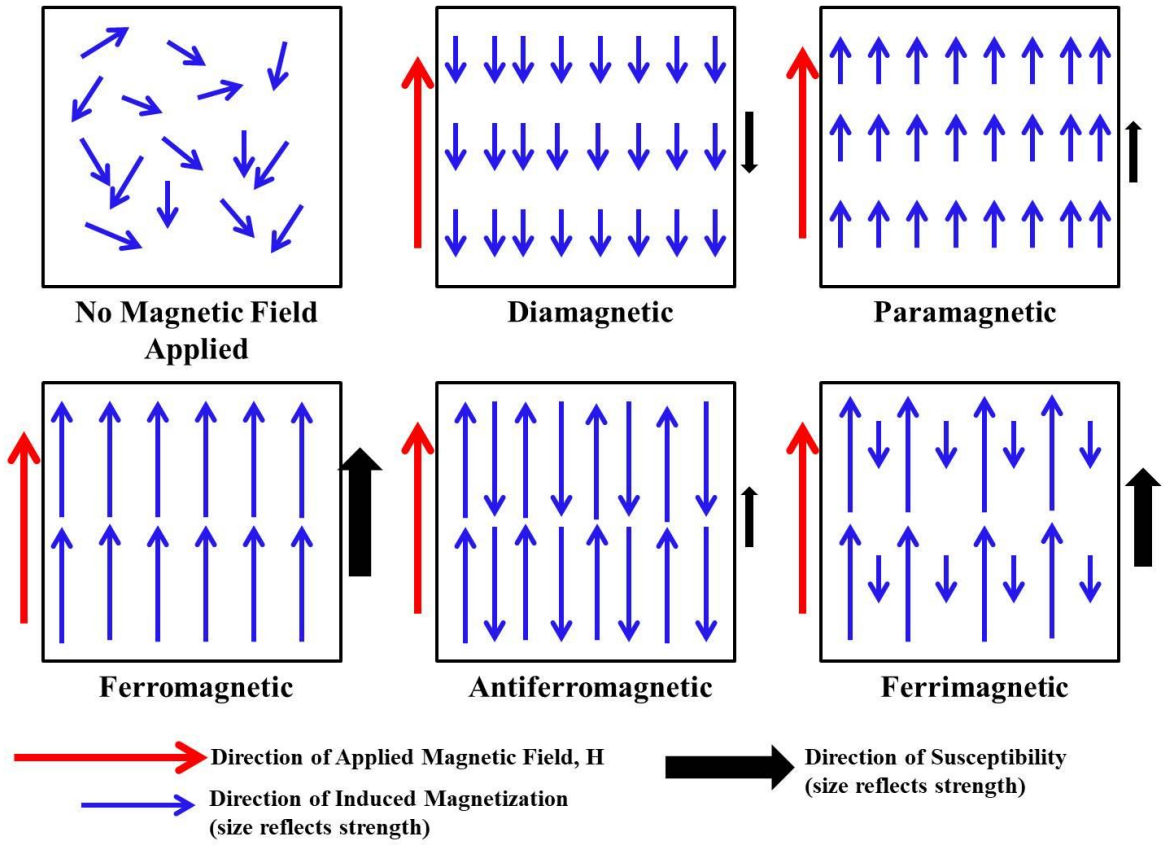

Figure 2.1: Schematic representation of different magnetisms with spin orientations under applied magnetic field.

Ferrimagnetism is similar to antiferromagnetism except that the magnetization of the two sublattices has different magnitudes, resulting non-zero net magnetization. This type of magnetism happens in materials such as ferrites, oxides of various metal elements, etc. The most common ferrimagnet is $FeO.Fe_2O_3$ or Fe_3O_4.

2.1.4 Magnetic Anisotropy

Magnetic anisotropy describes how the magnetic properties depend on the direction of applied field with respect to the crystal lattice. Depending on the orientation of the field, saturation magnetization can be achieved in two different directions (easy and hard axes) by applying lower and higher magnetic field, respectively. Easy axis is the direction, along which lower magnetic field is sufficient to achieve saturation magnetization and hard axis is the direction, along which higher magnetic field is required to reach saturation magnetization. The physical origin of the magnetic anisotropy is the magnetic dipolar interaction and the spin-orbit interaction. A common application of this phenomenon is compass in which needle is magnetized along the needle's direction instead of perpendicular direction. There are many types of magnetic anisotropy such as magneto-crystalline anisotropy, shape anisotropy, magneto-elastic anisotropy, exchange anisotropy, etc [9].

Magneto-crystalline anisotropy is the energy required to deflect the magnetic moment in a single crystal from easy to hard axis direction. This anisotropy originates from spin-orbital interaction. Hexagonal cobalt is one of the examples of this anisotropy where uniaxial anisotropy is parallel to the crystalline axis.

Shape anisotropy is mediated by the dipolar interaction. Its contribution is dependent upon the shape of the sample as this interaction is long range. Therefore, it is important in thin films.

Magneto-elastic anisotropy arises from the spin-orbit interaction of each electron. The spin moments are coupled to the lattice via the orbital electrons. If the lattice is changed by strain, the distance between the magnetic atoms is also varied resulting change in interaction energies. This produces magneto-elastic anisotropy.

Exchange anisotropy arises from magnetic exchange interaction between a ferromagnet and an antiferromagnet or ferrimagnet. Magnetic coupling at the interface of the two materials can create a preferential direction in the ferromagnetic phase, which takes the form of uni-directional anisotropy [10].

Among these anisotropies, crystalline anisotropy is one of the most discussed anisotropies. This is specific to a given material and independent of particle shape. For uniaxial crystal symmetry, the magneto-crystalline anisotropy energy is given by [11]

$$E = K_1 V \, Sin^2 \theta + K_2 V Sin^4 \theta + \ldots\ldots \qquad \text{.....(2.7)}$$

Where V is the volume of particle, K_1 and K_2 are the anisotropy constants and θ is the angle between the magnetic moment and the symmetry or easy axis (**Figure 2.2 (a)**) of crystal. The values of K's have strong dependence on temperature. They decreases rapidly as temperature approaches the Curie temperature and become constant at much lower temperature than the Curie temperature of the material. K_2 and other higher order anisotropy constants are negligible with respect to K_1 [9]. For single domain particles with uniaxial symmetry, the anisotropy energy can be represented as

$$E(\theta) = K_{eff} V Sin^2\theta \quad \text{.....(2.8)}$$

where $K_1 = K_{eff}$ is uniaxial anisotropy constant. Eq. 2.8 describes two local energy minima at each pole (θ = 0 and π) separated by an equatorial (θ = π/2) energy barrier $K_{eff}V$ shown in **Figure 2.2 (b)**.

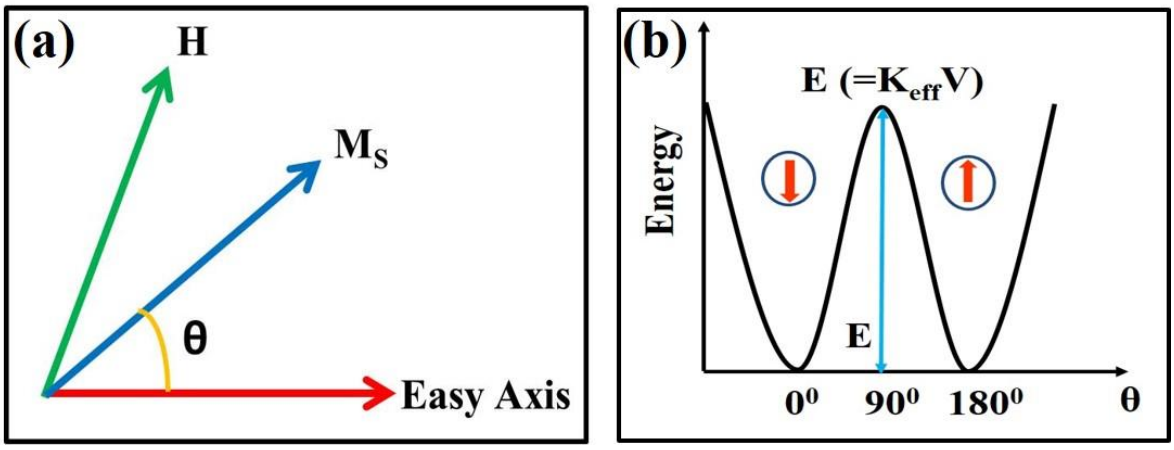

Figure 2.2: (a) Schematic drawing of magnetization, applied magnetic field and easy axis for a material and (b) Change in anisotropy energy barrier E in the absence of an applied external magnetic field.

2.1.5 Magnetic Domains and Domain Walls

Experimentally, it is observed that a ferromagnetic material does not show net magnetization in the absence of external magnetic field. This is explained by the scientist Weiss introducing the concept of ferromagnetic domain. The domains are formed to minimize the total magnetic energy of the material. The total magnetic energy of the material comprises of the exchange energy along with the magnetic field, anisotropy, domain wall and magnetostrictive energies. This energy can be lowered by reducing the volume of the domain by subdividing it into neighbouring subdomains. In the absence of external magnetic field, the magnetization vector of different domains orient randomly resulting no net magnetization in the specimen. The domain walls, formed at boundaries, increase the exchange energy as well as total magnetic energy of the material due to the presence of non-parallel spins in the domain wall. Therefore, subdivisions of domains cannot continue indefinitely. A FM material must possess a domain structure consisting of a number of smaller domains which corresponds to a state of minimum energy. Besides, in the presence of an external magnetic field, magnetization of FM materials may be imposed on (i) the growth in size of the domains oriented along field direction at the expense of other domains (off field directions), and (ii) the rotation of magnetization direction of the domains along the field direction. These two magnetization processes are illustrated below in **Figure 2.3**.

When a small magnetic field is applied on FM material, the domains pointing along the direction of the field grow at the expense of that having opposite orientation. Therefore, a small magnetization appears into the specimen. Such displacement of domain boundaries is mostly reversible. As the field is increased further, a larger number of domains grow favourably, resulting increase in magnetization. The displacement of the domain boundaries thereafter becomes irreversible. The growth of the domains continues until the favourable domains, could develop to the maximum extent with their easy directions of magnetization. All domains rotate from their easy direction to field direction with increasing magnetic field and magnetization slowly attaining saturation value M_S.

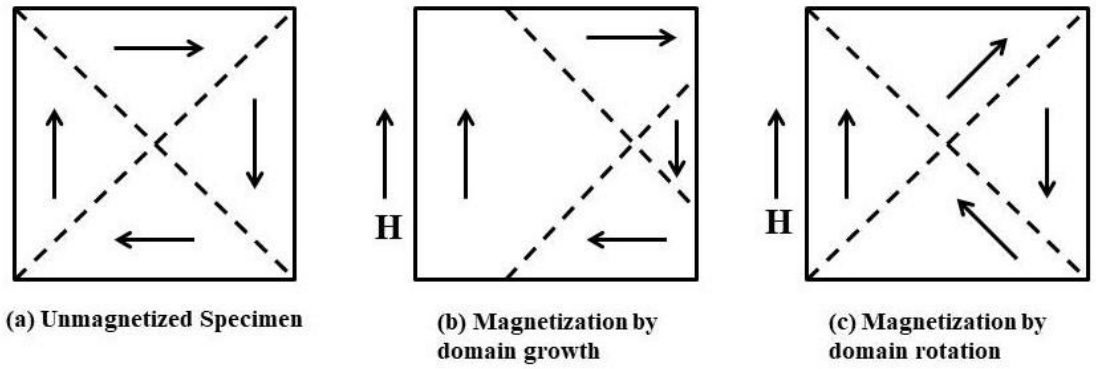

Figure 2.3: Different magnetization processes

On decreasing the field, the magnetization does not follow the same path and random state of orientation of domains cannot be reached easily. Therefore, there exists a non-zero magnetization even at zero magnetic field. This magnetization is known as remanence (M_r). This magnetization is reduced to zero by applying

a reverse magnetic field, named as coercive field (H_C). A similar variation in the reverse magnetization is also observed as the reverse field is first increased and then decreased. This results a closed loop known as Hysteresis loop as shown in **Figure 2.4**. This hysteresis curve is highly important in order to understand the quality of a magnetic material and selection for a particular application.

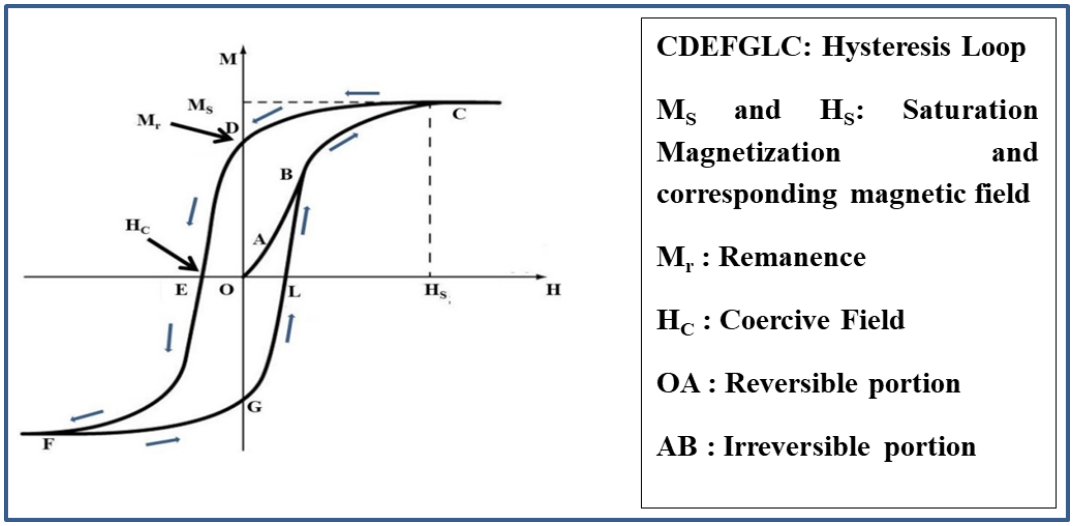

Figure 2.4: Typical hysteresis curve for a ferromagnetic material

2.1.6 Magnetic Frustration

Magnetic frustration arises either from the geometry of the lattice or from the competition between different kinds of magnetic interactions. It results some ordered (e.g non-collinear, chiral) or disordered (e.g spin liquid, spin ice, etc.) magnetic states. The term 'geometrical frustration', or in short 'frustration', in the context of magnetic systems, has been introduced by Gerard Toulouse in 1977 [12], whereas frustrated magnetic systems was studied even before. Geometrical

frustration, which stems from the relative arrangement of spins, is an important feature in magnetism.

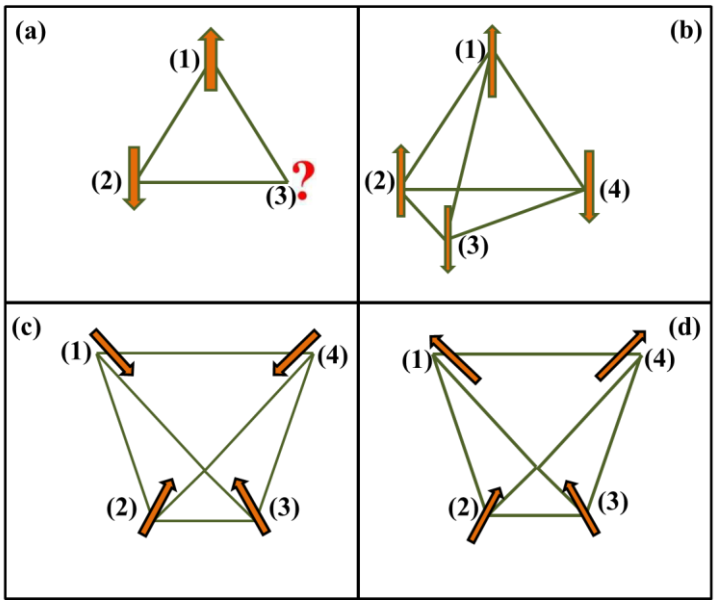

Figure 2.5: Geometrical frustration. (a) Anti-ferromagnetically interacting spins in a triangular arrangement, (b) Anti-ferromagnetically interacting spins in a tetrahedral arrangement, (c) Spins along the easy axes of a tetrahedron, (d) Frustrated easy spins in a tetrahedron

A simple 2D example is shown in **Figure 2.5(a)** where three magnetic ions are situated at the corners of a triangle with antiferromagnetic interactions between them. When two of them are aligned antiferromagnetically, the third one can no longer minimize its interactions with both the spins simultaneously i.e third one is frustrated. Thus, antiferromagnetic interactions are incompatible with triangular lattice symmetry, known as geometrical frustration. Similarly in 3D, four spins arranged in a tetrahedron (**Figure 2.5(b)**) may experience geometrical frustration. **Figure 2.5(b)** shows interactions between 1 and 3, 1 and 4, 2 and 3, 2

and 4 are favourable where interactions between 1 and 2, 3 and 4 are unfavourable. Thus, it is impossible to get all interactions favourable and the system gets frustrated. It is also possible in non-collinear arrangement of spins. **Figure 2.5(c)** and **Figure 2.5(d)** represent spins along the easy axis of a tetrahedron, which means the absence of geometrical frustration and frustrated easy spins in a tetrahedron, respectively.

2.1.7 Spin Glass

Spin glasses [13] are the magnetic systems in which interactions between the magnetic moments are in conflict because of some frozen-in structural disorder. Unlike ferromagnetic systems, spins are oriented in random direction in three dimensional space, as shown in **Figure 2.6**. The term 'glass' arises from an analogy between the magnetic disorder in a spin glass and the positional disorder of a conventional chemical glass. Spin glasses are categorized as 'metastable' state because of their stable complex internal configuration, different from the lowest energy configuration (ferromagnetic alignment).

The time dependence of magnetic behaviour of spin glass system distinguishes it from other magnetic systems. The spin glass system exhibits typical magnetic behaviour (such as paramagnetism) above spin glass transition temperature, T_g. If a magnetic field is applied to the sample during cooling from temperature $T > T_g$, the magnetization of the sample increases with decreasing temperature following the Curie law.

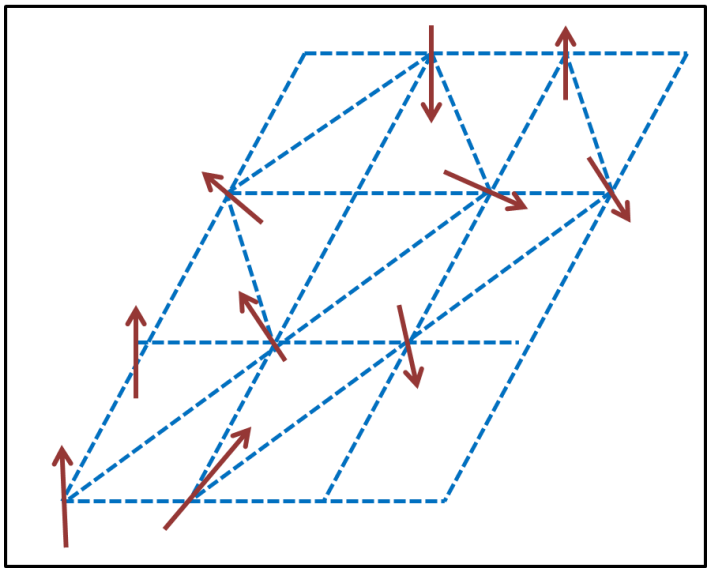

Figure 2.6: Schematic representation of random spin structures of spin glass systems

At T_g, the sample becomes spin glass and further cooling of it leads a very small or no change in magnetization. This is known as field-cooling magnetization. When the applied field is removed, the magnetization of the spin glass decreases rapidly with time to a lower value of magnetization, named remanent magnetization. Beyond this value, decay in magnetization with time becomes very slow process. In addition, this shows non-exponential curve of magnetization versus time and no simple function can fit the curve adequately [14]. This slow decay is the signature of spin glass systems. This phenomenon differ spin glass from ferromagnetic samples which shows time independent magnetization. Besides, paramagnetic samples show rapid and exponential decrease in magnetization to zero with no remanent magnetization after removal of external magnetic field. Thus, paramagnetic material differs from spin glass materials. If the sample is cooled below T_g in the absence of an external magnetic

field, named zero-field cooling, and then a magnetic field is applied to the spin glass phase, a rapid initial increase to a magnetization value, known as zero field cooled magnetization, is observed. This is followed by a slow upward drift toward the field cooled magnetization.

2.1.8 Superparamagnetism

Superparamagnetism is a form of magnetism which arises in small ferromagnetic or ferrimagnetic nanoparticles. Generally, nanoparticles with size less than an hundred nanometer can be considered as single domain particles. The magnetization of the nanoparticles, known as single giant magnetic moment, is also considered as the sum of all individual magnetic moments of atoms contained by the nanoparticles. This approximation is known as "macro-spin approximation". For single domain particle having volume V with uniaxial anisotropy, the maximum anisotropy energy barrier separating magnetization directions is given by $E=K_{eff}$ V, according to Eq.2.8. This anisotropy energy of single domain particle decreases with decreasing particle size and becomes comparable to or less than the thermal energy k_BT (k_B= Boltzmann Constant, T= temperature) for grain size lower than the critical value. Then the spin magnetization can flip its direction randomly over short period of time due to thermal fluctuation. The mean time between two successive flips is called the Neel relaxation time (τ_N) and is given by Neel-Arhenius equation [15].

$$\tau_N = \tau_0 exp\left(\frac{K_{eff}V}{K_BT}\right) \text{.....(2.9)}$$

where τ_0 is characteristic length of time (10^{-9} to 10^{-12} s) related to the material. In absence of any external magnetic field, the value of average magnetization of the nanoparticles will be zero. Whereas in presence of an external magnetic field, ensemble of single domain particles will behave in the same way as an ensemble of paramagnetic atoms with much greater susceptibility. There will be saturation when all the spins align in the direction of the external magnetic field but no hysteresis in S-shaped M-H loop can be seen. Thus, all the theoretical treatments of paramagnetism fit also for superparamagnetism though there is a huge difference in spin number (S_{spin}) between both the systems. The value of S_{spin} is ~10^5 for superparamagnetic system, whereas S_{spin} has value 1 for paramagnets. A schematic representation of the M-H loop behaviour of single domain particle with temperature is shown in **Figure 2.7(a)**.

The magnetic behaviour of superparamagnetic particles depends also on the observation time or measurement time (τ_m). When the relaxation appears so fast with respect to the measurement time ($\tau_m >> \tau_N$), no time average of the magnetization orientation is observed which is analogous to Langevin paramagnet. On the contrary, the assembly of superparamagnetic particles behave as an ordered magnetic state (ferro, ferri or antiferro) when the relaxation appears very slow (blocked state) with respect to measurement time ($\tau_m << \tau_N$).

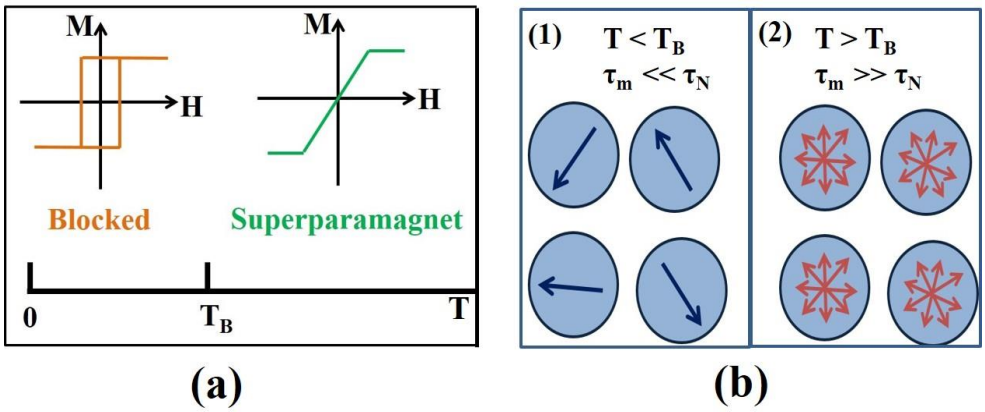

Figure 2.7: (a) Schematic representation of the M-H loop behaviour of single domain particle with temperature, (b) Case 1 illustrates the blocked state at $T<T_B$ where the magnetic moment of each particle is well-defined. Case 2 shows the superparamagnetic state at $T>T_B$ where the magnetization direction constantly flips, resulting net zero moment.

These two states are represented in **Figure 2.7(b)**. Transition from superparamagnetic to blocked state would occur by lowering the temperature. The temperature at which τ_m equals to τ_N, is defined as blocking temperature (T_B), separating these two states. For a particular superparamagnetic sample, T_B with respect to particular measuring technique increases with increasing particle size. It should be mentioned that T_B also depends on the measurement time (τ_m) and increases with decreasing τ_m.

2.1.9 Magnetic Memory Effect

Magnetic memory effect (MME), phenomenon of remembering the previous history and unfolding it under suitable conditions by the sample, have been investigated intensively till today due to their significance in technological applications as well as for fundamental physics [16]. This arises due to the appearance of interparticle long-range magnetic ordering at low temperatures.

The interactions of the nanoparticles must be very sufficiently strong to make these magnetic phenomena possible. This phenomena have been widely studied in various nanomaterials such as superparamagnetic (SPM), the spin-glass (SG), the superspin glass (SSG) system, etc. The non-interacting SPM system exhibits field cooled (FC) MME due to the distribution in their relaxation times, which arises through particle size distribution. Whereas the SG system shows both FC and zero field cooled (ZFC) MME because of the surface effects, interparticle interactions, and the random distribution of the anisotropic axis. Therefore, MME has been utilized as a fingerprint test in distinguishing SPM and SG systems [17,18]. It should be mentioned that the SPM to SSG phase transition can be observed if the material possesses particles having large size distribution and randomness. The possible evidences of such SPM to SSG phase transition are: (i) the critical slowing down of the relaxation time τ on approaching the transition temperature T_g [19, 20]; (ii) the divergence of the nonlinear susceptibility χ_{nl} at T_g [21]; (iii) the magnetic aging in the ordered phase [19, 22].

2.2 Exchange Bias Phenomena

2.2.1 Discovery and Applications

Exchange Bias (EB) effect is a physical phenomenon which is first observed by Meiklejohn and Bean in the FM Co/AFM CoO core-shell system in 1956 [6]. They found a shift of the magnetic hysteresis loop along the field axis at low

temperature when specimen was cooled in the presence of static magnetic field [7]. This effect was first named as "new magnetic anisotropy" and later described as exchange anisotropy. Initially, the EB effect was observed in a system consisting of FM and AFM substances with the Curie temperature (T_C) of FM component is greater than Neel temperature (T_N) of AFM component. When the sample is exposed to a static magnetic field at a temperature ($> T_N$) and cooled through T_N down to a temperature much less than T_N, the FM spins adjacent to AFM spins are coupled to the uncompensated AFM spins [23]. This coupling results a displacement of the magnetic hysteresis loop that is the typical manifestation of EB effect [10].

Since its discovery, EB effect has been investigated in different systems having FM/AFM interfaces such as inhomogeneous material [7], small particles [6, 10], thin film [24-26], FM thin films on AFM single crystals [27-28], etc. It is found not only in FM/AFM interfaces but also in other types of interfaces such as Ferrimagnetic/AFM [29], FM/Ferrimagnetic [30], Diluted magnetic semiconductors/AFM [31], etc. A numerous application of EB effect in electronics devices makes it an integral part of modern magnetism. One of the most popular applications of EB is in spin valve device that is the main component of read head of computer hard disks [32-33], magneto-resistive sensors [34-35], magnetic random access memory [36], etc.

2.2.2 Basic Phenomenology

Experimentally, it is observed that the shifting of hysteresis loop, resulting from the pinning mechanism at the interface between soft and hard magnetic substances, is the manifestation of EB effect. The horizontal and vertical shifting of hysteresis loop are shown in **Figure 2.8(a)** and **Figure 2.8(b)**, respectively. A schematic representation of EB effect due to the field cooling in bilayer FM/AFM structure and appearance of pinned FM layer at the interface are shown in **Figure 2.8(c)** and **Figure 2.8(d)**, respectively. A FM/AFM bilayer system with $T_C > T_N$ is considered for the qualitative explanation of basic phenomenology of EB effect. The shift of hysteresis loop of this system can be explained by the basic phenomenology of EB effect as shown in **Figure 2.9**. Here, it is assumed that both FM and AFM components are in single domain state during the magnetization process as well as magnetization reversal process. When system is cooled at temperature T, where $T_N<T<T_C$, the AFM component shows paramagnetic behaviour while spins of FM component align themselves along applied magnetic field, H. It results net magnetization, M, shown in **Figure 2.9(1)**.

The hysteresis curve of FM component is centered at origin, unbiased by the AFM component. A phase transition from paramagnetic to antiferromagnetic one occurs in the AFM component when system is cooled down below T_N, in the presence of saturated magnetic field of FM component. Exchange interaction at the interface between FM and AFM influences the first mono layer of AFM

component to align parallel or antiparallel to the FM spins. The next monolayer of AFM aligns antiparallel to first monolayer spins to maintain AFM order and so on, as shown in **Figure 2.9(2)**. The uncompensated spins at the AFM interface leads a net magnetization of this AFM monolayer.

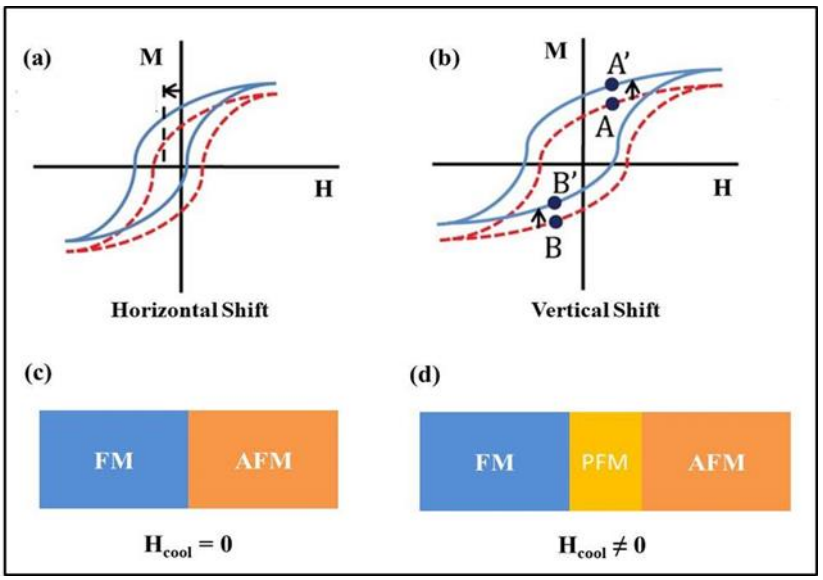

Figure 2.8: (a) and (b) horizontal and vertical shifting of hysteresis loop, respectively. (c) and (d) schematic representation of EB effect due to field cooling in bilayer FM/AFM structure and bilayer structure with pinned FM layer at the interface, respectively.

When magnetic field is reversed, the FM spins try to rotate in plane to align themselves along direction of reverse applied field while they are opposed by exchange coupling with AFM spins, as shown in **Figure 2.9(3)**. Therefore, a stronger external force is required to overcome the interfacial exchange coupling in order to reverse the orientation of FM spins. This results higher value of coercive field than that of at $T_N < T < T_C$. The FM spins need a smaller external field in order to rotate back from negative saturation field (**Figure 2.9(4)**) to their

initial positions (**Figure 2.9(5)**). The FM spins experience a torque in all the directions except in the field cooling direction. As a result, the hysteresis loop is centered at particular negative values except zero value of the applied magnetic field. This shifting of the centre of the hysteresis loop is the manifestation of exchange bias field (H_{EB}). The value of H_{EB} is negative with respect to the direction of FM spins after field cooling. Here, AFM spins are considered to be fixed to the field cooling direction during the reversal process. With the shifting of centre of hysteresis loop, an enhancement of coercive field of FM/AFM bilayer is also observed but could not be explained by this simple phenomenological model.

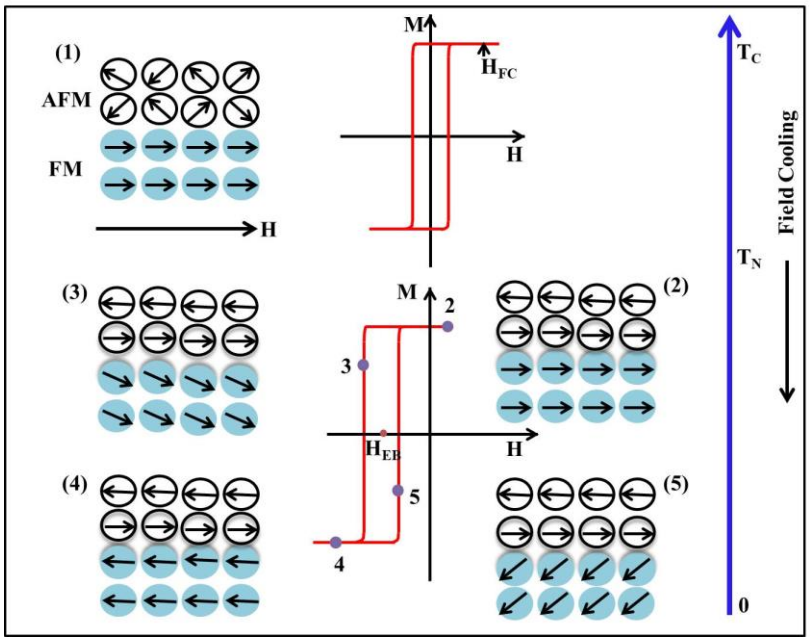

Figure 2.9: Basic Phenomenological model describing the shift of hysteresis loop of an FM/AFM bilayer. Panel (1): The initial state of spin configuration at $T_N<T<T_C$. Panel (2): The spin configuration at $T<T_N$. Panels (3) and (5): Spin configuration during reversal process. Panel (4): Saturated state of spins at negative fields.

2.2.3 Training Efeect

Training effect is one of the important properties of EB phenomena. It is defined as the difference between subsequent magnetization reversal loops. This is investigated by consecutive field cycling at low temperature after the field cooling. It was observed in thin films and nanoparticles although it was described first for thin films [37]. In thin film systems, it has been experimentally shown that the reduction of H_{EB} is expressed as

$$\boldsymbol{H_{EB} - H_{EB}^{\infty} \propto n^{-1/2}} \text{.....(2.10)}$$

Where n is the loop index number and H_{EB}^{∞} is the exchange bias for n = ∞. There are two kinds of EB effect reported; one is the decrease of EB effect between the first and second loop (for n < 2) [38] and another one is the decrease of EB effect involving subsequent higher number of loops (for n ≥ 2) [39]. The above equation (2.10) can be performed in series expansion approach which satisfies the second type of training effect. Binek recently proposed the more generalized interpretation of the training effect using a discretized Landau-Khalatnikov equation [40] where the continuous time parameter was replaced by n. The general recursive formula for H_{EB} is represented as

$$\boldsymbol{H_{EB}(n+1) - H_{EB}(n) = -\gamma[H_{EB}(n) - H_{EB}(n=\infty)]^3} \text{.....(2.11)}$$

where γ is a constant. Equation (2.10) is limiting case of equation (2.11) and equation (2.10) can be derived from series expansion of equation (2.11). Equation (2.11) satisfies the training effect for all n. The first and second types of training

effect have been proposed to arise from the AFM magnetic symmetry [38] and from the configuration of the AFM domains during field cycling [41], respectively. However, other factors, apart from microstructure, play a role in the training effect, promoting the effect in some AFM single crystal in low AFM anisotropy based systems [42].

2.2.4 Blocking Temperature

The existence of EB effect is closely related to the magnetic order of the AFM component [39]. This magnetic ordering can be degraded by increasing the temperature, mainly at $T \geq T_N$. Hence, as the temperature increases and reaches to the Neel temperature T_N of the AFM, the EB effect disappears. On the contrary, it is also often found that the EB effect disappears at temperatures far below T_N, especially in nanomaterial systems. The temperature, at which the EB field vanishes, is usually denoted as blocking temperature (T_B). This particular value of temperature depends on size of particle as well as thickness of AFM layers. High quality thin film systems having thick AFM layers often show $T_B \approx T_N$, while other system with thin or polycrystalline AFM layers have $T_B < T_N$ [43]. In the case of nanomaterial systems, thermal dependence of H_{EB} is influenced by volume distribution, randomness of the anisotropy axes and the existence inter-particle interactions along with structural factors.

2.2.5 Compensated and Uncompensated Interfaces

An uncompensated as well as a compensated FM/AFM interface plays an important role in the existence of EB effect as discussed in different theoretical models.

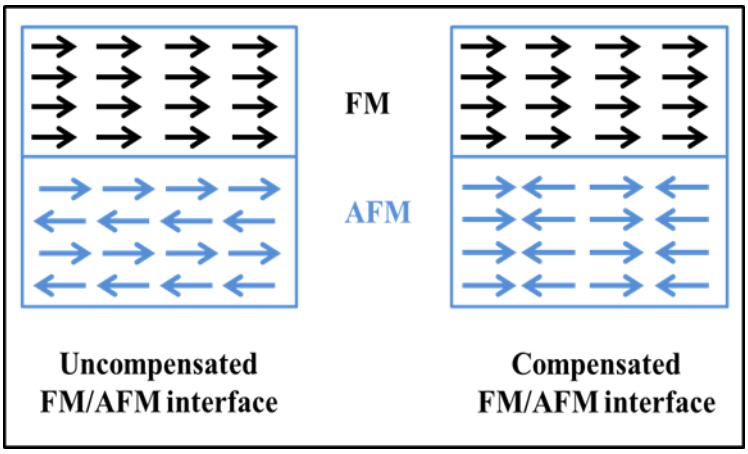

Figure 2.10: Schematic diagram of uncompensated and compensated FM/AFM interfaces

An uncompensated FM/AFM interface can be understood in the way that the first mono-layer of AFM aligns with the FM in parallel and the subsequent mono-layers of the AFM in antiparallel order with each other. Whereas, in case of a compensated interface, the spins align antiparallel within each of the AFM mono-layer and thereby, no coupling can occur at the interface. The compensated and uncompensated interfaces are displayed in **Figure 2.10**. It is to be noted that the formation of any one of the interfaces depends on the specific AFM and the crystalline directions.

2.2.6 Theoretical Model

A large number of theoretical models [39, 44-49] have been developed to understand the EB effect quantitatively. However, none of these models can able to describe the EB phenomena completely.

Meiklejohn and Bean model, first model to explain EB effect, was proposed by Meiklejohn and Bean [6-7, 10]. This model describes the FM/AFM coupling and predicts shift in hysteresis loop which is the manifestation of EB effect, as explained in section 2.2.2 and represented in **Figure 2.9**. In this model, FM and AFM components are assumed in a single domain state. FM can rotate rigidly whereas the AFM, having uniaxial anisotropy, remains unchanged during the rotation of FM spins in the presence of reverse applied magnetic field. The FM/AFM interface is considered as smooth and AFM monolayer spins at interface are uncompensated. This model is based on the Stoner-Wohlfarth model [50-51], which calculates the magnetization due to external magnetic field by minimizing the total magnetic energy. Meiklejohn and Bean had introduced an energy term for the coupling between FM and AFM component. The total magnetic energy per unit interface area is given by

$$E = -HM_{FM}\, t_{FM}\, cos(\theta - \beta) + K_{FM} t_{FM} sin^2(\beta) + K_{AFM} t_{AFM} sin^2(\alpha) - J_{EX} cos(\beta - \alpha) \quad \text{.....(2.12)}$$

Where H is the external magnetic field, M_{FM} is the magnetization of the FM, t_{FM} and t_{AFM} are the thickness of FM and AFM, respectively, K_{FM} and K_{AFM} are the

anisotropy constant of FM and AFM, respectively. J_{EX} is the exchange interaction constant between FM and AFM. The angle α is formed between the magnetization of AFM (M_{AFM}) and K_{AFM}, β is formed between M_{FM} and K_{FM} and θ is formed between H and K_{FM}, shown in **Figure 2.11**. In the above equation, the first, second, third and fourth terms represent Zeeman energy due to interaction between H and M_{FM}, anisotropy energy in FM, anisotropy energy in AFM and exchange interaction energy between FM and AFM, respectively. K_{FM} and K_{AFM} are assumed to be oriented parallel to the field cooling direction (θ=0). Neglecting the FM anisotropy and minimizing w.r.t α and β, the shift of hysteresis loop i.e. exchange bias field (H_{EB}) obtained by Meiklejohn is given by

$$H_{EB} = -\frac{J_{EX}}{M_{FM}t_{FM}} \quad \text{.....(2.13)}$$

It gives the expected characteristics of the hysteresis loop for an ideal case. With respect to cooling field direction, EB shows negative sign. Although this model gives a good understanding of EB, this neglects many parameters that can play an important role in EB such as interface roughness, AFM or FM domains, etc. Due to these assumptions, EB field, predicted by this model, is often larger than experimental value for most of the thin film system [44, 49, 52] and H_{EB} does not show negative value always [53-55]. Moreover, AFM spins are rigid during FM spin reversal only for $K_{AFM}t_{AFM}/J_{EX} \geq 1$, otherwise AFM spins follow the FM magnetization reversal which results zero exchange bias and an increase in coercivity. Also, training effect cannot be explained by this model.

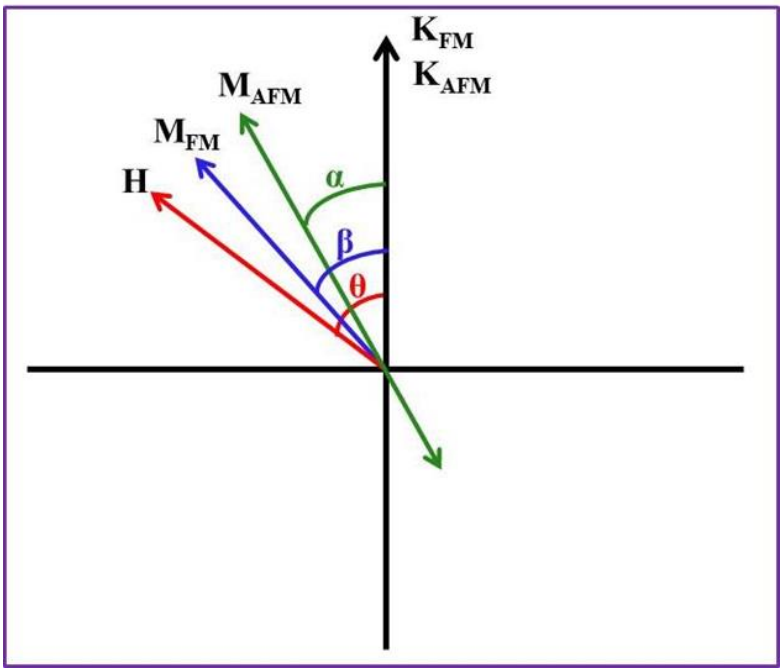

Figure 2.11: Schematic view of angles and vectors used in the Meiklejohn and Bean model.

Néel/Mauri domain wall model was the next attempt to reduce the difference in theoretical value with experimental value of H_{EB}. Néel introduced the concept of a planar domain wall formation during the magnetization reversal rather than a coherent rotation in Meiklejohn and Bean model. The H_{EB} is reduced due to fraction of the exchange coupling energy stored by AF domain wall. Néel's study mostly was based on the fact that the thickness of the layers should be at least about hundreds of nanometers. That is why it could not explain the phenomena in thin films. Later, Mauri [56] introduced the domain wall formation in the AFM parallel to the FM/AFM interface due to the magnetization reversal of the FM layer. The Néel/Mauri concept predicts more feasible value of EB for thick enough AFM layer. The main drawbacks of this model are (1) the formation of AFM domain wall is associated with strong coupling and weak AFM anisotropy;

(2) the interface is considered as ideal; (3) this model does not explain enhancement of coercive field (H_C).

Random Field model was introduced by Malozemoff assuming roughness of the interface and a compensated AFM [57]. Because of roughness on the atomic scale, uncompensated spins remains at the interface and a random exchange interaction between FM and AFM happens. This random field results the breaking of AFM into domains with a domain wall perpendicular to the interface. Therefore, the interface interaction is decreased and exchange bias field is calculated as

$$H_{EB} \propto \frac{2\sqrt{J_{EX}K_{AFM}}}{M_{FM}t_{FM}} \text{ ……..(2.14)}$$

which shows much better result with experimental data than the previous models. This model also can explain the training effect observed in EB system. It leads the breakup of the single domain state of AFM during training mechanism.

The **Koon model** proposes a perpendicular coupling between the FM and a compensated AFM layer as mechanism for origin of EB [58]. It can give the explanation for the effect of positive EB.

In the **Domain State model,** the AFM in an EB system is taken to be diluted with non-magnetic defects [59-60]. The AFM magnetization originates from uncompensated spins and controls the EB interaction with the FM. Training effect can be explained by this model. It is also able to explain the EB dependence on temperature, blocking temperature, cooling field and the AFM thickness.

Besides these models, a lot of other models, which are more system specific, have been proposed to explain the origin of EB.

2.3 Dielectricity

2.3.1 Discovery and Technological Importance of Dielectrics

Electrically insulating materials are playing an important role since the beginning of the science and technology of electrical phenomena. Dielectrics are basically electrical insulators, which can prevent the flow of current in an electrical circuit. The capacitance of a condenser can be modified by inserting dielectric materials in the space between conductors. But there have been no reports of the investigation on the properties of insulating or dielectric materials till 1837 in spite of the fact that the first capacitor was developed by Cunaeus and Mussachenbroek way back in 1745 [61]. Faraday first observed that the capacity of a condenser could be increased if the space between conductors was filled with insulator or dielectric material. This work encouraged further investigation on dielectrics or insulating medium aiming at maximizing the amount of charge that can be stored by a capacitor [62]. Apart from the insulation aspect, the dielectric phenomenon could well become more general and fundamental as it is the origin of dielectric polarization. A systematic investigation on dielectric properties of materials was done by Clausius [63] and Mossotti [64]. They followed Faraday's work by considering that dielectrics were composed of conducting spheres in a

non-conducting medium. They established the correlation between macroscopic characteristics of insulator, the specific inductive capacity, also known as dielectric constant with the microscopic structure of the material. Debye [65] extended the Clausius-Mossotti theory by taking into account the permanent dipole moments associated with the molecules. This molecular dipole moment is responsible for the macroscopic dielectric properties of the materials and that can be calculated from the measurement of dielectric constant. Debye theory showed an excellent agreement with the experimental results for most of the polar liquids [66]. It was later prolonged by Onsager, Krikwood and Frohlich [67-69]. Moreover, Debye applied the concept of permanent molecular dipole moment for explaining the anomalous dispersion of the dielectric constant observed by Drude [70]. An alternating electric field with appropriate frequency leads to dielectric dispersion. The orientation of the dipoles result frequency dependant dielectric constant and dielectric loss over a broad band of frequencies. At very high frequency of alternating field, the orientations of dipoles cannot follow the field frequency and no longer able to contribute in dielectric constant. Debye showed that in a certain frequency band, a phase lag is developed between the field and dipole orientation, and as a result the energy drawn from electrical source by the material is dissipated as heat. Unlike polar liquids, the dielectric behaviour for solids was found to be deviating significantly from Debye's theory [71]. Two major approaches were proposed to modify the Debye theory and explain the non-

Debye relaxation behaviour of the materials. The first approach was proposed by Cole [72], Davidson [73] and William [74] in terms of the superposition of an exponentially relaxing process. The second approach was proposed by Joncher [75] in terms of cooperative molecular motions.

Modern day electronics such as mobile communication, i-pads, laptops, wireless communication systems are developing rapidly. Microwave resonators and decoupling capacitors are the integrated parts of these systems, which demands high quality dielectric materials with properties like low loss tangent, large dielectric constant, small leakage current, small temperature coefficient of resonator frequency (for resonators), etc. Thus, the understanding of how dielectric behaviour of dielectric materials varies with field, frequency and temperature becomes very important for modern technological applications.

2.3.2 Theoretical Details

2.3.2.1 Polarization and Polarizability

One of the important properties of dielectric is its ability to get polarized in the presence of an external electric field. When an external electric field (E_0) is applied, the positive charges of atoms and molecules of dielectrics are pushed in the field direction while negative charges in the opposite direction from their equilibrium position. Hence, a large numbers of electric dipoles, each having some dipole moment in the field direction, are formed. This process is known as polarization (P) as shown in **Figure 2.12**. It is defined as the electric dipole moment

per unit volume of the material. A field corresponding to the electric dipoles, named polarization field (E_P), is produced in opposite direction of external field. Hence, external field (E_0) is reduced to E as an effect of polarization ($E < E_0$). The macroscopic field (E) can be written as

$$\boldsymbol{E = E_0 + E_P} \text{.....(2.15)}$$

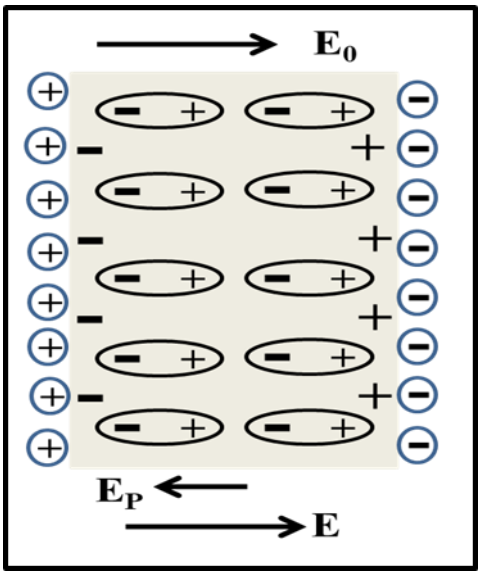

Figure 2.12: Schematic diagram of Polarization

For static electric field, polarization (P) is proportional to this macroscopic field and can also be expressed as

$$\boldsymbol{P = \varepsilon_0 \chi_e E} \text{.....(2.16)}$$

where ε_0 is the free space permittivity and χ_e is the electric susceptibility that is the measure of the polarization per unit resultant electric field in the material. The electric field acting at the site of an atom or molecule is significantly different from the macroscopic electric field E and is called the local field (E_{loc}). This field

is responsible for the polarization of each atom or molecule of a solid. For an molecular site with cubic symmetry, the local field is given by

$$\boldsymbol{E_{loc} = E + \frac{P}{3\varepsilon_0}} \quad \textbf{.....(2.17)}$$

where 1st term is macroscopic field and 2nd term represents the field due to polarization of other atoms in the solid. Eq. 2.17 is known as Lorentz relation which can be modified with shape of the specimen [76].

There are mainly four types of polarization found in dielectric materials in the presence of an external electric field [77], as shown in **Figure 2.13**.

Electronic Polarization: Redistribution of electronic charges relative to the nucleus generates dipoles which gives rise to electronic polarization (P_E) by aligning themselves along the applied electric field.

Atomic Polarization: This occurs in solids with ionic bonding which acts as dipole with dipole moment. But the net dipole moment as well as polarization is zero in the absence of applied electric field due to the symmetry of crystal. In presence of electric field, ions are displaced from their equilibrium position and align along the field direction. It results atomic or ionic polarization (P_A).

Dipolar Polarization: This type of polarization happens only in polar molecules with permanent dipole moments. In the absence of external electric field, random orientation of molecules results no net dipole moment. The dipolar polarization occurs in presence of external field. The molecules with permanent dipole

moment align themselves along the field direction and results net polarization. This polarization is also known as orientational polarization (P_D).

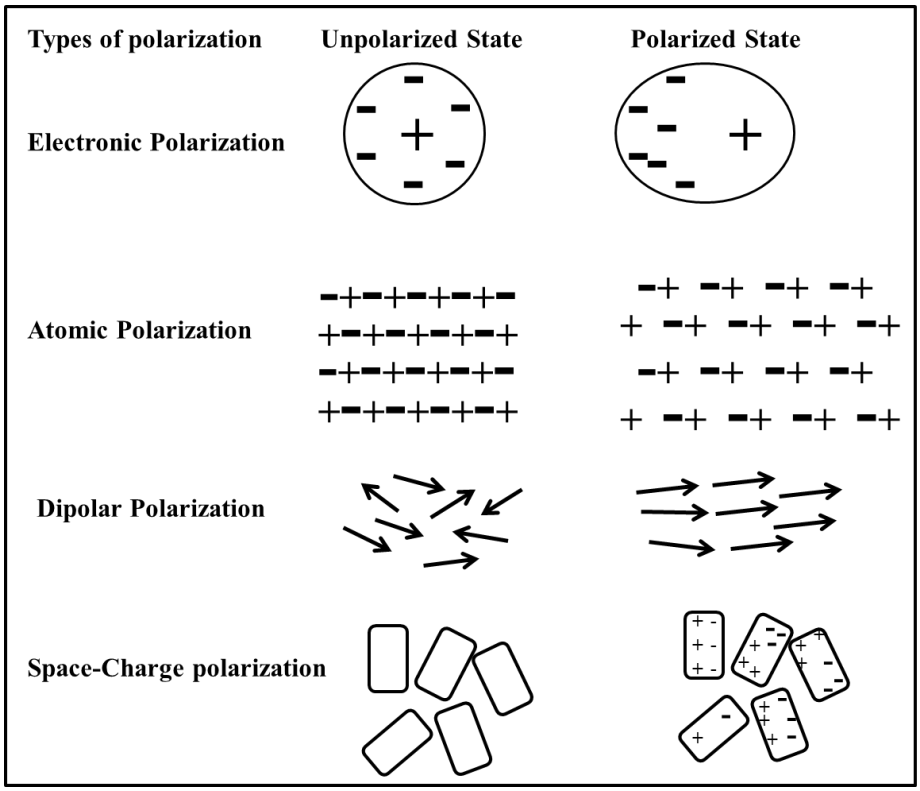

Figure 2.13: Representation of Four types of Polarization

Space-Charge Polarization: It arises from the accumulation of charge dipoles at grain boundaries as well as the interface of electrode materials. The space charge polarization (P_{INT}) can be viewed as the combination of hopping polarization and interfacial polarization. In dielectric materials, localized charges such as ions and vacancies or electrons and holes can hop from one site to another site, gives rise to hopping polarization. Besides, the displacement of positive and negative charges due to external electric field produces interfacial polarization.

The above four polarization mechanisms also depend on the frequency of applied electric field as shown in **Figure 2.14**. Electronic polarization is the fastest and occurs at frequencies between 10^{13}-10^{15} Hz as lighter electrons play important role in this mechanism. Atomic polarization can occur at frequencies between 10^{9}-10^{13} Hz due to the involvement of ions. Dipolar polarization involving moments of molecular dipoles occurs at comparatively lower frequencies below 10^{9} Hz. Interface or space polarization takes place at very low frequencies below 100 Hz because this mechanism, involving charge dipoles such as defects, is unable to follow the fast changing applied field. In presence of external electric field, the induced polarization in dielectric material is referred as dielectric behaviour of the dielectric material.

The total polarization (P) can be written as

$$\boldsymbol{P = P_D + P_E + P_A} \text{.....(2.18)}$$

Interfacial polarization cannot be simply added to the total polarization as it occurs at the interfaces and the fields are not well defined at the interfaces. The dipole moment (p) per unit local electric field (E_{loc}) at the molecule is called as molecular polarizability (α).

$$\boldsymbol{p = \alpha E_{loc}} \text{.....(2.19)}$$

For simple dielectrics like gases, local field can be taken same as the macroscopic field. The total molecular polarizability can be written as sum of dipolar polarizability (α_D), electronic polarizability (α_E) and atomic polarizability (α_A).

$$\alpha = \alpha_D + \alpha_E + \alpha_A \text{.....(2.20)}$$

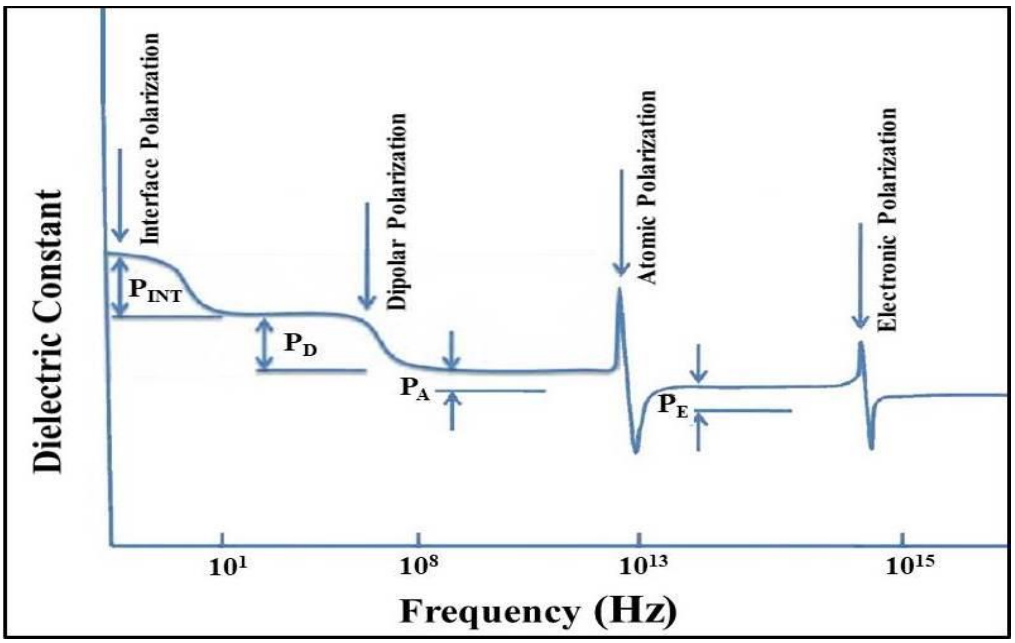

Figure 2.14: Schematic representation of various mechanisms for frequency response of dielectric constant in dielectric materials

2.3.2.2 Theories of Permittivity

Like susceptibility, the dielectric constant (permittivity) is also a measure of the capability of material to store the applied electrical energy in the form of polarization. Depending on the external electrical field, there are two types of permittivity [78], namely (i) static permittivity and (ii) dynamic permittivity. When a dielectric material gets polarized under static electric field, the permittivity of material under this condition is called static permittivity (ε_s). If a dielectric material is placed in an electric field of varying frequency, then with increasing frequency the molecular dipoles cannot orient as fast as the field frequency. Hence, the permittivity of the material drops off with increasing

frequency of applied field. The frequency dependent permittivity of material is known as dynamic permittivity (ε^*). The different theories of static and dynamic permittivity are as follows:

(i) <u>Theories of Static Permittivity:</u> Theories of permittivity refer to the response of the charge distribution to the external electric field. For the concept of static permittivity or dielectric constant, let us consider two plane parallel plates capacitors with area of each plate being 'A', separation 'd' between plates are charged with a surface charge density 'q', one plate being positive and the other negative. Assuming that the space between the plates is vacuum and d << A, a homogeneous electric field (E_0) between plates can be considered and the field strength can be expressed as

$$\boldsymbol{E_0 = 4\pi q = D}\text{.....(2.21)}$$

where D is called the electric displacement or flux density. The potential between the plates is

$$\boldsymbol{\varphi_0 = E_0 * d}\text{.....(2.22)}$$

The capacitance of the system is defined by

$$\boldsymbol{C_0 = \frac{Aq}{\varphi_0} = \frac{Q}{\varphi_0}}\text{.....(2.23)}$$

Now, a dielectric material is placed in the space between plates keeping the charge on the plates constant. Then it is observed that the new capacitance C is

larger than C_0 and new potential φ is lower than φ_0. The static dielectric constant ε_s is defined as

$$\boldsymbol{\varepsilon_s = \frac{\varphi_0}{\varphi} = \frac{C}{C_0}} \text{.....(2.24)}$$

The relation between susceptibility and dielectric constant can be written as

$$\boldsymbol{\chi_e = \varepsilon_s - 1} \text{.....(2.25)}$$

The field strength is decreased to E from its initial value due to the placement of insulating material between plates.

$$\boldsymbol{E_0 = D = \varepsilon_s E} \text{.....(2.26)}$$

Here, D is also known as electric displacement vector. Thus, according to Eq. 2.21 and 2.26, introduction of dielectric material is equivalent to reduction of surface charge density by an amount

$$\boldsymbol{P = q - q' = \left(\frac{E_0}{4\pi}\right) - \left(\frac{E}{4\pi}\right) = \left(\frac{\varepsilon_s E}{4\pi}\right) - \left(\frac{E}{4\pi}\right) = \frac{E}{4\pi}(\varepsilon_s - 1)} \text{.....(2.27)}$$

Here, q is the modified surface charge density. This reduction of surface charge density is caused due to the negative charge induction on positive plates and vice versa in the presence of external electric field. 'P' is known as polarization of material. From Eq. 2.26 and 2.27, it can be written as

$$\boldsymbol{4\pi P + E = E_0 = \varepsilon_s E = D} \text{.....(2.28)}$$

This Eq.2.28 represents the connection between the dielectric constant and the applied electric field. The effective surface charge ±PA produces a net electric moment M of the dielectric which can be written as

$$\boldsymbol{M = PAd = PV}\text{.....(2.29)}$$

Hence, polarization can be defined as dipole moment per unit volume in dielectric material. The amount of polarization can be estimated using different theories discussed as follows:

(a) Clausius-Mossotti Equation: For simple dielectrics such as gases, the effective field at the position of molecule i.e local field (E_{loc}) is same as the external electric field (E) due to little molecular interaction. On the contrary, for dielectric solids and liquids, a given molecule or atom can feel E_{loc} due to dipoles in surrounding medium. The local field contribution for a molecular site with cubic symmetry is shown in Eq. 2.17. If all the molecules have the same polarizability (α_i) and there are N numbers of molecules per unit volume, the polarization can be expressed as

$$\boldsymbol{P = N\alpha_i E_{loc} = N\alpha_i \left(E + \frac{P}{3\varepsilon_0}\right)}\text{.....(2.30)}$$

Where α_i is sum of electronic and atomic polarizability, ε_0 is free space permittivity, E= External Electric field (E_0) + Polarization field (E_p), P is total

polarization of solids. Using Eq. 2.16 , the electrical susceptibility can be written as

$$\chi_e = \frac{P}{\varepsilon_0 E} = \frac{N\alpha_i/\varepsilon_0}{1-N\alpha_i/3\varepsilon_0} \text{.....(2.31)}$$

This expression can be put in the form

$$\frac{\varepsilon_s - 1}{\varepsilon_s + 2} = \frac{N\alpha_i}{3\varepsilon_0} \text{.....(2.32)}$$

This is known as Clausius- Mossotti equation [79] which relates the dielectric constant of a material under electronic and atomic polarization to one of the important microscopic quantity i.e. molecular polarizability. The right hand side of the Eq.2.32 is molecular polarization, purely molecular quantity which gives the electrical properties of molecule. But there are some limitations of this relation. The Clausius-Mossotti relation holds good for non-polar dielectrics only. In case of polar dielectrics the Lorentz field approximation [80] cannot be applied and hence Clausius-Mossotti equation cannot be used.

(b) Debye Theory: Debye [81] has proposed his theory of static dielectric constant using dipolar polarizability. In this theory, the contribution of dipolar polarization of polar dielectrics is considered using classical Boltzman statistics and Langevin function $L(y) = \coth y - \frac{1}{y}$ from the theory of paramagnetism. Debye estimated the temperature dependence of permanent dipole orientation.

Debye calculated the dipolar polarizability as $\alpha_D \propto \frac{1}{T}$ and modified the Clausius-Mossotti equation as

$$\frac{\varepsilon_s - 1}{\varepsilon_s + 2} = \frac{N\alpha_i}{3\varepsilon_0} + \frac{N\alpha_D}{3\varepsilon_0} \text{.....(2.33)}$$

The static dielectric constant of many polar gases and polar liquids has been predicted using Debye theory. However, this theory fails in the case of condensed state of matter. In addition, Debye theory breaks down to predict Mossotti catastrophe. The reason for these failures is the dipole-dipole interaction that cannot be neglected for condensed state of material.

(c) Onsager's Theory: Onsager [82] modified the Debye theory by introducing a cavity concept. This theory is based on the assumption that the molecule is spherical, polar and the sum of the volume of molecules is equal to the total volume of the material. In this new approach, the surroundings of each molecule are considered as homogeneous continuum with the macroscopic properties of the substance. The internal field in the molecule is considered as sum of the spherical cavity field produced due to uniform external applied field in the cavity of molecular dimensions and the reaction field in cavity produced due to polarization induced by dipoles in its surroundings. Onsager's molecular model formed of a sphere with a permanent dipole moment and an isotropic polarizability. On the basis of this model, the connection between molecular dipole moment and static dielectric constant is derived by Onsager. This relation

is obeyed by non-associated polar liquids [82, 83] and weakly bound van der Waals solids. But this theory failed to predict phenomenon of ferroelectricity.

In general, most of the solid dielectrics do not follow local field expressions at sufficiently low frequencies because of the charge carriers such as ions, electrons present in these materials. Therefore, low frequency dielectric permittivity measurement is very difficult. Debye theory and Onsager's theory are known as semi statistical theories where local field expressions are estimated using macroscopic arguments. Kirkwood and then Frohlich used statistical methods to obtain the expression of static permittivity [84-85]. Cole also proposed a theory of static permittivity similar to the Kirkwood theory except in the treatment of direction of polarization [86].

(ii) <u>Theories of Dynamic Permittivity:</u> When a dielectric material is subjected to an alternating electric field, the polarization also varies periodically with time. This happens because dipolar polarization cannot follow the frequency of alternating field and unable to achieve its equilibrium value fast enough. It leads to the decrease in dipole moment per unit volume with increase in frequency. A 'dielectric loss' also appears over a broad band of frequencies. At these high frequencies, no contribution comes to the dielectric constant due to orientation of permanent dipoles. Moreover, a phase lag between the field and dipole orientation develops and energy absorbed by the material from electrical source is dissipated as heat. In order to describe this situation, frequency dependent dielectric constant

(dynamic permittivity or complex dielectric constant) is considered. The complex representation of dielectric constant can be written as

$$\boldsymbol{\varepsilon^* = \varepsilon' - j\varepsilon''} \text{ ……..(2.34)}$$

The real part ε' represents the dielectric constant i.e the ability of dielectric material to store electrical energy from an external electric field and the imaginary part ε'' is known as the dielectric loss. If an alternating electric field of frequency f and angular frequency ω (= 2πf) is expressed as= $\boldsymbol{E_0 e^{j\omega t}}$, then complex permittivity can be written as

$$\boldsymbol{\varepsilon^* = n^2 + \frac{(\varepsilon_s - n^2)}{(1 + j\omega\tau)}} \text{ ……..(2.35)}$$

Which rationalizes to

$$\boldsymbol{\varepsilon' = n^2 + \frac{(\varepsilon_s - n^2)}{(1 + \omega^2\tau^2)}} \text{ ……..(2.36)}$$

$$\boldsymbol{\varepsilon'' = \frac{(\varepsilon_s - n^2)\omega\tau}{(1 + \omega^2\tau^2)}} \text{ ……..(2.37)}$$

Where 'n' is the refractive index of material, τ is the relaxation time and ε_s is static dielectric constant. These Eqs.2.36 and 2.37 are known as Debye or Debye-Drube equations. The dielectric loss will be maximum at frequency ω = 1/τ and maximum value of dielectric loss will be $\boldsymbol{\varepsilon''_{max} = (\varepsilon_s - n^2)/2}$. This indicates at frequency ω = 1/τ, the energy absorption due to phase lag between the polarization and the applied field will be maximum. The loss tangent can be expressed as

$$\tan \delta = \frac{\varepsilon''}{\varepsilon'} \text{ ……..(2.38)}$$

Where, δ is the angle between vector sum of the real and imaginary components of complex permittivity with the real axis (ε′), shown in **Figure 2.15**.

The loss tangent is also known as dissipative factor, reciprocal of which termed as the quality factor of the material. The quality factor is used to evaluate the figure of merit in high frequency applications. Experimental data can be represented by the plot of electrical permittivity or dielectric constant (ε′) and dielectric loss (ε″) with frequency. The data of dielectric constant and loss measurement are also displayed by plotting ε″ against ε′ in a complex plane. In order to represent permittivity or dielectric constant data, different relaxation models such as Cole-Cole model [72], Davidson-Cole model [73], etc. are used.

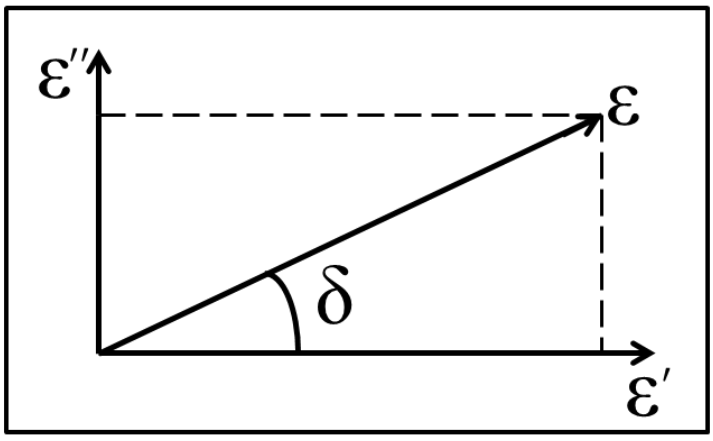

Figure 2.15: Loss tangent vector diagram

2.4References

1. M. Baibich, J. Broto, A. Fert, F. v. Dau, F. Petroff, P. Etienne, G. Greuzet, A. Friederich, and J. Chazelas, Phys. Rev. Lett. **61**, 2472 (1988).
2. G. Binash, P. Grünberg, F. Saurenbach, and W. Zinn, Phys. Rev. B **39**, 4828 (1989).
3. S. A. Wolf, A. Y. Chtchelkanova, D. M. Treger, IBM J. Res. & Dev. **50**, 101 (2006).
4. G. A. Prinz, Science **282**, 1660 (1998).
5. B. Dieny, V. S. Speriosu, S. S. P. Parkin, B. A. Gurney, D. R. Wilhoit, and D. Mauri, Phys. Rev. B **43**, 1297 (1991).
6. W. H. Meiklejohn and C. P. Bean, Phys. Rev. **102**, 1413 (1956).
7. W. H. Meiklejohn and C. P. Bean, Phys. Rev. **105**, 904 (1957).
8. R.J. Cava, J. Mater. Chem **11,** 54 (2001).
9. B. D. Cullity and C. D. Graham, Introduction to Magnetic Materials, 2nd edition, IEEE Press, Wiley Publishing Company, ISBN 978-0-471-47741-9.
10. W. H. Meiklejohn, J. Appl. Phys. **33**, 1328 (1962).
11. P. E. Jönsson, Adv. Chem. Phys. **28**, 191 (2004).
12. J. Vannimenus and G. Toulouse, J. Phys. C: Solid State Physics **10 (18)**, L537 (1977).

13. K. Binder and A.P. Young, Reviews of Modern Physics **58(4)**, 801 (1986).
14. P. A. Joy, P. S. A. Kumar and S. K. Date, J. Phys.: Condens. Matter. **10 (48)**, 11049 (1988).
15. Kurti, N., ed. (1988). Selected Works of Louis Néel. Gordon and Breach. pp. 407–427. ISBN 978-2-88124-300-4
16. D. De, S. Goswami and M. Chakraborty, Journal of magnetism and magnetic materials **565**, 170175 (2023).
17. M. Sasaki, P. E. Jönsson, H. Takayama and H. Mamiya, Phys. Rev. B. **71**, 104405 (2005). doi: 10.1103/PhysRevB.71.104405
18. A. C. Gandhi, R. Selvam, C. L. Cheng and S. Y. Wu, Nanomaterials (Basel) **11(3)**, 648 (2021).
19. J. L. Dormann, R. Cherkaoui, L. Spinu, M. Noguès, F. Lucari, F. D'Orazio, D. Fiorani, A. Garcia, E. Tronc and J. P. Jolivet, J. Magn. Magn. Mater. **187**, L139 (1998).
20. C. Djurberg, P. Svedlindh, P. Nordblad, M. F. Hansen, F. Bødker and S. Mørup, Phys. Rev. Lett. **79**, 5154 (1997).
21. T. Jonsson, P. Svedlindh and M. F. Hansen, Phys. Rev. Lett. **81**, 3976 (1998).
22. T. Jonsson, P. Nordblad and P. Svedlindh, Phys. Rev. B **57**, 497 (2000).
23. S. Giri, M. Patra and S. Majumdar, J. Phys.: Condens. Mater. **23**, 073201 (2011).

24. A. Yelon, in: M. H. Francombe and R. W. Hoffman (Eds.), Physics of Thin Films, Academic Press, New York, **6**, 205 (1971).

25. R. Jungblut, R. Coehoorn, M. T. Johnson, J. aan de Stegge and A. Reinders, J. Appl. Phys. **75**, 6659 (1994).

26. M. Takahashi, A. Yanai, S. Taguchi and T. Suzuki, Jpn. J. Appl. Phys. **19**, 1093 (1980).

27. T. J. Moran, J. M. Gallego and I. K. Schuller, J. Appl. Phys. **78**, 1887 (1995).

28. A. E. Berkowitz and J. H. Greiner, J. Appl. Phys. **36**, 3330 (1965).

29. P. J. van der Zaag, R. M. Wolf, A. R. Ball, C. Bordel, L. F. Feiner and R. Jungblut, J. Magn. Magn. Mater. **148**, 346 (1995).

30. W. C. Cain and M. H. Kryder, J. Appl. Phys. **67**, 5722 (1990).

31. R. K. Zheng, H. Liu, X. X. Zhang, V. A. L. Roy and A. B. Djurisic, Appl. Phys. Lett. **85**, 2589 (2004).

32. A. Matsuzono, S. Terada, H. Ono, A. Furukawa, T. Sone, S. Sasaki, Y. Kakihara, Y. Takeda, N. Chiyokubo and H. Matsuki, J. Appl. Phys. **91**, 7267 (2002).

33. A. Tanaka,Y. Shimizu,Y. Seyama, K. Nagasaka, R. Kondo, H. Oshima, S. Eguchi and H. Kanai, IEEE Trans. Magn. **38**, 84 (2002).

34. B. Dieny, B. A. Gurney, S. E. Lambert, D. Mauri, S. S. P. Parkin, V. S. Speriosu and D. R. Wilhoit, US Patent 5.206.590 (1993).

35. P. M. Baumgart, B. Dieny, B. A. Gurney, J. P. Nozieres, V. S. Speriosu and D. R. Wilhoit, US Patent 5.287.238 (1994).

36. S. Parkin, X. Jiang, C. Kaiser, A. Panchula, K. Roche and M. Samant, Proceeding of the IEEE **91**, 661 (2003).

37. D. Paccard, C. Schlenker, O. Massenet, R. Montmory and A. Yelon, Phys. Status Solidi b **16**, 301 (1966).

38. A. Hoffman, Phys. Rev. Lett. **93**, 097203 (2004).

39. J. Nogués, J. Sort, V. Langlais, V. Skumryev, S. Suriñach, J. S. Muñoz and M. D. Baró, Phys.Rep. **422,** 65 (2005).

40. C. Binek, X. He and S. Polisetty, Phys. Rev. B **72,** 054408 (2005).

41. C. Prados, E. Pina, A. Hernando and A. Montone, J. Phys.: Condens. Matter **14**, 10063 (2002).

42. H. Xi, R. M. White, S. Mao, Z. Gao, Z. Yang and E. Murdock, Phys. Rev. B **64**, 184416 (2001).

43. Ò. Iglesias. A. Labarta and X. Batlle, Journal of Nanoscience and Nanotechnology **8,** 2761 (2008).

44. J. Nogués and I. K. Schuller, J. Magn. Magn. Mater. **192,** 203 (1999).

45. F. Radu and H. Zabel, Springer Tracts Mod. Phys. **227**, 97 (2007).

46. A. P. Malozemoff, J. Appl. Phys. **63,** 3874 (1988).

47. A. E. Berkowitz and K. Takano, J. Magn. Magn. Mater. **200**, 552 (1999).

48. R. L. Stamps, J. Phys. D: Appl. Phys. **33**, R247 (2000).

49. M. Kiwi, J. Magn. Magn. Mater. **234,** 584 (2001).

50. E. C. Stoner and E. P. Wohlfarth, Nature **160**, 650 (1947).

51. E. C. Stoner and E. P. Wohlfarth, Philos Tr R Soc S-A. **240**(826), 599 (1948).

52. R. L. Stamps, J. Phys. D: Appl. Phys. **33**, R247 (2000).

53. J. Nogués, D. Lederman, T. J. Moran and I. K. Schuller, Phys. Rev. Lett. **76**, 4624 (1996).

54. F. Canet, S. Mangin, C. Bellouard and M. Piecuch, Europhys. Lett. **52**, 594 (2000).

55. H. Shi, D. Lederman, N. R. Dilley, R. C. Black, J. Diedrichs, K. Jensen and M. B. Simmonds, J. Appl. Phys. **93**, 8600 (2003).

56. D. Mauri, H. C. Siegmann, P.S. Bagus and E. Kay, J. Appl. Phys. **62,** 3047 (1987).

57. A. P. Malozemoff, Phys. Rev. B **35,** 3679 (1987).

58. N. C. Koon, Phys. Rev. Lett. **78,** 4865 (1997).

59. P. Miltényi, M. Gierlings, J. Keller, B. Beschoten, G. Güntherodt, U. Nowak, and K. D. Usadel, Phys. Rev. Lett. **84,** 4224 (2000).

60. U. Nowak, K. D. Usadel, J. Keller, P. Miltényi, B. Beschoten, and G. Güntherodt, Phys. Rev. B **66,** 014430 (2002).

61. P. Van Musschen Broek, Introduction Philosophion Naturalem, Luchtman, Leiden (1762)

62. M. Faraday, Phil. Trans **128:1,** 79 265 (1837).

63. O. F. Mossoti, Bibl.univ.modena **6**, 193 (1847).

64. R. Clausius, Volume **2** Vieweg. Braunschweigh (1879).

65. P. Debye, *Phys.Z*, **13**, 97 (1912).

66. K. Dutta, S. K. Sit and S. Acharyya, Pramana-J. of Phys. **57(4),** 775 (2001).

67. L. Onsager, *J.Amer.Chem.Soc* **58**, 1486 (1936).

68. J. G. Kirkwood, J. Chem. Phys **7**, 911 (1939).

69. H. Frohlich, Theory of Dielectrics: dielectrics constant and dielectric loss, 2nd ed. Oxford: Clarendon Press,1986, c1958.

70. P. Drude, Z. phys. Chem, **23**, 267 (1897).

71. A. V. Turik and A. S. Bogatin, Functional Materials Letters, **8(4),** 1550035 (2015).

72. K. S. Cole and R. H. Cole, Journal of Chemical phys **9**, 341 (1941).

73. D. W. Davidson and R. H. Cole, J.Chem.Phys **19**, 1484 (1951).

74. G. Williams and D. C. Watt, Trans Faraday Soc **66**, 80 (1970).

75. A. K. Jonsher, Dielectric relaxation in solids, Chelsea dielectric press, London (1983)

76. R. K. Puri and V. K. Babbar, Solid State Physics, S.Chand & Company ltd., ISBN: 81-219-1476-0,code:10 181, Reprinted 2011.

77. C. P.Smyth, Annual Review of Physical Chemistry **17**, 433 (1966).

78. A. J. Dekker, Solid State Physics, Macmillan Publishers India LTD, reprinted 1985-2011

79. S. O. Kasap in Principles of Electronic Materials and devices, Mcgraw – Hill(2006)

80. H. A. Lorentz."Theory of Electrons", Teutorer Verlogsellscharft, Leipzig, 306(1909).

81. P**.** Debye. Polar Molecules, Chemical Catalog Company, New York (1929).

82. L.Onsager, J. Am. Chem. Soc. **50**, 1486 (1936).

83. A. R. VonHippel, Dielectric and waves John wiley &Sons,Newyork (1954)

84. J. G. Kirkwood, J. Chem. Phys. **4**, 492 (1936).

85. H. Frohilich, Theory of Dielectrics, Oxford University Press, London (1949).

86. N. E. Hill, W. E. Vaughan, A. H. Price and M. Davies, Van Nostrand Reinhold Company, London (1969).

3 Studied Materials

A brief description of the studied samples and their properties, applications are focused here.

3.1 Films

A film is the layer of material with thickness ranging from fraction of nanometer to several micrometers on a substrate or bulk surface. Thereby, the functionality of substrate can be modified and increased. Initially, metal film formation by sputtering of cathodes with high energy positive ions [1] can be considered as the beginning of the thin film science. This attracts significant attention in modern day life due to their wide applications in the various fields such as sensor device, storage of solar energy, piezo-electric device, space science applications, optical applications and many more [2-3]. Recently, it has started to play an essential role in high density memory systems of computers, field effect transistor, switching devices, cryogenic applications, nanotechnology, etc [4-6].

The properties of the film differ significantly from those of bulk due to the effect of grain boundaries which is neglected in the bulk state of materials [7]. The properties such as structural, electrical, optical, magnetic, etc., of a film can be controlled by the different deposition procedures, rate of deposition, purity of the material to be deposited, operating conditions, etc. Different deposition techniques can be classified into two main groups, namely, (i) physical deposition

process (magnetron sputtering, physical vapour deposition, molecular beam epitaxy, etc.,) [8-10] and (ii) chemical deposition process (chemical bath deposition, sol-gel, spin coating, dip coating, etc.,) [11-14]. A schematic diagram of film is shown in **Figure 3.1(a)**.

It is important to be noted that depending on the thickness range of film, one can think of two types of film, thin and thick film but no limit of thickness can be defined. A film can be considered as 'thin' if its properties are considerably different from that of the bulk. When the thickness of the thin layer exceeds certain threshold value, the effect of thickness will be minimal [15]. In other words, a film can be considered as 'thin' for one given application while it behaves as 'thick' in another application.

Films can also be characterized into two groups, epitaxial film and granular or polycrystalline film depending on the surface morphology. Unlike epitaxial film, the surface morphology of granular film shows peak like structure under the Atomic Force Microscopy (AFM). The granular film, instead of epitaxial films, can also be used to fulfil growing needs of large storage capacity within a small volume as well as cost-effectiveness of magnetic recording media. Thus, we focus mainly on granular film.

Metal oxide semiconductors are gaining a great interest from scientific and technological points of view. Therefore, in this thesis, we have investigated the magnetic properties along with the structural and morphological properties of

granular NiO and $Ni_{1-x}Zn_xO$ film, fabricated using sol-gel dip coating technique as discussed later.

3.2 Nanoparticles

Since last century, nano-science and nano-technology, growing rapidly worldwide, attract significant attention of researchers as broad and interdisciplinary areas of research. Starting from the major research and development sectors like energy storage devices, pharmaceuticals, etc., to today's high speed personal computers, mobile communications, nano-science and nano-technology become indispensable components, nowadays. The cornerstones of nano-science and nano-technology are nanomaterials. Following the definition used by the National Nanotechnology Initiative in the US, nanostructured materials can be defined as the materials with structural elements, clusters, crystallites or molecules of dimension in the range 1 to 100 nm [16]. Nanomaterials can be classified into three groups depending on the basis of reduction in size of materials in different dimensions, such as (i) 0 dimensions (quantum dots, nanoparticles, etc.,), (ii) 1 dimensions (nanowires, nanotubes, nanorods, etc.,), (iii) 2 dimensions (grapheme, nanofilms, nanolayers, etc.,) and (iv) 3 dimensions (bulk powder, bundles of nanowires, carbon fullerenes, etc.,). Classification of nanomaterials can also be done based on pore dimensions since many applications of absorption and diffusion depend on this parameter.

Generally, there are two main approaches for synthesis of nanomaterials, such as

(i) **Top-Down:** Nanostructure synthesized by reduction of size of bulk materials is known as Top-Down approach. Example-Ball milling, Lithography, Epitaxy, etc.

(ii) **Bottom-Up:** The building of nanomstructures from the atomic level such as atoms and molecules is called Bottom-Up approach. Example- Sol-Gel process, Chemical Reduction methods, etc.

The properties of nanomaterials are significantly different and notably improved from that of bulk materials. This is because of smaller grain sizes of materials, resulting greater surface to volume ratio [17]. There are various properties can be altered by grain size reduction or changing surface area to volume effect. Chemical properties such as catalytic activity, selectivity, efficiency of various chemical reactions, etc., can be improved in nanoscale. The melting point of nanomaterial (thermal properties) can vary with particle sizes. The conductors can behave like semiconductors or insulators due to electron confinement in nanoscale as the energy bands are replaced by discrete energy sates. The size of nanoparticles also influences the optical and magnetic properties. Moreover, doping is another resourceful method to tune the properties of nanomaterials towards the desire direction for intense applications. In this thesis we have studied structural, transport and dielectric properties of $Ni_{1-x}Zn_xO$ and $Zn_{1-x}Al_xO$ nanoparticles using various characterization techniques, discussed later.

3.3 Perovskite Nanoparticles

Chapter 3

Perovskite is named after a Russian nobleman and mineralogist Count Lev Aleksevich Von Perovski [18]. This is a large family of compounds with crystal structures related to the calcium titanium oxide ($CaTiO_3$) structure, first discovered by Gustav Rose in 1839. The perovskite family of oxides have drawn significant attention due to their variety of surprising properties such as superconductivity [19], dielectric properties and ferroelectricity [20], colossal magnetoresistance [21], etc. They also have the ability to accommodate almost all of the elements in the periodic table. The ideal perovskite structure is cubic but it is rarely survived due to interplay between electrons, lattice and spin degrees of freedom. Therefore, distorted perovskites (ABO_3 where A-site is usually cation of alkaline or rare earth element and B-site could be 3d to 5d transition metal cations and O is oxygen anion) with reduced symmetry (trigonal, tetragonal, orthorhombic, etc.) have great industrial importance. Recently, rare earth perovskite and the doped mixed oxides with general composition of RBO_3 (R= rare earth cations) and with $R_{1-x}T_xBO_3$ (T= doped metal ion, x= doping concentration), respectively, have been studied worldwide because of their extraordinary applications such as random access memory [22], sensors [23], wireless communication [24], etc. depending on their peculiar properties.

A typical cubic perovskite crystal structure with general formula ABO_3 is shown in **Figure 3.1(b)**, where A and B are cations of different radii, O is anion. The A ion with 12 fold co-ordination number is slightly larger than B ion with 6 fold co-

ordination number. Generally, divalent A ions occupy the corner position (0, 0, 0) of the cube and are 12 fold coordinated by oxygen anions whereas tetravalent B ions sit in the body centre position $(\frac{1}{2},\frac{1}{2},\frac{1}{2})$ of oxygen octahedral and O ions are at the face centre position $(\frac{1}{2},\frac{1}{2},0)$ of the cubic structure. The structure can be considered as a network of corner shared BO_6 octahedral with all B-O-B bond angles are equal to 180^0. The structural distortion occurs depending on the ratio of A and B ionic sizes and the electronic configuration of the metal ions. Usually, two types of structural distortion are observed in perovskite (i) off-centering of B ion in the BO_6 octahedral occurred due to 'displacive phase transition' (small collective displacements of individual atoms) and (ii) tilting of BO_6 octahedral as a result of order-disorder phase transition [25-26]. Tolerance factor (t^*) can predict which type of distortion will occur in perovskite structure, suggested by Goldschmidt [27] as

$$\boldsymbol{t^* = \frac{(r_A + r_O)}{\sqrt{2}\times(r_B + r_O)}} \text{.....(3.1)}$$

Where r_A and r_B are the ionic radii of the A and B cations, respectively, and r_O is the ionic radius of oxygen anion in Å unit. Tilting mode happens for $t^*<1$, whereas $t^*>1$ indicates off centering of B cations in the BO_6 octahedral.

In this thesis, we have studied structural and magnetic properties of hole doped perovskite $Nd_{0.78}Sr_{0.22}CoO_3$ nanoparticle, since it can be used as a potential candidate to explore the abundant interfacial magnetic phenomena such as phase separation, ferrimagnetic transition, etc.

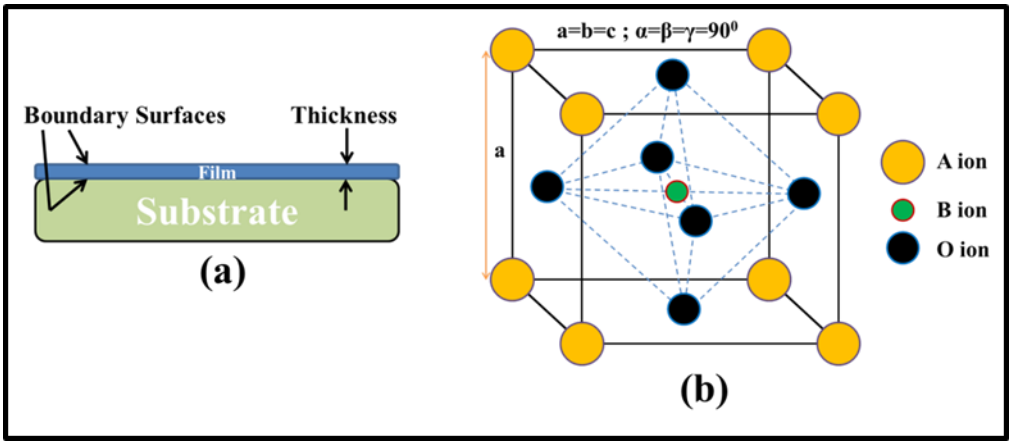

Figure 3.1: (a) Schematic diagram of film (b) Schematic diagram of ideal Perovskite structure

3.4 References

1. W. R. Grove, Phil. Trans. Roy.Soc. London, **142** (1852) 87-101.
2. L. Jogschies, D. Klaas, R. Kruppe, J. Rittinger, P. Taptimthong, A. Wienecke, L. Rissing, M. C. Wurz, Sensors, **15** (2015) 28665-28689.
3. D. M. Mattox, Journal of Vacuum Science and Technology, **13** (1976) 127-134.
4. J. C. S. Kools, IEEE Trans. Magn. **32 (4)** (1996) 3165-3184.
5. A. Lotnyk, M. Behrens, B. Rauschenbach, Nanoscale Advances, **1** (2019) 3836-3857.
6. R. L. Patterson, A. Hammoud, P. Fialla, Journal of Materials Science: Materials in Electronics, **13** (2002) 363-365.
7. S. Yahiaoui, Magister Thesis, Biskra University, (2014), Algeria.

8. A. M. Reddya, A. S. Reddyb, P. S. Reddya, Physics Procedia, **49** (2013) 9-14.
9. K. Reichelt, X. Jiang, Thin Solid Films, **191(1)** (1990) 91-126.
10. D. C. Look, D. C. Reynolds, C. W. Litton, R. L. Jones, D. B. Eason, G. Cantwell, Applied Physics Letter, Vol. **81** No. **10** (2002) 1830-1832.
11. J. C. Osuwa, G. I. Onyejiuwa, Journal of Ovonic Research, vol. **9** no. **1** (2013) 9-15.
12. R. C. Korošec, P. Bukovec, Acta Chim. Slov, **53** (2006) 136-147.
13. D. J. Estes, M. Mayer, Colloids and Surfaces B: Biointerfaces, **42** (2005) 115-123.
14. P. Baudry, A. C. M. Rodrigues, M. A. Aegerter and L. O. Bulhões, Journal of Non-Crystalline Solids, **121** (1990) 319-322.
15. D. Royer and E. Dieulesaint, Edition Masson, Tome 2, (1999), France.
16. A. S. Edelstein (ed), Nanomaterials: Synthesis, Properties and Applications, IOP publishing, Bristol, (1999).
17. J. R. Weertman, R. S. Averback, Nanomaterials: Synthesis, Properties and Applications, A. S. Edelstein, R. C. Cammarata (eds), IOP publishing, London, (1996) 323.
18. Z. Cheng, J. Lin, Cryst. Eng. Comm., **12** (2010) 2646-2662.
19. Y. Maeno, H. Hashimoto, K. Yoshida, S. Nishizaki, T. Fujita, J. Bednorz, F. Lichtenberg, Nature, **372** (1994) 532-534.

20. G. Samara, Ferroelectrics, **2** (1971) 277-289.

21. A. P. Ramirez, Journal of Physics: Condensed Matter, **9** (1997) 8171-8199.

22. A. Kingon, S. Streiffer, C. Basceri, S. Summerfelt, Mrs Bulletin, **21** (1996) 46-52.

23. H. Obayashi, Y. Sakurai, T. Gejo, Journal of Solid State Chemistry, **17** (1976) 299-303.

24. M. T. Sebastian, Dielectric materials for wireless communication, Elsevier, 2010.

25. N. Ramadass, Materials Science and Engineering, **36** (1978) 231-239.

26. E. Fatuzzo, W. J. Merz, Ferroelectricity, North-Holland Pub. Co., 1967.

27. S. Švarcová, K. Wiik, J. Tolchard, H.J. Bouwmeester, T. Grande, Solid State Ionics, 178 (2008) 1787-1791.

Chapter 4

4 Experimental Details and Measurements

A brief description of the techniques of sample preparation, procedures and instruments used to characterize the structural, topological, optical, dielectric and magnetic properties of samples are discussed here. The sample characterizations and investigations of dielectric and magnetic properties have been performed in the laboratories of Jadavpur University, Indian Association for the Cultivation of Science (IACS) and Saha Institute of Nuclear Physics (SINP).

4.1 Sample Preparation

4.1.1 Dip Coating

Dip coating technique [1] can be described as a process where the substrate to be coated is immersed in a precursor solution and then withdrawn with a well-defined withdrawal speed under controlled temperature and atmospheric conditions. It is a simple, low-cost, reliable and reproducible method for deposition of a film on the substrate. This process involves few stages as shown in **Figure 4.1(a)**. In the figure, the first stage represents the 'immersion' in which substrate is immersed into the precursor solution with a constant speed. Second stage indicates 'start-up' in which the substrate is kept into solution for a while and is then pulled up. 'Deposition' is the third stage where a thin layer is deposited itself on the substrate and thickness of the coating is determined by withdrawal speed. Excess liquid will be drained from the surface of substrate, named

'Drainage' and the solvent evaporates from the solution and forms thin layer film, known as 'Evaporation'. Both Drainage and Evaporation are represented by stage four in the **Figure 4.1(a)**. A large variety of films having different structures and thicknesses are fabricated by controlling many factors such as withdrawal speed, number of dipping cycles, submersion time, composition of solution, temperature and environments, substrate surface, etc. Dip coating are used in multilayer sensor coating, sol-gel nanoparticle coating, self-assembled monolayers, layer by layer nanoparticle assemblies, etc.

4.1.2 Chemical Precipitation method

Chemical precipitation process [2] is one of the most useful methods to separate solid product from a precursor solution either by converting the product into an insoluble form or by changing the composition of the solvent to reduce the solubility of the product in it. A calculated amount of reactants (metal oxide or nitrate powder) are mixed together into a solvent, such as deionized water or ethanol, of a particular volume, and thereby a homogeneous mixture is formed by continuous stirring at fixed temperature. A solvent in which the product of precursor solution is insoluble, is termed as anti-solvent that is also added in the above-mentioned mixture. As a result, drastic reduction of the solubility of product causes precipitation of product and the precipitation free solution, named supernatant, remains above the precipitation. Thereafter, the precipitate is easily

separated by filtration or centrifugation. Finally, the product is dried at required temperature. **Figure 4.1(b)** represents the chemical deposition method.

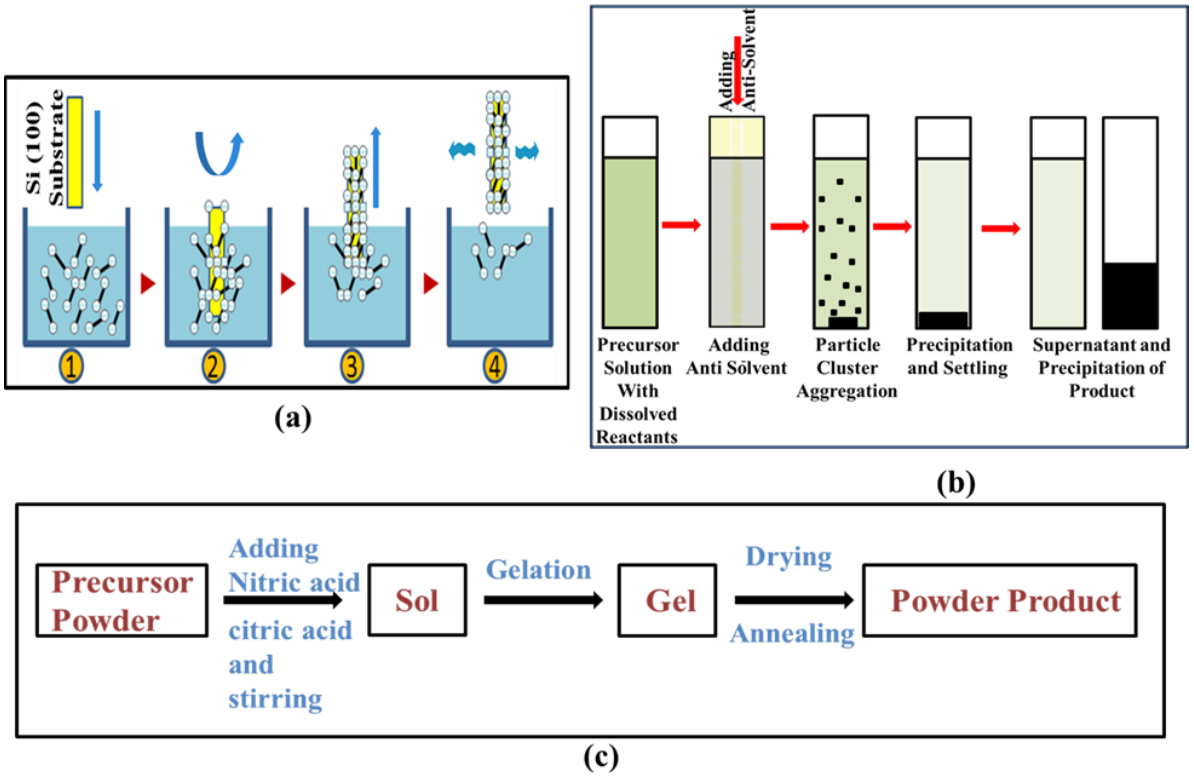

Figure 4.1: (a) Stages of Dip Coating Process (b) Different stages of chemical precipitation process (c) Process of powder sample preparation by sol-gel technique.

4.1.3 Sol-Gel Citrate Precursor Technique

Sol-gel [3] is a chemical solution process which is initially used to prepare metal oxide nanoparticles and later in preparation of ceramics, glass-materials, etc. in the form of thin film or powder. In this process, a 'sol' is a colloidal solution which evolves gradually towards the formation of a 'gel' diphasic system containing both liquid and solid phases. A calculated amount of reagents such as metal oxide powder are dissolved in diluted nitric acid to form nitrate solution of reagents. A required amount of citric acid is added into it to form citrates of

reagents considering that only two citrate ions take part in the chemical bonding with ions of reagents. In order to get citrate precursor powder, the solution is slowly evaporated for long time and finally it is annealed at suitable temperature and environment for a certain time to get the desired product. For thin film preparation, prepared substrate is dipped into solution in dip coating technique or solution is dropped on rotating substrate in spin coating technique. Stages of sol-gel technique for preparation of powder sample are shown in **Figure 4.1(c)**.

4.2 Structural and morphological characterization of the samples

The studied samples are thus prepared using the above mentioned techniques. In order to characterize the structural and morphological details of the samples, different characterization techniques are performed and discussed below.

4.2.1 X-Ray Diffraction (XRD)

X-Ray diffraction (XRD) process [4] is an analytical characterization technique initially used for phase identification of crystalline material. Information on unit cell dimensions about crystallinity, orientation of different planes, lattice strain, different bonds and their length, presence of defects, mean position of atoms, grain size and many others can be obtained from this study. X-ray is an electromagnetic wave, discovered by W.C. Rontgen in 1985 [4]. Since the wavelength of X-ray lies in between 0.01 and 10 nm, which is of the order of

typical interatomic distances, X-rays are suitable for probing the sample such as thin film, nanomaterial, etc.

X-ray diffractometer has three basic components: an X-ray tube, a sample holder and X-ray detector. Continuous and characteristic X-rays are produced in X-ray tube using bremsstrahlung process and electron transition between shells, respectively. A target, commonly copper, is taken for single crystal diffraction. The diffracted X-rays, in general, CuK_α radiation with wavelength 1.5418 Å, are filtered for producing monochromatic radiation and probed on sample. The interaction between incident rays and the sample results constructive interference, satisfying Bragg's Law, defined as

$$\boldsymbol{2d_{hkl}\sin\theta = n\lambda}\text{.....(4.1)}$$

Where d_{hkl} isthe interplaner distance of parallel planes (hkl) of sample, θ is the diffraction angle or Bragg's angle of X-ray (generally Cu K_α) of wavelength λ and n is the order of the diffraction. A schematic representation of the diffraction and interference processes is shown in **Figure 4.2(a)**. These diffracted X-rays are then detected, processed, counted and corresponding intensity is continuously recorded. In order to find all possible directions of diffraction of the lattice, the sample is scanned through a range of 2θ angles. A peak in intensity occurs for lattice planes with d_{hkl} spacing satisfying Bragg's law. The structural investigation is done by comparing the d_{hkl} spacing estimated from XRD pattern with the internationally recognized database (JCPDS).

The crystalline size can be determined from Scherrer's formula, later modified by Williamson and Hall [5], and defined as

$$D = \frac{0.98\lambda}{\beta \cos(\theta)} \text{.....(4.2)}$$

and modified form is

$$\beta \cos(\theta) = \frac{0.98\lambda}{D} + 2\varepsilon \sin(\theta) \text{.....(4.3)}$$

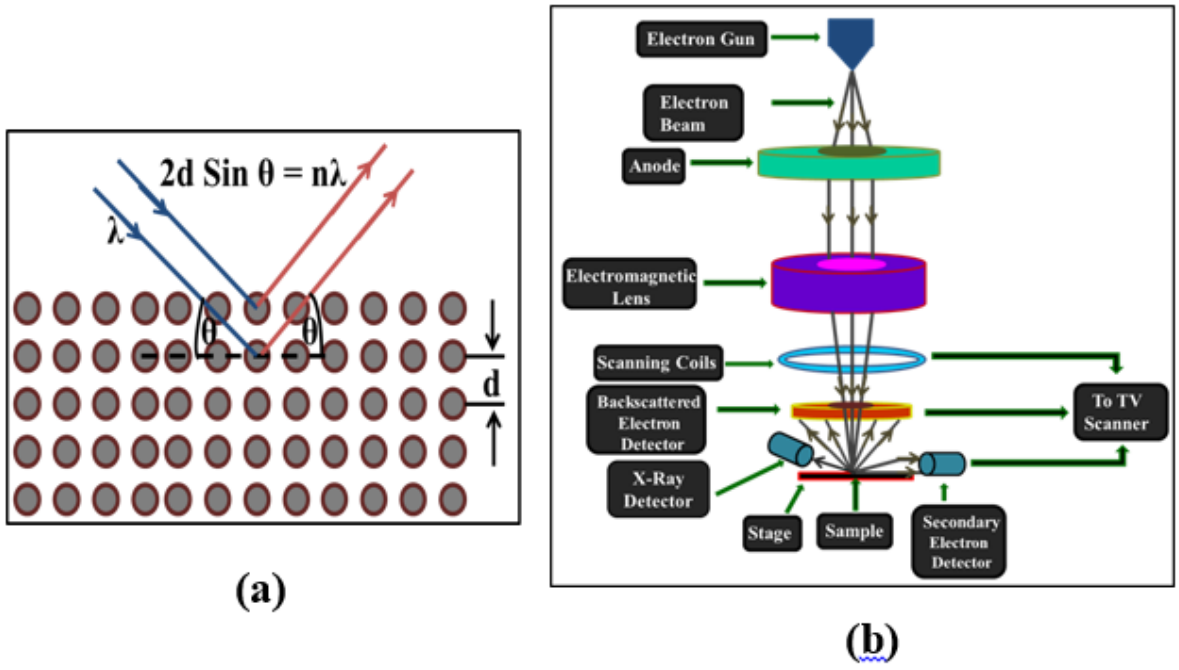

Figure 4.2: (a) Schematic diagram of X-ray diffraction (b) Schematic representation of SEM

Here β, D, λ, ε and θ represent FWHM of the peak in radian, size of the crystallite in the direction perpendicular to the reflecting planes, wavelength of the X-ray, microstrain and diffraction angle, respectively. Lattice parameter (a_{hkl}) can also be estimated from interplanar spacing (d_{hkl}) using Bragg's law. Interplanar spacing (d_{hkl}) is derived from the experimental mean peak position following the equation

$$d_{hkl} = \frac{\lambda}{2\sin\theta} \text{.....(4.4)}$$

Where θ and λ are the diffraction angle and wavelength of the X-ray, respectively. Using (hkl) parameters and d_{hkl}, a_{hkl} for cubic system can be calculated as follows

$$d_{hkl} = \frac{a_{hkl}}{\sqrt{h^2+k^2+l^2}} \text{.....(4.5)}$$

Besides, a single crystal of small dimension or materials with poor crystallinity can be analysed by several other methods such as fiber diffraction, powder diffraction and small-angle X-ray scattering (SAXS). Glancing incidence X-Ray diffraction (GIXRD) is used for analysis of polycrystalline thin film. X-Ray reflectivity (XRR) provides wealth information about interfacial properties of near-surface regime of materials and layered structures.

All of our works discussed in this thesis are characterized by X-ray powder diffractometer BRUKER D-8 ADVANCE.

4.2.2 Field Emission Scanning Electron Microscope (FESEM)

High resolution (as low as ~ 1 nm) three dimensional images of morphology of samples, size and shape of the particle is obtained from Field Emission Scanning Electron Microscope (FESEM). There is a basic difference between FESEM and SEM. In FESEM, a field emission electron gun is used, whereas the electrons are produced thermoionically by heating up a W or LaB_6 cathode in conventional Scanning Electron Microscope (SEM). High resolution image formation by producing much smaller diameter electron beam (< 100 Å) is the advantage of

FESEM compared to SEM. As a result, conducting coating on insulating materials becomes less important. The schematic representation of SEM process is depicted in **Figure 4.2(b)**. The electron beam from electron gun moves in a vertical path through the column of the microscope in ultra-high vacuum. Then electron beam, focused by electromagnetic lens, is moved on the sample by scanning coils. When the electron beam is incident on sample, the atoms of sample are ionized and the secondary electrons are produced. A certain amount of electrons (in the electron beam) are scattered elastically in backward direction due to Coulomb repulsion between electron beam and electron clouds of atoms in the sample. These elastically scattered electrons are known as backscattered electrons. The X-rays due to electronic transitions of atoms in the sample, secondary electrons and backscattered electrons are the main signals detected by corresponding detectors. The secondary and backscattered electrons are collected and converted into two dimensional intensity distributions on cathode ray screen as signal which gives the information regarding the topology of the sample. On the other hand, X-ray signals give the information regarding compositions of the sample. It should be noted that the resolution of the images of topology of sample obtained by secondary electrons is much better than that of obtained by backscattered electrons. Therefore, we concentrate on collecting secondary electrons and also a very thin layer (1.5-3.0 nm) of gold is deposited on sample

in order to make it highly conducting before taking image to avoid any damage of samples. In our research works, FE-SEM (JEOL, JSM-7601F) is used.

4.2.3 Tunneling Electron Microscopy (TEM)

Alike SEM, there is another important technique in order to get morphological and crystalline information of the sample, named Tunnelling Electron Microscope (TEM). A schematic arrangement of TEM is shown in **Figure 4.3(a)**. Initially, sample is well dispersed in ethyl alcohol and put it drop wise (not more than one or two drops) on a carbon coated copper grid. Excess sample can restrain the electron beam from transmitting through the specimen. Finally, grid is kept under the microscope after drying in air. In this technique, high energy electron beam is passed through the ultra-thin sample following interactions with the atoms. These transmitted electrons can carry the structural information of sample. There are two modes of observation which are diffraction mode and image mode. In diffraction mode, transmitted electrons are analysed and a diffraction pattern is obtained on fluorescent screen. This pattern will be a spot pattern for single crystal, whereas polycrystalline will produce a ring pattern. Highly magnified image of illuminated sample surface is obtained from the image mode. TEM produces a high resolution (1 nm), black and white image, generated by adjusting the voltage of the electron gun as well as changing the electromagnetic wavelength via the solenoids. Electron Dispersive Spectroscopy (EDS) unit is an additional attachment with TEM to obtain the information about the relative ratio

of the elements by which sample is composed. Moreover, another kind of TEM, High Resolution TEM (HRTEM) is used to study defects, interplanar spacing, interfaces, etc. In our research works, TEM JEOL (Model: JEM, 2100F) is used for morphological characterization of sample.

4.2.4 Atomic Force Microscopy (AFM)

Atomic Force Microscopy (AFM) is one of the scanning probe microscopy (SPM) with high resolution of the order of fractions of a nanometre. In AFM, a cantilever with a sharp tip at its end acts as a probe to scan the specimen surface. In order to get local properties of the sample, such as height, magnetism, friction, etc., the probe raster-scans over a small area of the sample, shown in **Figure 4.3(b)**. In general, the probe is a sharp tip having 3-6 μm tall pyramid like shape with 15-40 nm base radius. AFM measures the vertical and lateral deflections of the cantilever with resolution 0.1 nm and ~ 30 nm, respectively, using optical lever. A laser beam strikes and reflected by cantilever. This reflected laser is incident on position sensitive four-segment photo-detector. Therefore, angular deflections of the cantilever are estimated from the difference in signals of the segments of photo-detector. This results three dimensional image of sample surface displayed as a pseudo colour plot. AFM is also used to measure the mechanical properties of the sample, such as Young's modulus, stiffness, etc., following the measurement of force between the probe and the sample as a function of their

mutual separation. The surface topology of our samples is probed by AFM, Veeco-diCP II.

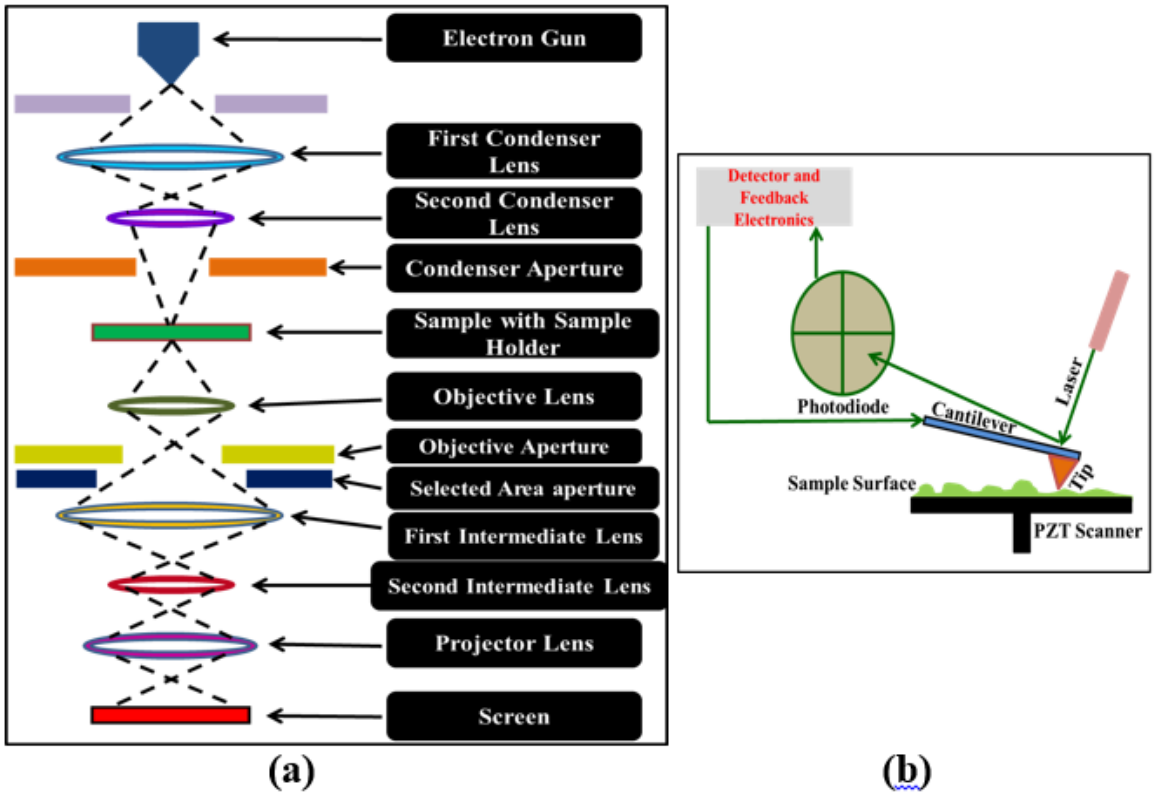

Figure 4.3: (a) Schematic representation of TEM, (b) Schematic representation of AFM

4.2.5 Softwares

In this thesis, several softwares are used to analyse the experimental data. The scientific graphing and data analysing are performed using ORIGIN software. Rietveld refinement procedure is executed on XRD data to obtain refined values of the structural and microstructural parameters using MAUD software. VESTA software is used to find the detail microstructural properties such as bond angle, bond length, atomic positions, etc. Measurement of the interplanar distance,

particle size, etc (fraction of nm order of distances) from TEM data are done by ImageJ program. For graphing and analysing the impedance data, ZView software is used.

4.3 Optical Properties Characterization: UV-Vis Spectroscopy

Ultraviolet visible spectroscopy (UV-Vis) is an important tool for studying optical properties such as band gap, purity of substance, detection of functional group, etc. of samples. Basically, spectroscopy is related to the interaction between matter and incident light. Molecules containing π-electrons or non-bonding electrons (n-electrons) can absorb the energy in the form of ultraviolet or visible light. This results an excitation of the electrons from ground state to higher energy state. This is why it is also known as electronic spectroscopy. The energy difference between the higher state and the ground state must be equal to the energy absorbed. The basic principle of UV-Vis follows the Beer-Lambert Law [6] according to which whenever a beam of monochromatic light is passed through a solution having absorbing substance, the absorbance of the solution is directly proportional to the concentration of the solution and the path length through the sample. This law is defined as

$$\boldsymbol{A = \log_{10} \frac{I_0}{I} = \varepsilon CL} \text{.....(4.6)}$$

where 'A' is the absorbance, I_0 and I refer to the intensity of incident light upon a sample cell and the intensity of light departing the sample cell, respectively, C

stands for the concentration of the absorbing substance, L is the path length through the sample and ε is the molar absorptivity. The optical band gap of the material can be determined from the fundamental absorption corresponding to the transition from valence band to conduction band. Electromagnetic radiations wavelength between 190-800 nm (190-400 nm is UV region and 400-800 nm is visible region) is used for this absorption spectroscopy. The relation between absorption coefficient and incident photon energy for a direct band gap system [7] can be expressed as

$$(\boldsymbol{\alpha h\nu})^{\mathbf{2}} = \boldsymbol{A}\left(\boldsymbol{h\nu} - \boldsymbol{E_g}\right)\text{.....(4.7)}$$

Where E_g is the band gap of the material, α is the absorption coefficient of the material, hν is the energy of incident radiation. The band gap can be estimated from the plot of $(\alpha h\nu)^2$ versus hν, known as Tauc Plot. In this thesis, UV-Vis (Shimadzu, UV 2401PC) is used for band gap measurements.

4.4 Dielectric Properties Characterization

Dielectric properties of the studied materials have been measured using a LCR meter (E4980A LCR meter-Agilent technologies). All the instruments are interfaced to a remote computer and data recording is automatically done by this. An alternating current (ac) signal of fixed amplitude (1 V is used in our work) is provided by the LCR meter and the response is estimated by the system of four probe coaxial cables in the frequency range 20 Hz – 2 MHz and 0-40 V direct current (dc) bias field range, according to requirement. Zero correction of the

instrument and connections with standard protocols are performed to nullify the presence of the stray wiring, conductance and capacitance. Both static and dynamic dielectric permittivity, impedance and electric modulus are the important parameters associated with the analysis of dielectric properties of the sample.

In order to study dielectric properties, sample is pressed into pellet mechanically under controlled pressure at room temperature and sintered at 100^0C for 30 min before electrical connection done. The electrical contacts are fabricated using silver paint coating on parallel opposite surfaces of the pelletized sample. Therefore, sample acts as capacitor. Capacitor is a commonly used dielectric, having electrically insulating material between two metallic plates. If a static voltage (V) is applied across a capacitor with capacitance (C), then the charge stored on the plates of capacitor can be written as

$$\boldsymbol{Q = CV} \text{.....(4.8)}$$

If the permittivity of the material kept between conducting plates of capacitor be 'ε', the area of each plates be 'A' and distance between them be 'd', then the capacitance of parallel plate capacitor is defined as

$$\boldsymbol{C = {\varepsilon A}/{d} = {K\varepsilon_0 A}/{d}} \text{.....(4.9)}$$

Where 'ε_0' represents free space permittivity of value 8.85×10^{-12} F/m and 'K' is defined as relative permittivity or dielectric constant of the dielectric material. Dielectric constant is a dimensionless quantity. When alternating voltage is

applied across the dielectric medium, then applied field's frequency (f) dependent dielectric constant has to be considered. The complex dielectric is defined as

$$\boldsymbol{\varepsilon^* = \varepsilon' - j\varepsilon''} \text{.....(4.10)}$$

The real part ε' represents the dielectric constant and the imaginary part ε'' is known as the dielectric loss. The real and imaginary part can be written as

$$\boldsymbol{\varepsilon'' = \frac{Gd}{\omega \varepsilon_0 A}} \text{.....(4.11)}$$

Where G and ω are the ac conductance and angular frequency (= 2πf) of the input ac signal, respectively. The measurement of energy dissipated per cycle is represented as dielectric loss tangent which can be written as

$$\boldsymbol{\tan\delta = \varepsilon''/\varepsilon' = \frac{G}{\omega C}} \text{.....(4.12)}$$

The complex impedance is defined as $Z^* = Z' - jZ''$ where Z' and Z'' are the real and imaginary part of complex impedance. Z' and Z'' can be written as

$$\boldsymbol{Z' = \frac{G}{G^2+\omega^2C^2}} \text{ ..... (4.13)} \quad \& \quad \boldsymbol{Z'' = \frac{\omega C}{G^2+\omega^2C^2}} \text{.....(4.14)}$$

The ac conductivity of the sample can be defined as

$$\boldsymbol{\sigma_{ac} = \omega K \varepsilon_0 \tan\delta = \frac{\omega C d \tan\delta}{A}} \text{.....(4.15)}$$

4.5 Magnetic Properties Characterization

4.5.1 SQUID and Vibrating Sample Magnetometry (VSM)

Vibrating Sample Magnetometer (VSM) and Superconducting Quantum Interference Device (SQUID) are the most widely used magnetometers for magnetic properties characterization of materials.

VSM: The measurement of magnetization of a magnetic sample by VSM is based on the induction of an electrical signal due to the movement of the sample inside a pair of 'detection' or 'pick up' coils. If the sample executes sinusoidal vibration inside the coils, then according to Faraday's law, the measured signal (ε) of induction or induced voltage is related with magnetic moment (m) of sample and frequency of oscillation as follows

$$\boldsymbol{\varepsilon = -\frac{d\varphi}{dt} \propto m \sin(\omega t)} \text{.....(4.16)}$$

Where dφ/dt is the rate of change of flux passing through the coils. The setup has to be calibrated with a sample of known magnetic properties and dimension same as measured sample in order to calculate magnetic moment from measured induced voltage. One of the important components of VSM is lock-in amplifier which has ability to filter the signal ($\geq 10^{-6}$ emu) to reduce noise. The two detection coils with opposite orientation are used in series instead of one to avoid the induction of a signal in the coil by changing external magnetic field. These coils are kept perpendicularly with external magnetic field whereas sample is oriented parallel with the field, shown in **Figure 4.4**. In addition, a small cryostat is attached inside the coils to execute measurements at very low temperature (~ 4 K). The setup used for our measurements is VSM-J4252 system.

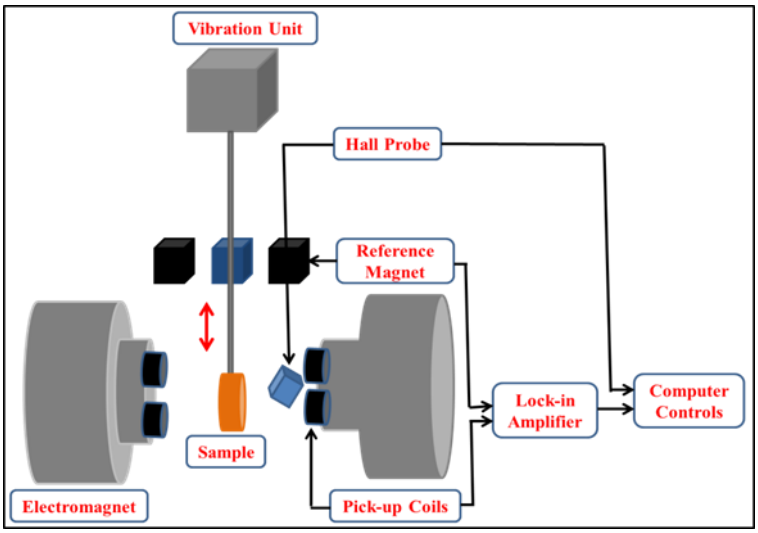

Figure 4.4: Schematic diagram of VSM

SQUID: SQUID magnetometer is one of the most effective and sensitive ways of measuring magnetic properties of magnetic sample. A schematic diagram of SQUID is shown in **Figure 4.5**. It is based on superconducting loops containing Josephson junctions. SQUID are sensitive enough to detect incredibly small magnetic field (~ 10^{-18} T). Direct current (DC) and radio frequency (RF) SQUID are the two main types of SQUID.

The DC SQUID works with two Josephson junctions in parallel in a superconducting loop. It is based on the DC Josephson effect. Besides, RF SQUID has only one Josephson junction which makes them cheaper but less sensitive than former one. If a weak electrical contact exists between two superconductors, the electrical current density through the weak contact depends on the phase difference ($\Delta\varphi$) of the two interfering superconducting wave functions and rate of change of $\Delta\varphi$ is correlated with the voltage across this weak contact. This $\Delta\varphi$ is influenced by the magnetic flux, applied to the

superconducting ring with one or two weak contacts. The magnetic flux (Φ) results current flow through the ring and a RF voltage across the circuit is developed. Thus, the magnetic flux and voltage across weak contact are related to each other. As a result, such a structure can be used to convert magnetic flux into an electrical voltage. This is the basic working principle of a SQUID magnetometer.

Pure niobium or lead alloy with 10% gold or indium is used as superconducting material for SQUID because pure lead is unstable in repeatedly varying temperature. The entire device is cooled with liquid helium at very low temperature (few degrees of absolute zero) to maintain superconductivity. The most common commercial use of SQUID is in magnetic property measurement system (MPMS). SQUIDs are also used as detectors to perform magnetic resonance imaging (MRI). With the development in superconductor technology, SQUID becomes useful in prediction of earthquake, exploration of minerals, surveying geothermal energy, etc.

In our thesis work, magnetization measurements of samples are performed in a commercial SQUID magnetometer, Quantum Design-MPMS-7 which can

produce magnetic field upto 7 T and can be operate at the temperature range 2 to 400 K.

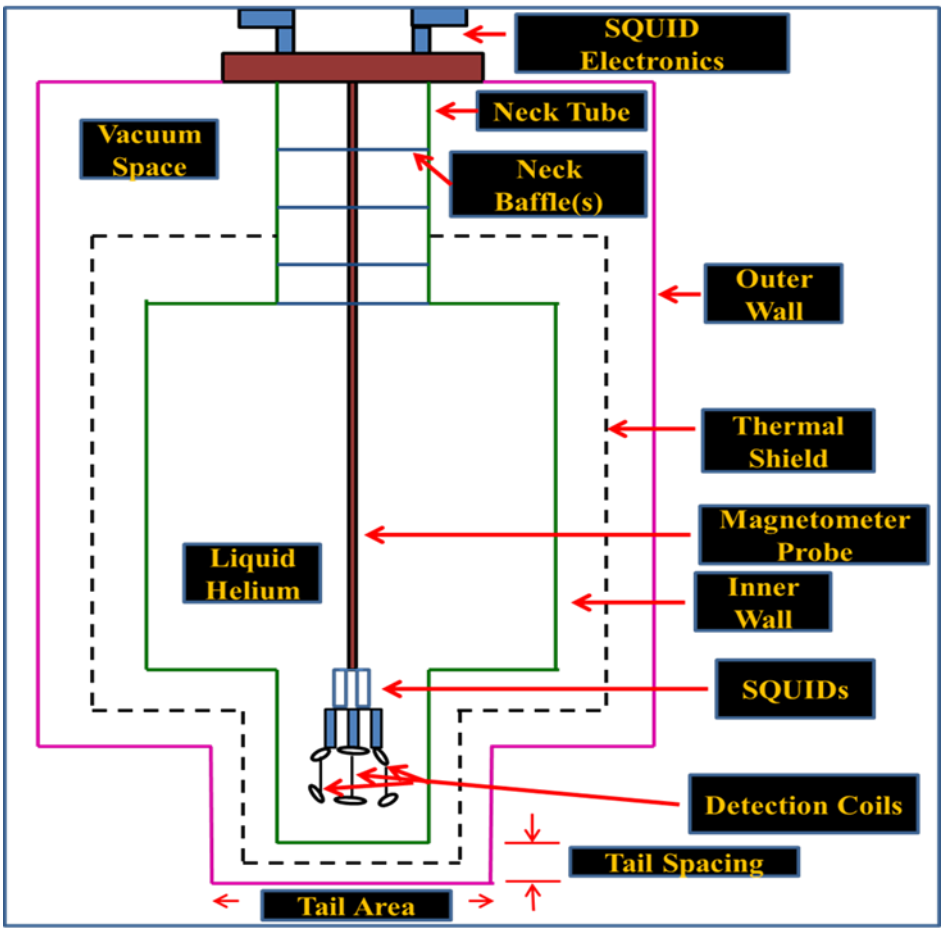

Figure 4.5: Schematic diagram of SQUID

4.5.2 DC Magnetization

DC magnetic measurements of the sample are represented by variation of magnetization (M) of sample as a function of temperature (T) and applied magnetic field (H). These measurements are executed following two major protocols, viz (i) Zero Field Cooled Heating (ZFCH) and (ii) Field Cooled Heating (FCH). According to first protocol, the sample at room temperature (RT) is cooled down to the lowest temperature without applying magnetic field, known

as Zero Field Cooling (ZFC). The data are recorded during heating of the sample to preferred temperature after switching on a required magnetic field. On the contrary, in second protocol, the sample at room temperature (RT) is cooled down to the lowest temperature in presence of finite magnetic field, known as Field Cooling (FC). After achieving FC condition, the data recording are performed during heating cycle when magnetic field is switched on.

4.5.3 Exchange Bias Effect

Exchange bias (EB) effect is found in low dimensional ferromagnetic (FM) materials having interface with an antiferromagnetic (AFM) following FC below Neel temperature (T_N) of AFM component. It is manifested by the shifting and broadening of hysteresis loop of the FM component. A detail discussion is done in chapter 2 section 2.2. The EB field (H_{EB}) and coercivity (H_C) can be expressed as

$$\boldsymbol{H_{EB} = \frac{(H_{C1}+H_{C2})}{2}} \text{.....(4.17)}$$

$$\boldsymbol{H_C = \frac{(H_{C1}-H_{C2})}{2}} \text{.....(4.18)}$$

Where H_{C1} and H_{C2} represent the coercive fields of the ascending and descending branch of hysteresis loop, respectively, shown in **Figure 4.6**. In addition, the remanent magnetization (M_r) and the vertical shift of hysteresis loop (M_{EB}) can be represented as

$$\boldsymbol{M_{EB} = \frac{(M_{r1}+M_{r2})}{2}} \text{.....(4.19)}$$

$$M_r = \frac{(M_{r1} - M_{r2})}{2} \text{.....(4.20)}$$

Where M_{r1} and M_{r2} represent the magnetization with positive and negative points of intersection with H=0 Oe, respectively, as mentioned in Fig.4.6.

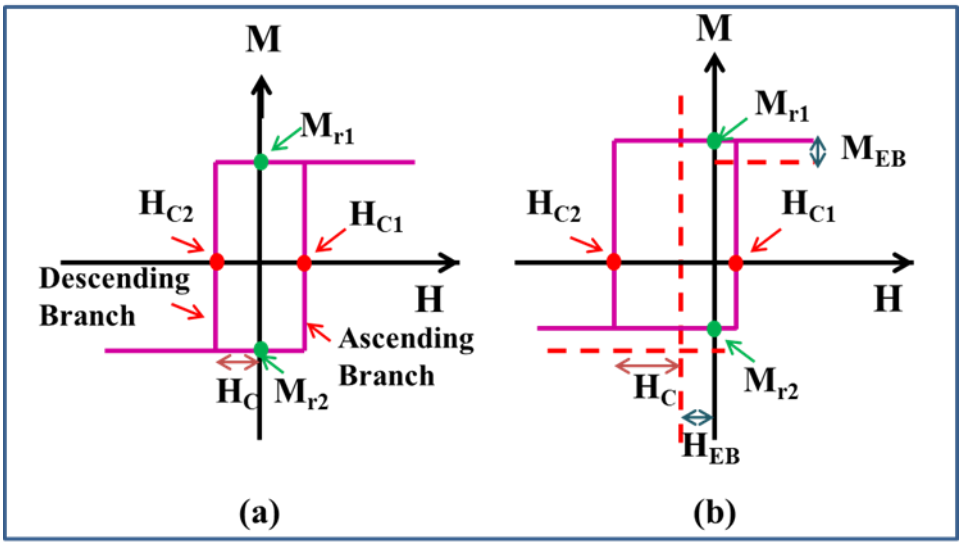

Figure 4.6: Schematic representation of the hysteresis loop with characteristics fields (H_C and H_{EB}), remanent magnetizations (M_{r1} and M_{r2}) and vertical shifting of Hysteresis loop (M_{EB}) of a FM (a) in the absence of EB effect and (b) after the induction of EB effect

4.5.4 Magnetic Memory Measurement

One of the important magnetic phenomena is magnetic memory effect. This happens due to interparticle long-range magnetic ordering at low temperatures. It is basically the ability of magneto-sensitive materials to memorize the information about magnetic moment depending on different protocols.

Magnetic memory measurement is performed both in ZFC and FC protocols [8-9]. Both the protocols are alike except the cooling of sample is done in presence of magnetic field in FC mode whereas it is done without applying magnetic field in ZFC mode. The sample is cooled to lowest temperature with a constant rate

following several numbers of halts at different temperatures (T_{wait}) for a certain time (t_{wait}). For FC mode, magnetic field is switched off during waiting process. After completion of FC process, the magnetic response is recorded during the heating cycle of sample with same rate as cooling process applying a magnetic field. Intriguingly, the magnetic moment shows a cusp or steps like nature at those temperatures (T_{wait}) where pause of the FC process has been done, provided this occurs only below the blocking temperature (T_B) of the sample [10]. Despite the continuous heating, the appearance of steps at T_{wait} in the M(T) curve in FCH process is the signature of memory effect. This is known as FCH memory which can also occur due to extrinsic effect [11]. Therefore, memory effect has to be confirmed by executing the measurement following ZFC protocols which is the definite signature of a glassy magnetic state originating from cooperative spin-spin interaction [9]. Memory effect in FC and ZFC protocols are both shown by spin-glass whereas a weakly interacting super paramagnetic material shows memory effect only in FC protocol [12]. Memory effect measurement can also be investigated by M(t) curve where t is the time. It is important to state that the system can memorize information in the vicinity of temperatures (T_{wait}) at which the information has been stored. In this thesis, we have studied the magnetic memory effect of $Nd_{0.78}Sr_{0.22}CoO_3$.

4.6 References

1. J. Matyas, R. Olejnik, P. Slobodian and Z. Spitalsky, International workshop on the applicationofnanomaterials, Nov.2016.
2. N. Giri, A. Mondal, S. sarkar and R. Ray, AIP Conference Proceedings, **1953** (2018) 050011.
3. S. Sarkar, A. Mondal, N. Giri and R. Ray, Phys. Chem. Chem. Phys., **21** (2019) 260.
4. Elements of X-ray diffraction, B.D. Culity, 1956, New York, Addison-Wesley series in metallurgy and materials, ISSN 0515-3972.
5. G. K. Williamson and W. H. Hall, Acta Metall. **1** (1953) 22.
6. George Wypych, PHOTOPHYSICS, Handbook of Material Weathering (Sixth Edition), 2018, 1-26.
7. F. A. Mir, S. Rehman, K. Asokan, S. H. Khan and G. M. Bhat, J Mater Sci: Mater Electron, **25** (2014) 1258.
8. Y. Sun, M. B. Salamon, K. Garnier and R. S. Averback, Physical Review Letters, **91(16)** (2003) 167206.
9. M. Sasaki, P. E. Jönsson, H. Takayama and H. Mamiya, Physical Review B, **71** (2005) 104405.
10. P. Jönsson, M. F. Hansen, P. Svedlindh and P. Nordblad, Physica B, **284-288** (2000) 1754.

11. D. De, A. Karmakar, M. K. Bhunia, A. Bhaumik, S. Majumdar and S. Giri, J. Appl. Phys., **111** (2012) 033919.

12. S. Dhara, R. Roy Cowdhury and B. Bandyopadhyay, RSC Adv., **5** (2015) 95695.

Chapter 5

5 Uncompensated Grain Boundary Spin Driven Exchange Bias Effect in Granular NiO film

5.1 Introduction

The exchange bias (EB) effect typically appears due to the pinning mechanism at the interface between two magnetic components having significant difference in anisotropy [1]. A combination of ferromagnetic (FM) and antiferromagnetic (AFM) substances is one of the classical example where the Curie temperature of the FM component is higher than that of the Nèel temperature (T_N) corresponding to the AFM component. When the sample is exposed to a static magnetic field at a temperature ($>T_N$) and cooled through T_N down to low temperature ($< T_N$), the FM spins adjacent to AFM spins are coupled to the uncompensated AFM spin. This coupling gives rise to a displacement of the magnetic hysteresis loop, which is the typical manifestation of EB effect. Although EB has been extensively observed in diverse ranges of thin bi-layered [2], multi-layered [3] or core–shell structures [4] constructed by different structural phases [1], this has also been reported in various chemically single phase compounds composed of coexisting magnetic phases having significant difference in magnetic anisotropies [5–10]. Numerous reports on EB phenomenon in AFM oxide nanoparticles like NiO [8,9], CuO [10,11], γ-Fe_2O_3, Fe_3O_4 [12,13], Cr_2O_3 [9,14] and Co_3O_4 [15] are

found in recent years. These establish the evidence of distinguishable surface magnetic anisotropy from that of core. The nature of surface magnetic anisotropy is proposed to be different in different cases. For example, for NiO [8] and γ - Fe_2O_3 [12], a frustrated magnetic shell has been suggested whereas, a spin glass component has been suggested in the shell of γ -Fe_2O_3 [16] and Fe_3O_4 [17] nanoparticles. Presence of a weak ferromagnetic (FM) component has been suggested at the surface of AFM CuO nanoparticles [11]. Recently, a disordered glassy magnetic phase at the particle surface has been proposed in $La_{1/3}Sr_{2/3}FeO_3$ [18]. The magnetic phase separation between glassy magnetic and antiferromagnetic components leads to the substantial exchange bias effect at low temperature as confirmed by meticulous polarized neutron diffraction studies. Exchange bias in single layer film is rather rarely observed [19] compared to that observed in bi-layer films [1], phase separated bulk materials or nanoparticles [5]. In this paper, we report significant exchange bias effect in granular NiO film, which is a rare example as found in literature. Here, exchange bias effect is suggested due to pinning mechanism involving dissimilar anisotropies of a new magnetic phase at the surface consisting of uncompensated spins and AFM core. Appearance of considerable exchange bias effect in a granular antiferromagnetic film is significant for the applications.

5.2 Experimental Details

Nickel nitrate (0.04 M) has been taken as Ni^{2+} source which is homogenized with dehydrated alcohol [20]. This active solution is then thoroughly mixed with Polyethylene glycol (PEG) in a ratio of 1ml–70 mg. The homogeneous solution is used for the chemical deposition on a Si wafer substrate by the dip-coating technique. Each layer of deposition is dried at 100 °C for 20 min. It is then calcinied at 500 °C in air for 20 min. Decomposition of PEG occurs during the heating steps of calcination. Finally, calcination at 500 °C completely removes the organic residues to form NiO film. In order to prepare thick NiO film, whole procedure starting from dip – coating of the Si wafer into the homogeneous mixture of the solution and subsequent calcination have been repeated for 25 times.

The X-ray diffraction pattern of the film recorded in the X-ray diffractometer with Cu-K_α radiation confirms single polycrystalline phase of NiO film. The surface topology of NiO film is probed by an atomic force microscopy, Veeco-diCP II. Magnetization is measured in a commercial magnetometer of Quantum Design (MPMS, XL).

5.3 Results and Discussions

X-ray diffraction pattern of a polycrystalline NiO film is shown in **Figure 5.1.** Peaks corresponding to (111) and (200) planes of fcc structured NiO with space

group Fm3m are associated with the peak corresponding to Si wafer as assigned in the **Figure 5.1**. The surface topology of NiO film is probed by the atomic force microscopy. Two and three dimensional images are shown in **Figure 5.2(a)** and **Figure 5.2(b)**, respectively. **Figure 5.2(a)** exhibits the morphology of the grains of NiO particles having a distribution of size in the range 15–25 nm. **Figure 5.2(b)** reveals the surface roughness of the film ~6 nm. We further note that the NiO film is granular in nature, which is different from the film, as synthesized from the pulsed laser deposition [21] and sputtering techniques [22].

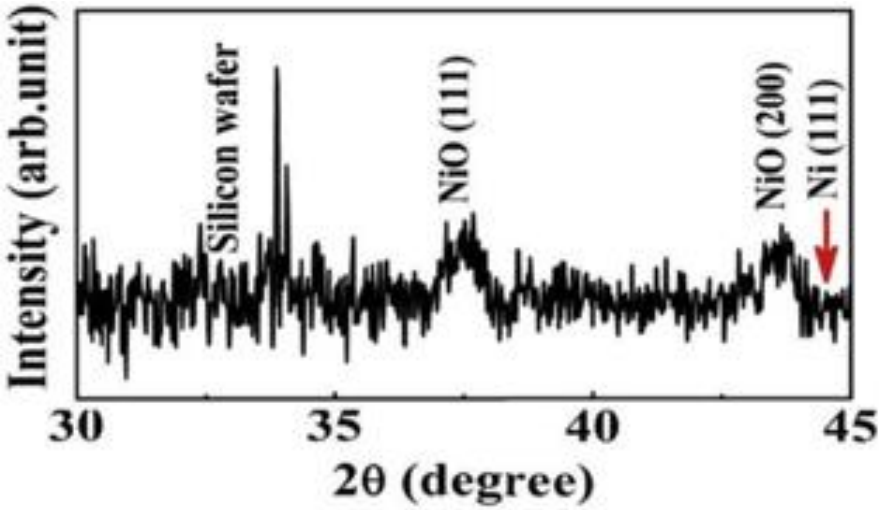

Figure 5.1: XRD patterns of NiO film and Si wafer at 300 K. Downward arrow represents the absence of XRD line corresponding to Ni (111) plane.

The temperature variations of magnetization measured in the heating cycle with 500 Oe both in zero field cooled (ZFC) and field cooled (FC) modes are shown in **Figure 5.3**. In case of ZFC mode, samples are cooled down to 6 K from 300 K in zero-field and measurements are carried out in the heating cycle. In case of FC mode, samples are cooled in 500 Oe and measurements are carried out in the

heating cycle, like the ZFC magnetization measurements. The FC magnetization deviated from ZFC magnetization around 250 K, as depicted in the **Figure 5.3** by an arrow. A broad peak appears in the thermal variation of ZFC magnetization around 156 K (T_P) as evident in **Figure 5.3**.

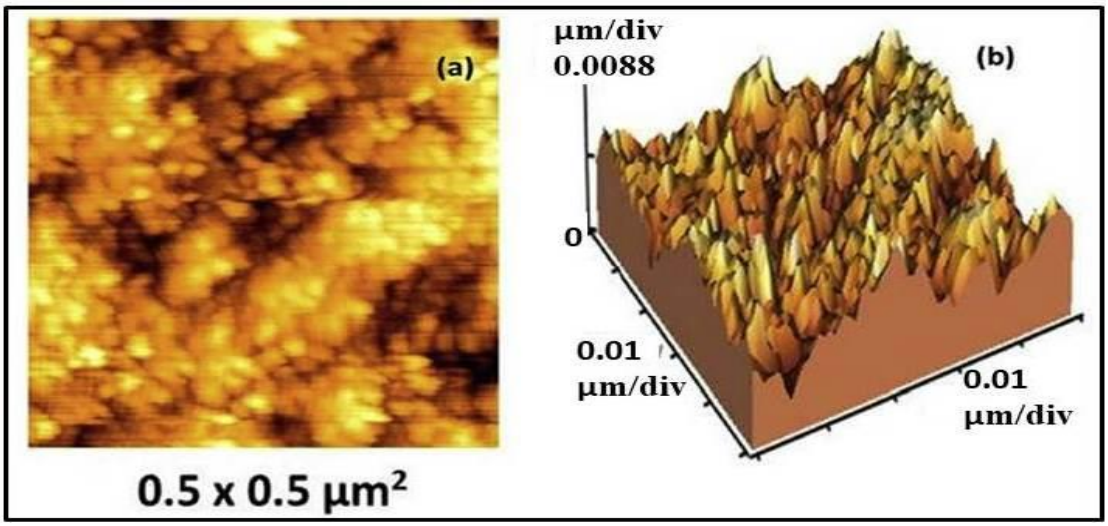

Figure 5.2: (a) Two-dimensional image and (b) three-dimensional image of NiO film, using atomic force microscopy.

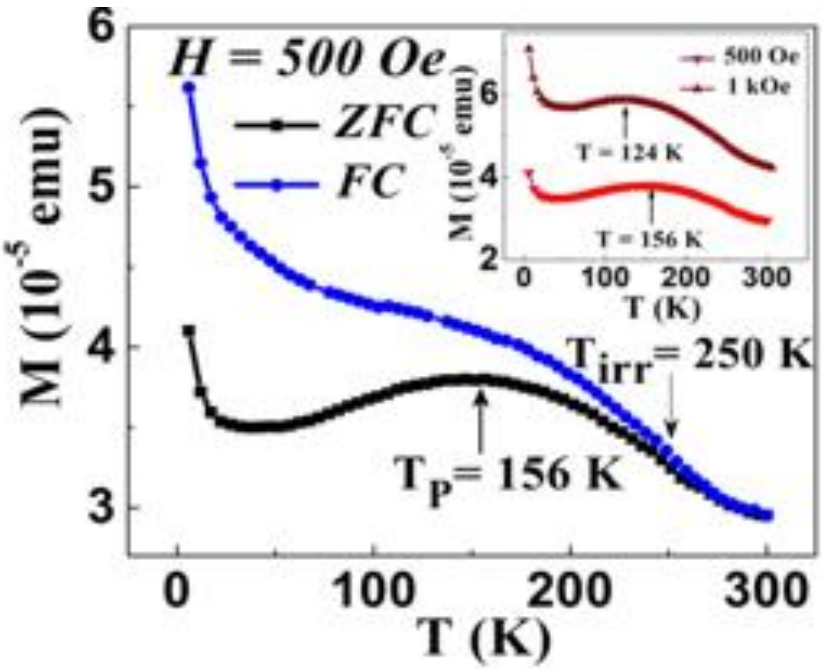

Figure 5.3: Thermal variation of ZFC and FC magnetization for NiO film measured at 500 Oe. Inset highlights ZFC magnetization measured in 500 Oe and 1 kOe.

This ZFC peaks may be interpreted as the spin-glass freezing temperature [23] or the blocking temperature [24]. To reveal the origin of the ZFC peak further, the temperature dependence of the ZFC magnetization is measured at two applied magnetic fields (H=500 Oe and 1 kOe) as shown in **Figure 5.3 inset**. The peak at T_P is found to shift toward low temperature for higher magnetic field which is a signature of a disordered magnetic system [25]. This has also been observed for the spin glass systems [26]. Magnetic memory in ZFC mode is an ascertaining phenomenon of the spin glass phase. A system exhibiting the memory effects in thermal variation of ZFC magnetization must also exhibit the same in FC magnetization. Therefore, we have performed first the experiment on memory effect in thermal variation of FC magnetization. We have followed the experimental protocol as also done by Biswas et al., [27] which is proposed by Sun et al., [28]. From 300 K ($> T_P$) the sample is cooled down to 6 K at the rate 2 K/min under 500 Oe and magnetization is recorded during the cooling process. This cooling process is associated with a halt at T_{halt}=103 K and 25 K for 2 hrs each. Magnetic field is cut off during this waiting time and magnetization is allowed to relax. After completion of each 2 hrs, the magnetic field is reapplied to 500 Oe and measurement is resumed while cooling down to 6 K. This curve defined by FC cooling (FCC) is shown in **Figure 5.5**. Then the temperature is raised up continuously in the same rate (2 K/min) from 6 K and magnetization is recorded in the same field as shown by FC heating (FCH) curve. FCC curve

shows steps at T_{halt} as expected. The FCH curve does not show any wriggle at T_{halt} although it is much below T_P. Absence of any wriggle at the halt temperature in FCH curve indicates the absence of memory effect even in thermal variation of FC magnetization. This suggests the superparamagnetic blocked state. Usually, the memory experiment is done in low field. Here, the experiment is performed in a comparatively higher field for obtaining reliable magnetization data because of the low moment of the film. It may hinder the possible characterization of spin glass state, which has been reported in some cases [29].

The FC magnetization slowly increases with the decrease in temperature down to 25 K. Below ~25 K, both FC and ZFC magnetization increase significantly with decrease in temperature down to 6 K. This sharp increase of both ZFC and FC magnetization indicates the signature of a dominant ferromagnetic (FM) component in the low temperature region.

This FM component may be attributed to the uncompensated (UC) spins at the surface of NiO grains as discussed in the recent reviews [30, 31]. Here, observation of granular NiO film is significant, because the granular NiO film may be considered as an assembly of the NiO nanoparticles. Thus the observed magnetization results in the current investigation are analogous to that reported NiO nanoparticles exhibiting EB effect, where EB effect was proposed due to pinning mechanism at the interface between antiferromagnetic core and an outer shell structure composed of uncompensated spins [24, 32].

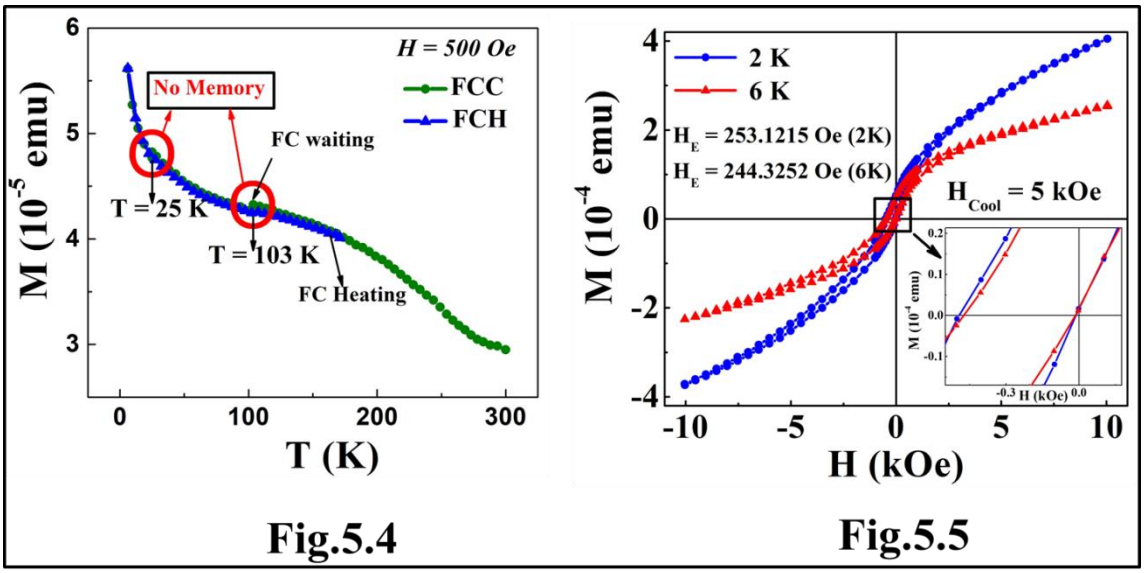

Fig.5.4 Fig.5.5

Figure 5.5: Thermal variation of field cooled (FCC) magnetization measured in the cooling cycle under H_{cool}=500 Oe with two intermediate halts, one at 103 K and other at 25 K for 2 h each. Absence of wriggle at T_{halt} is demonstrated by circles in the magnetization curve measured in heating cycle (FCH).

Figure 5.4: Magnetic hysteresis loops measured at 2 K and 6 K for NiO film after cooling the sample in H_{cool}=5 kOe. Inset highlights the central part of M−H loop.

But the antiferromagnetic ordering temperature is not manifested in the M-T curve, which would be evident in case of low field magnetization measurement. Here, low field measurement could not be performed because of the low moment of the film. However since the EB effect is observed due to field-cooling from 300 K, the AFM order may be lower than 300 K. Though the bulk NiO is known to order anti-ferromagnetically around 523 K, the transition temperature decreases drastically with reduction of particle size [24]. In fact coexistence of antiferromagnetic order followed by a superparamagnetic blocking temperature has been suggested in literature [24, 33] for NiO.

Appearance of UC-spins typically may bring in a new anisotropy which is different from the core anisotropy. Coexistence of different magnetic anisotropies

may lead to the EB effect due to field cooling. To investigate it, sample is cooled from 300 K down to low temperatures in 5 kOe (H_{cool}). Magnetic hysteresis (M−H) loops are measured in between ± 10 kOe.

The M−H loops at representative temperatures of 2 and 6 K are shown in **Figure 5.4**. The figure depicts a significant shift of the M−H loops along negative H−axis. The shift along field-axis is defined as exchange bias field (H_E) [5]. We have calculated coercive field (H_c) and H_E as $\boldsymbol{H_c = \frac{1}{2}(H_c^+ - H_c^-)}$ and $\boldsymbol{H_E = \frac{1}{2}(H_c^+ + H_c^-)}$, respectively, where H_c^+ (H_c^-) represents positive (negative) coercive field. Thermal variation of H_E and H_c are shown in **Figure 5.6(a)**. H_E decreases monotonically with increase in temperature and vanishes around 156 K (T_p). Decrease of H_E is associated with the decrease of H_c, as depicted in the **Figure 5.6(a)**. Reported results on NiO nanoparticles revealed that its coercive field (H_c) is significant which have been attributed to the surface anisotropy [29,34]. In the current investigation, observed EB field is suggested due to pinning mechanism at the interface between antiferromagnetic NiO core and FM surface component consisting of UC-spins. Appearance of UC-spins in the antiferromagnetic fine particle system has commonly been assigned at the crystallite surfaces [30]. Since crystallites in the particles are physically in close contact, the pinning mechanism takes place at the crystallite interfaces [9, 35]. However, occurrence of FM component due to the presence of minor phase (≤5%) of Ni cannot be ruled out

as it is beyond the detectability of X-ray diffraction studies as evident from **Figure 5.1.**

The cooling field dependence of H_E has been observed in various systems [36]. Here, cooling field (H_{cool}) dependence of H_E measured at 6 K is displayed in **Figure 5.6(b)**. Sample is cooled down to 6 K from 300 K under different cooling field (H_{cool}) and H_E is estimated as discussed earlier. A sharp rise of H_E is observed with increasing H_{cool} up to 5 kOe, above which it increases slowly indicating a saturating trend for H_{cool}=20 kOe. During field cooling process a new layer consisting of pinned spins may appear at the interface of core and surface spins. This pinned layer typically gives rise to the EB effect. Small cooling field (H_{cool}) is not strong enough to align the pinned spins.

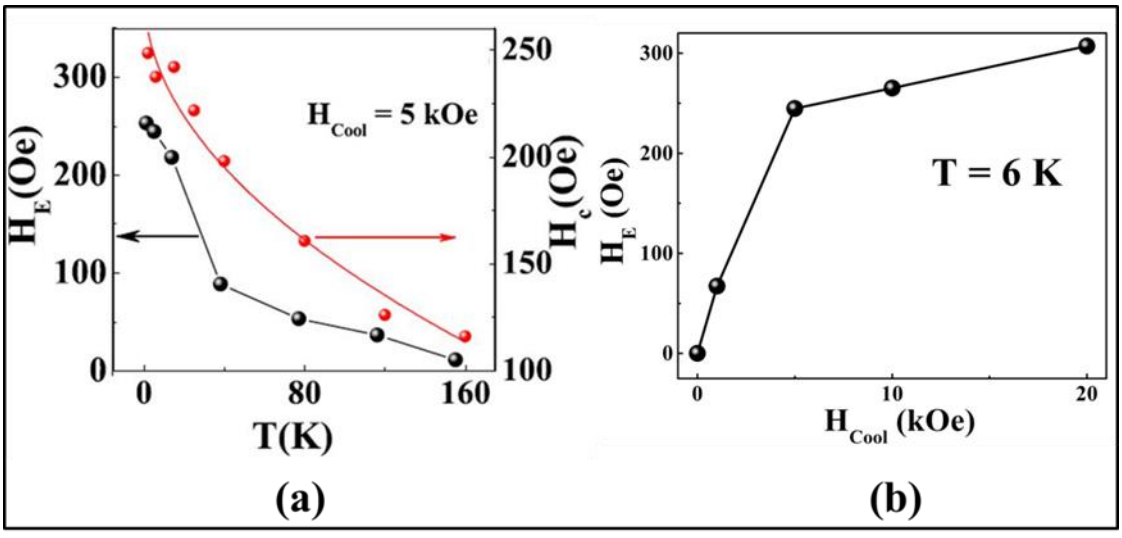

Figure 5.6: (a) Thermal variation of exchange bias field (H_E) and coercivity (H_c) of NiO film. (b) Cooling field (H_{cool}) dependence of H_E measured at 6K for NiO film.

The progressive alignment of the pinned spins along H_{cool} direction is increased rapidly with increasing H_{cool} till 5 kOe. Beyond 5 kOe the process becomes slow

exhibiting saturating tendency of H_E. This saturating trend indicates absence of minor loops effect [37].

Training effect describes the decrease of shift of M−H loop when the system is successively field-cycled at a particular temperature after the field cooling process [38]. **Figure 5.7(a)** represents a central portion of the M−H loops highlighting the decrease of shift with number (λ) of field cycling. The plot of H_E with λ is shown in **Figure 5.7(b)**. Here, successive M−H loops up to seven times (λ=7) are recorded in between ±10 kOe after cooling the sample down to 6 K from 300 K in H_{cool}=10 kOe. Decrease of H_E with λ is fitted satisfactorily with the empirical relation, $\boldsymbol{H_E(\lambda) - H_E^{\infty} \propto 1/\sqrt{\lambda}}$, where H_E^{∞} corresponds to $H_E(\lambda)$ at $\lambda \to \infty$.

The solid curve in **Figure 5.7(b)** demonstrates the best fit of H_E variation for λ≥2 with $H_E^{\infty} \sim$ 190 Oe. The above empirical equation does not explain the sharp fall (∼15%) of H_E in second loop compared to first loop as also observed in NiO nanoparticles [9]. More generalized explanation of the training effect has been proposed by Binek [39]. A recursive formula in the framework of spin configurational relaxation is proposed which describes the decrease H_E in the (λ + 1)th loop compared to λth loop as

$$\boldsymbol{H_E(\lambda+1) - H_E(\lambda) = -\gamma[H_E(\lambda) - H_E^{\infty}]^3} \quad \textbf{.....(5.1)}$$

Where, γ is a sample dependent constant and H_E^{∞} is the value of H_E at $\lambda \to \infty$. Using this recursion relation the whole set of data could be generated for H_E at

different λ. The calculated values are shown by the filled symbols in **Figure 5.7(b)** which matches satisfactorily with the experimental data (open symbols). The best fit corresponds to $\gamma = 7.5\times10^{-5}$ Oe^{-2} and H_E^{∞} = 168.2 Oe.

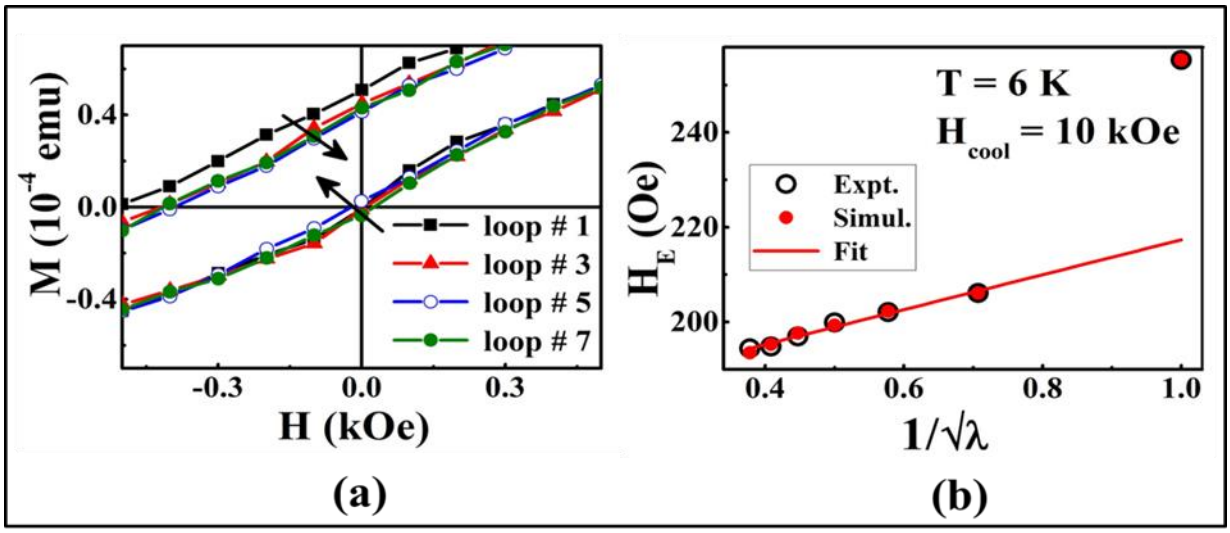

Figure 5.7: (a) Central portion of the M−H loop highlighting the decrease of shifts along the field axis with the successive field-cycling measured at 6 K after cooling the sample at 10 kOe. (b) Decrease of exchange bias field (HE) with the successive field cycling loop index number λ. Continuous line represents the fit using empirical equation as discussed in the text. Filled circles are calculated values using Eq.5.1.

5.4 Conclusions

Surface topology of the granular NiO film fabricated on a cleaned Si wafer by the sol-gel dip coating technique is probed by the atomic force microscopy. It displays grain sizes in the range 15–25 nm. The surface topology of NiO film depicts roughness ~6.0 nm. Furthermore, existence of granular NiO film is confirmed by the AFM image. Thermal variation of magnetization measured in ZFC mode in 500 Oe depicts a broadened peak around 156 K (=T_p). This may indicate that T_p behaves like a blocking temperature of the weakly interacting

antiferromagnetic nanoparticles or a spin-glass like transition of the interacting antiferromagnetic nanoparticles. Absence of FC memory effect nullifies the possibility of spin glass state. Significant rise in thermal variation of FC and ZFC magnetization below 25 K infer the existence of FM component. Due to field-cooling process a shift in the M−H loop along H-axis is observed. This shift is the manifestation of exchange bias effect. The EB field varies significantly both with temperature as well as cooling field. It vanishes around 156 K (T_p), which is associated with the disappearance of coercivity. Since EB effect involves the pinning mechanism at the interface between two magnetic domains having significant difference in magnetic anisotropy, the vanishing EB effect around T_p indirectly indicates that the difference of magnetic anisotropy weakens above T_p. Cooling field dependence of H_E at 6 K shows saturating trend with the variation of cooling field near 20 kOe. Training effect in accordance with the recursive formula in the framework of spin configurational relaxation model has been observed. Here, the pinning mechanism at the interface between antiferromagnetic core and a weak ferromagnetic shell composed of uncompensated spins in the granular NiO film is suggested, which leads to the exchange bias effect. However, occurrence of FM component due to the presence of minor phase (≤5%) of Ni cannot be ruled out. The observed exchange bias in the granular polycrystalline NiO film is a rare consequence, which attracts the community.

5.5 References

1. J. Nogués, I.K. Schuller, J. Magn. Magn. Mater. 192 (1999) 203–232.
2. X. Yuan, X. Xue, J. Du, F.Z. Huang, Q. Xu, Solid State Commun. 161 (2013) 9–12.
3. S.H. Lim, M. Murakami, S.E. Lofland, A.J. Zambano, L.G. Salamanca-Riba, I. Takeuchi, J. Magn. Magn. Mater. 321 (2009) 1955–1958.
4. H. Al Chaghouri, F. Tuna, P.N. Santhosh, P. John Thomas, Solid State Commun. 230 (2016) 11–15.
5. S. Giri, M. Patra, S. Majumdar, J. Phys.: Condens. Mater. 23 (2011) 073201–073223.
6. J. Nogués, J. Sort, V. Langlais, V. Skumryev, S. Surinach, J.S. Munoz, M.D. Baro, Phys. Rep. 422 (2005) 65–117.
7. Ó. Iglesias, A. Labarta, X. Batlle, J. Nanosci. Nanotechnol. 8 (2008) 2761–2780.
8. S.A. Makhlouf, H. Al-Attar, R.H. Kodama, Solid State Commun. 145 (2008) 1–4.
9. Sk Sabyasachi, S. Majumdar, S. Giri, Solid State Commun. 151 (2011) 1515–1519.
10. A. Punnoose, H. Magnone, M.S. Seehra, J. Bonevich, Phys. Rev. B 64 (2001) 174420–174427.

11. D.R. Saha, A.K. Nandi, D. Chakravorty, J. Magn. Magn. Mater. 355 (2014) 184–187.
12. T.N. Shendruk, R.D. Desautels, B.W. Southern, J. Van Lierop, Nanotechnology 18 (2007) 455704–455709.
13. G. Salazar-Alvarez, J. Qin, V. Sepelák, I. Bergmann, M. Vasilakaki, K.N. Trohidou, J.D. Ardisson, W.A.A. Macedo, M. Mikhaylova, M. Muhammed, M.D. Baró, J. Nogués, J. Am. Chem. Soc. 130 (2008) 13234–13239.
14. D. Tobia, E.L. Winkler, R.D. Zysler, M. Granada, H.E. Troiani, J. Alloy. Comp. 495 (2010) 520–523.
15. M.J. Benitez, O. Petracic, E.L. Salabas, F. Radu, H. Tüysüz, F. Schüth, H. Zabel, Phys. Rev. Lett. 101 (2008) 097206–097209.
16. H. Wang, T. Zhu, K. Zhao, W.N. Wang, C.S. Wang, Y.J. Wang, W.S. Zhan, Phys. Rev. B 70 (2004) 092409–092412.
17. B. Martínez, X. Obradors, Ll Balcells, A. Rouanet, C. Monty, Phys. Rev. Lett. 80 (1998) 181–184.
18. Sk Sabyasachi, M. Patra, S. Majumdar, S. Giri, Phys. Rev. B 86 (2012) 104416–104424.
19. Y. Yamamoto, H. Nakagawa, H. Hori, J. Magn. Magn. Mater. 310 (2007) 2384–2386.
20. S. Das, S. Majumdar, S. Giri, J. Phys. Chem. C 114 (2010) 6671–6675.

21. P. Misra, V.K. Sahu, R.S. Ajimsha, A.K. Das, B. Singh, J. Phys. D Appl. Phys. 50 (2017) 415106.
22. B. Subramanian, M. Mohamed Ibrahim, V. Senthilkumar, K.R. Murali, V.S. Vidhya, C. Sanjeeviraja, M. Jayachandran, Physica B 403 (2008) 4104–4110.
23. S.D. Tiwari, K.P. Rajeev, Physical Rev.B 72 (2005) 104433.
24. M. Tadic, D. Nikolic, M. Panjan, G.R. Blake, J. Alloy. Comp. 647 (2015) 1061– 1068.
25. J.R.L. de Almeida, D.J. Thouless, Phys. Reu. Lett. 32 (1974) 1792.
26. H. Bouchiat, J. Phys. C Solid State Phys. 16 (1983) L145.
27. Sumita Biswas, Sk Sabyasachi, Asim Bhaumik, Ruma Ray, IEEE Trans. Magn. 50 (2014) 2301107.
28. Young Sun, M.B. Salamon, K. Garnier, R.S. Averback, Phys. Rev. Lett. 91 (2003) 167206.
29. E. Winkler, R.D. Zysler, M. Vasquez Mansilla, D. Fiorani, D. Rinaldi, M. Vasilakaki, K.N. Trohidou, Nanotechnology 19 (2008) 185702–185709.
30. R.H. Kodama, A.E. Berkowitz, D. Fiorani (Ed.), Surface Effects in Magnetic Nanoparticles, Springer, New York, 2005, pp. 189–216.
31. S. Morup, D.E. Madsen, C. Frandsen, C.R.H. Bah, M.F. Hansen, J. Phys. Condens. Matter 19 (2007) 213202–213232.

32. M. Thakur, M. Patra, S. Majumdar, S. Giri, J. Alloys Compounds 480 (2) (2009) 193–197.

33. M. Feygenson, A. Kou, L.E. Kreno, A.L. Tiano, J.M. Patete, F. Zhang, M.S. Kim, V. Solovyov, S.S. Wong, M.C. Aronson, Phys. Rev. B 81 (2010) 014420.

34. R.H. Kodama, S.A. Makhlouf, A.E. Berkowitz, Phys. Rev. Lett. 79 (1997) 1393–1396.

35. J. Nogués, V. Skumryev, J. Sort, S. Stoyanov, D. Givord, Phys. Rev. Lett. 97 (2006) 157203–157206.

36. A. Rostamnejadi, M. Venkatesan, P. Kameli, H. Salamati, J.M.D. Coey, J. Appl. Phys. 116 (2014) 043913–043916.

37. D. De, Ò. Iglesias, S. Majumdar, S. Giri, Phys. Rev. B 94 (2016) 184410–184419.

38. P.Y. Yang, C. Song, F. Zeng, F. Pan, Appl. Phys. Lett. 92 (2008) 243113–243115.

39. Ch Binek, Phys. Rev. B 70 (2004) 014421–014425.

Chapter 6

6 Doping Induced Tailoring of Exchange Bias Effect in Granular $Ni_{1-x}Zn_xO$ Film

6.1 Introduction

The pinning mechanism at the interface of two magnetic components having significantly different anisotropy [1, 2] gives rise to the exchange bias effect (EB). At the beginning, EB effect was observed in a system composed of ferromagnetic (FM) and antiferromagnetic (AFM) components where the curie temperature of FM component (T_C) is higher than that of Néel temperature of AFM component (T_N). Initially, the sample is exposed to a static magnetic field at a temperature ($T_N < T < T_C$). As it is cooled down to a temperature ($< T_N$), the coupling between FM spins and nearby AFM spins causes a displacement of magnetic hysteresis loop [3], which is the typical evidence of EB effect. The EB effects have been observed in numerous morphologies such as thin layer structures like thin bi-layered [4], multi-layered [5], core-shell structure [6], AFM oxide nanoparticles like NiO [7], Fe_3O_4 [8], Cr_2O_3 [9] and $rGO@Co_3O_4$ [10], thin films like Co–CoO [11]. Exchange bias present in single layer film [12] is rarely found in literature compared to that observed in other structures. The exchange bias effect is widely used in different magnetic sensors, computer memory technology, read heads for spintronic applications [13]. In this paper, we report significant

exchange bias effect in granular $Ni_{1-x}Zn_xO$ film. Pinning mechanism of a new magnetic phase having different anisotropies at the surface consisted with uncompensated spins and AFM core leads to the exchange bias effect. An exchange bias effect present in the granular antiferromagnetic film has great importance in application like magneto-resistive sensors [14], spin valve devices [15], etc.

6.2 Experimental Details

$Ni_{1-x}Zn_xO$ film is fabricated on Si (100) substrate by the sol-gel dip coating technique. Si (100) substrate is dipped in a solution composed of Ni^{2+} and Zn^{2+} source. 0.06M nickel nitrate and zinc nitrate are homogenized with dehydrated alcohol [16]. Polyethylene glycol is then added to the solution. Solution is stirred for 1 h on magnetic stirrer and finally it is used for the chemical deposition. Si substrate is cleaned with dilute HCl, alcohol and deionized water by sonicating for 1 h. Finally, it is dried at 120 °C for 15 min. After each layer deposition, the prepared substrate is dried at 120 °C for 20 min. This process of deposition and subsequent heat treatments are done consecutively up to 25 times. Finally, it is annealed at 450 °C for 3 h in air. Samples are prepared for different doping concentration x=0.03 and x=0.05. The X-ray diffraction pattern of the film was measured by X-ray diffractometer with Cu-K_α radiation. The surface topology is characterised by AFM. Magnetization is

measured in a commercial SQUID magnetometer (Quantum Design, MPMS-5).

6.3 Results and Discussions

The X-ray diffraction pattern of $Ni_{0.95}Zn_{0.05}O$ film is shown in **Figure 6.1**. XRD peaks of $Ni_{1-x}Zn_xO$ are assigned to (111), (200), (220), (311) and (222) planes of *fcc* structured NiO with space group *Fm3m* following JCPDS (Card no: 040835). This assures the single phase *fcc* structured $Ni_{1-x}Zn_xO$. The average crystalline size of the $Ni_{1-x}Zn_xO$ particles estimated from the broadening of the diffraction peaks by using Williamson and Hall's modified Scherrer's formula [$\beta \cos\theta = 0.89\lambda/D + 2\varepsilon \sin\theta$, where ε is microstrain] are ~ 16 nm and 9 nm for x=0.03 and 0.05, respectively.

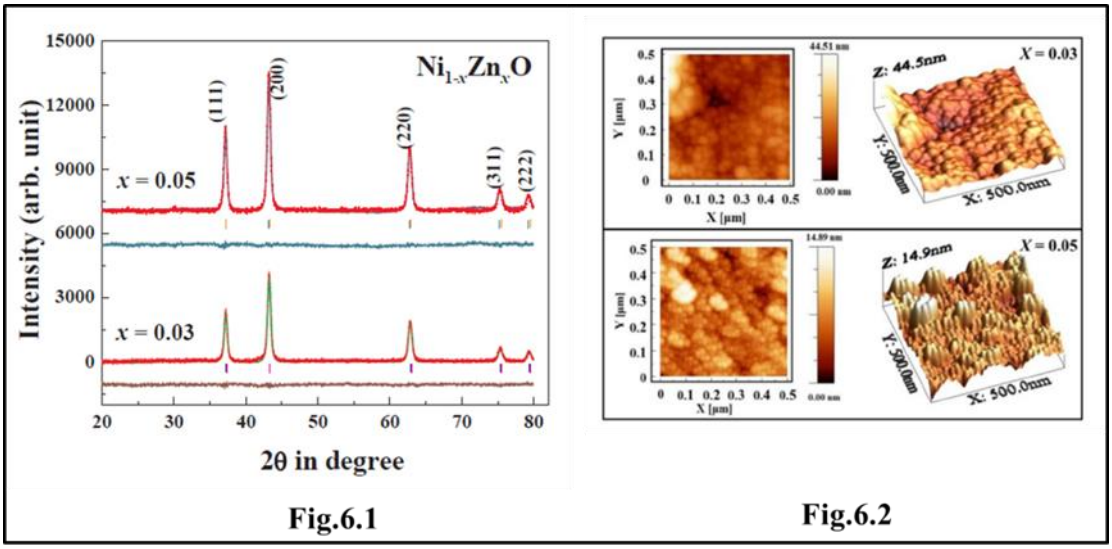

Figure 6.1: XRD patterns of Ni $_{1-x}$Zn $_x$O (x=0.03, 0.05) film at 300 K.

Figure 6.2: Two and three - dimensional AFM images of $Ni_{0.97}Zn_{0.03}O$ and $Ni_{0.95}Zn_{0.05}O$ film.

The lattice parameters are calculated as 4.1803 Å and 4.1840 Å for x=0.03 and 0.05, respectively, using Rietveld analysis. The unit cell volumes are estimated as 73.0498 $Å^3$, 73.2445 $Å^3$ and the bond length of Ni^{2+}-O^{2-} are assessed as 2.0920 Å, 2.6202 Å for x=0.03 and 0.05, respectively, using VESTA software. These results infer that the lattice parameter as well as unit cell volume increases with x. The surface topology of $Ni_{1-x}Zn_xO$ films were probed by the atomic force microscopy. Two and three dimensional images of $Ni_{1-x}Zn_xO$ film for x=0.03 and x=0.05 are shown in **Figure 6.2**. Crystallite sizes are found to be in accordance with that obtained from the XRD results. We further note that nature of the $Ni_{1-x}Zn_xO$ film is granular in nature, which is different from the film prepared from the pulsed laser deposition [17] and sputtering techniques [18].

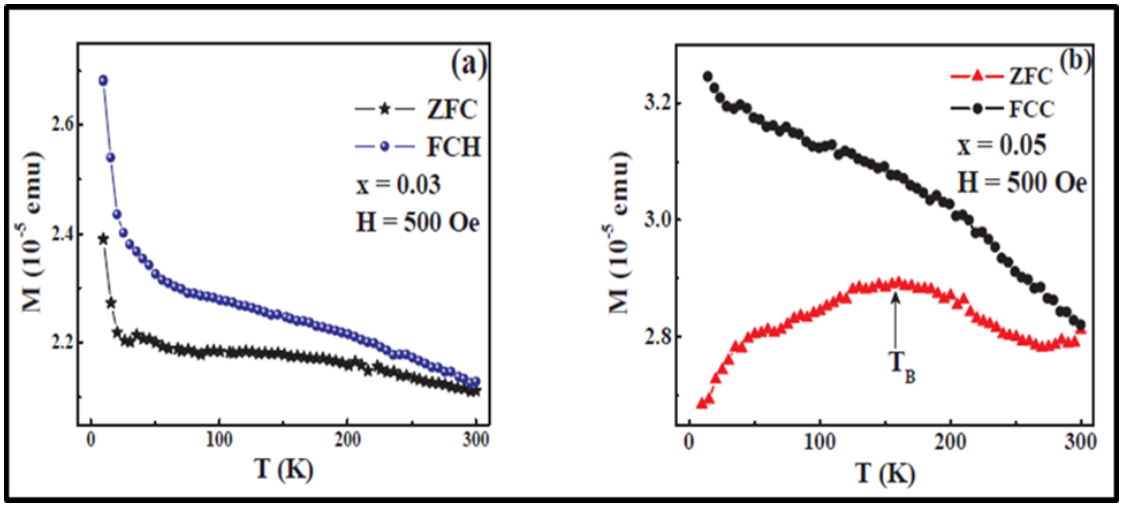

Figure 6.3: Thermal variation of ZFC and FC magnetization for (a) $Ni_{0.97}Zn_{0.03}O$ and (b) $Ni_{0.95}Zn_{0.05}O$ film, respectively measured at 500 Oe.

The temperature variations of magnetization measured in zero field cooled (ZFC) and field cooled (FC) mode are shown in **Figure 6.3(a)** and **Figure 6.3(b)** for

$Ni_{0.97}Zn_{0.03}O$ and $Ni_{0.95}Zn_{0.05}O$ film, respectively. In case of ZFC mode samples are cooled down to 6 K from 300 K in zero-field and magnetization measurements are carried out in the heating cycle with 500 Oe measuring field. In case of FC mode samples are cooled down to 6 K in presence of 500 Oe magnetic field and measurement protocol is same as earlier. For $Ni_{0.97}Zn_{0.03}O$ film both the FC and ZFC magnetization slowly increase with the decrease in temperature down to 30 K and beyond that magnetization increases significantly. This sharp increase of both ZFC and FC magnetization indicates the signature of a dominant ferromagnetic (FM) component in the low temperature region which may be attributed to the uncompensated (UC) spins at the surface of $Ni_{0.97}Zn_{0.03}O$ grains [19, 20]. In contrast, compound with x=0.05 shows absence of such FM component. A broad peak appears in the thermal variation of ZFC magnetization of $Ni_{0.95}Zn_{0.05}O$ film around 155 K indicating a blocking temperature (T_B) as shown in **Figure 6.3(b)**. The FC curve exhibits an increasing trend below 155 K, which also supports the blocked state. Presence of UC-spins at the surface of the granular $Ni_{0.97}Zn_{0.03}O$ typically may bring in a new anisotropy which is different from the core anisotropy. Coexistence of different magnetic anisotropies may lead to the EB effect. To investigate it, sample is cooled from 300 K down to 4 K under different cooling field (H_{cool}) e.g., 2 kOe and 5 kOe. Magnetic hysteresis (M−H) loops [21, 22] measured in between ± 5.0 kOe are shown in **Figure 6.4(a)** and **Figure 6.4(b)**. The figures depict a significant shift of the M−H loops along

negative H−axis. The shift along field axis is defined as exchange bias field (H_E) [2] which are estimated as 55 Oe and 75 Oe for H_{cool} = 2 kOe and 5 kOe, respectively. On the other hand, H_E for $Ni_{0.95}Zn_{0.05}O$ is found to be negligibly small when measured at 4 K under 5 kOe cooling field (See **Figure 6.5**). Thus, H_E strongly depends on dopant content *x* as well as on the cooling field as expected. In spite of having larger particle size, $Ni_{0.97}Zn_{0.03}O$ granular film exhibits significant EB effect, whereas, $Ni_{0.95}Zn_{0.05}O$ does not even though it has more interface area because of smaller crystallite size. This infers that here, the EB

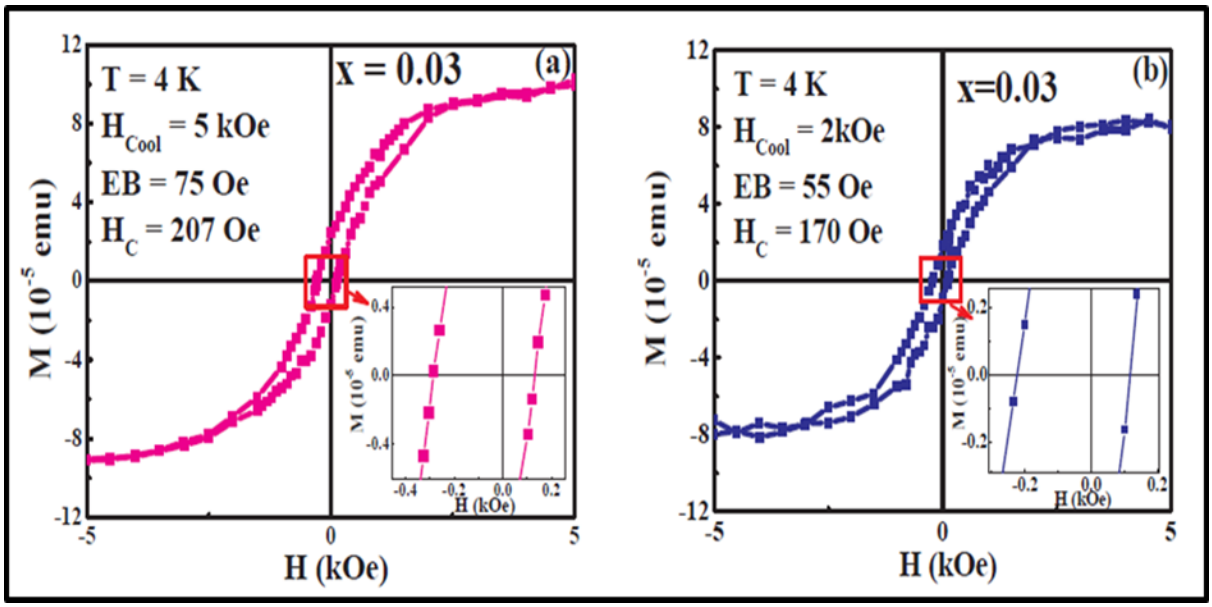

Figure 6.4: Magnetic hysteresis loops for $Ni_{0.97}Zn_{0.03}O$ film measured at 4 K after cooling the sample under (a) H_{cool}=5 kOe and (b) H_{cool}=2 kOe, respectively. Insets highlight the shift of central part of M−H loop along –ve field.

effect is strongly influenced by the dopant content *x* rather than the particle size. In order to understand the occurrence of EB effect the pinning mechanism at the interface between the surface and core anisotropies of granular $Ni_{0.97}Zn_{0.03}O$ film

is suggested. As NiO is antiferromagnetic [7], antiferromagnetic core and UC spin of surface cause significant difference in anisotropy leading to the EB effect.

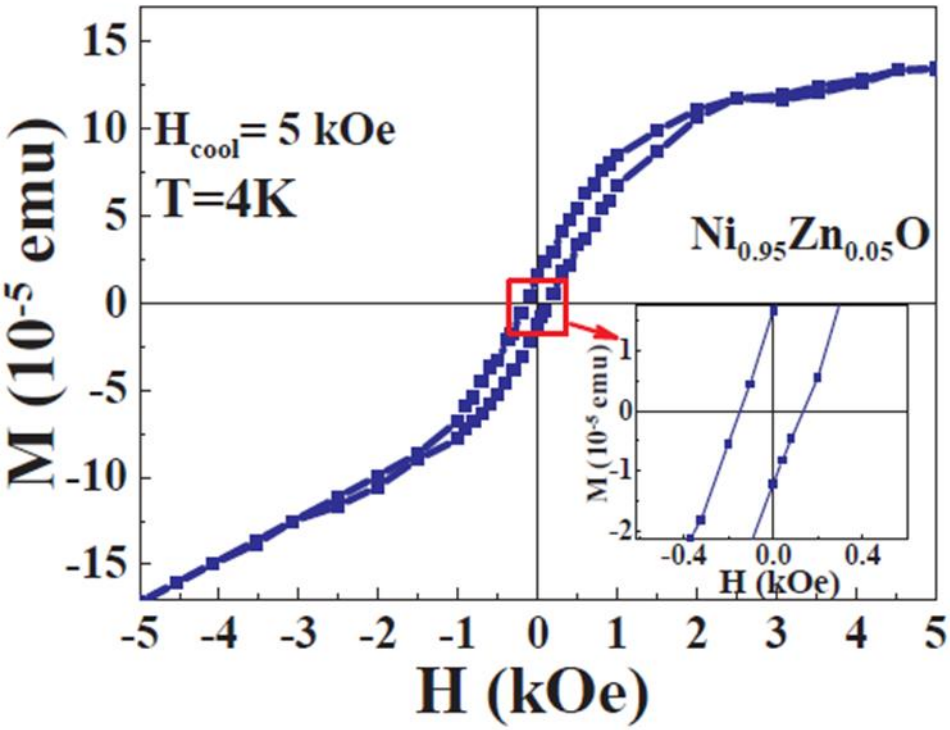

Figure 6.5: Magnetic hysteresis loops for $Ni_{0.95}Zn_{0.05}O$ film measured at 4 K after cooling the sample under H_{cool}=5 kOe. Inset indicates the disappearance of exchange bias effect.

6.4 Conclusions

$Ni_{1-x}Zn_xO$ film was fabricated on a clean Si (100) single crystal by the sol-gel dip coating technique. Average size of the crystallites obtained from X-ray diffraction is 16 nm and 9 nm for x=0.03 and 0.05, respectively. Thermal variation of FC and ZFC magnetization reveal the presence of uncompensated spins for $Ni_{0.97}Zn_{0.03}O$. The UC spin component may bring in a new anisotropy which is different from the core anisotropy. Coexistence of different magnetic

anisotropies may lead to the EB effect. This EB field is found to depend strongly on the dopant (Zn) concentration *x* but not on the crystallite size. The formation of the granular film is the key where the granules can be realized as an assembly of nanoparticles of 16 nm average crystallite size for *x*=0.03. The pinning mechanism at the interface between antiferromagnetic core and shell consisting of uncompensated spins which may lead to the EB effect in the granular $Ni_{1-x}Zn_xO$ film is proposed.

6.5 References

1. J. Nogués, I. K. Schuller, J. Magn. Magn. Mater. 192 (1999) 203.
2. S. Giri, M. Patra, S. Majumdar, J. Phys. Condens. Matter 23 (2011) 073201.
3. A. Mondal, S. Sarkar, N. Giri, S. Chatterjee, R. Ray, Acta Metall. Sin. 30 (6) (2017) 521.
4. R. Jungblut, R. Coehoorn, M.T. Johnson, J. aan de Stegge, A. Reinders, J. Appl. Phys. 75 (1994) 6659.
5. S.-H. Lim, M. Murakami, S.E. Lofland, A.J. Zambano, L.G. Salamanca-Riba, I. Takeuchi, J. Magn. Magn. Mater. 321 (2009) 1955.
6. Hanan Al Chaghouri, F. Tuna, P.N. Santhosh, P. John Thomas, Solid State Commun. 230 (2016) 11.
7. Sk Sabyasachi, S. Majumdar, S. Giri, Solid State Commun. 151 (2011) 1515.

8. G. Salazar-Alvarez, J. Qin, V. Šepelák, I. Bergmann, M. Vasilakaki, K.N. Trohidou, J.D. Ardisson, W.A.A. Macedo, M. Mikhaylova, M. Muhammed, M.D. Baró, J. Nogués, J. Am. Chem. Soc. 130 (2008) 13234.
9. D. Tobia, E.L. Winkler, R.D. Zysler, M. Granada, H.E. Troiani, J. Alloy. Comp. 495 (2010) 520.
10. S. Sarkar, A. Mondal, N. Giri, R. Ray, Phys. Chem. Chem. Phys. 21 (2019) 260.
11. M. Takahashi, A. Yanai, S. Taguchi, T. Suzuki, Jpn. J. Appl. Phys. 19 (6) (1980) 1093.
12. Y. Yamamoto, H. Nakagawa, H. Hori, J. Magn. Magn. Mater. 310 (2007) 2384.
13. J.C.S. Kools, IEEE Trans. Magn. 32 (4) (1996) 3165.
14. L. Jogschies, D. Klaas, R. Kruppe, J. Rittinger, P. Taptimthong, A. Wienecke, L. Rissing, M.C. Wurz, Sensors 15 (2015) 28665.
15. J. Nogués, J. Sort, V. Langlais, V. Skumryev, S. Suriñach, J.S. Muñoz, M.D. Baro, Phys. Rep. 422 (2005) 65.
16. S. Das, S. Majumdar, S. Giri, J. Phys. Chem. C 114 (2010) 6671.
17. A. Ghosh, K. Dey, Sk Sabyasachi, A. Karmakar, S. Majumdar, S. Giri, Appl. Phys. Lett. 103 (2013) 052412.

18. A. Subramanian, M. Mohamed Ibrahim, V. Senthilkumar, K.R. Murali, V.S. Vidhya, C. Sanjeeviraja, M. Jayachandran, Physica B 403 (2008) 4104.
19. R.H. Kodama, A.E. Berkowitz, D. Fiorani (Ed.), Surface Effects in Magnetic Nanoparticles, Springer, New York, 2005, pp. 189–216.
20. S. Mørup, D.E. Madsen, C. Frandsen, C.R.H. Bahl, M.F. Hansen, J. Phys. Condens. Matter 19 (2007) 213202.
21. S. Idrissi, H. Labrim, S. Ziti, R. Khalladi, N. EL Mekkaoui, I. EL Housni, S. Mtougui, L. Bahmad, J. Electron. Mater., http://doi.org/10.1007/s11664-019-07110-z.
22. S. Idrissi, R. Khalladi, S. Mtougui, S. Ziti, H. Labrim, I. El Housni, N. El Mekkaoui, L. Bahmad, Physica A 523 (2019) 714–722.

7 Doping Induced Dielectric and Transport Properties of $Ni_{1-x}Zn_xO$

7.1 Introduction

Research on semiconductor nanomaterials has grown tremendously owing to their novel optical, electrical and catalytic properties during the past few decades. The size quantization effect and surface state on the nanometer scale [1-4] make them attractive materials for researchers. Several semiconducting metal oxides ZnO, MgO, NiO and TiO_2 have been successfully studied [5-12] for the last few years. Among them, nickel oxide (NiO) is one of the attractive material because of its potential applications in the technical fields such as microelectronics, nano electronics, optoelectronics, electrochemical, solar cells, gas sensors, etc. [13-19]. In addition, NiO is a promising p-type semiconductor [20], because its properties are very useful for various catalytic, smart windows, biosensors, LEDs and chemical sensing applications [10, 16, 21-23]. NiO is also an intriguing material for applications in fuel cells, lithium ion micro batteries, electro chromic coatings, nanowires, nano fibers, and specific alloy and catalyst applications [16, 22, 24-25].

Besides continuing advancements in material engineering, doping is an unambiguously resourceful method to tune its properties towards the desire direction for vivid applications. The type and purity of dopant plays a very crucial

role in the determination of structural and dielectric properties of NiO. The Zn doped NiO nanoparticles were synthesized by chemical precipitation to study the optical and magnetic properties and used as an electrode material for supercapacitor as reported by Sathish Kumar et al., [26]. The optical and magnetic properties of Zn doped NiO nanoparticles and nanocomposites were reported in Refs. [13, 27-29]. The layered structure of Zn doped NiO in film geometry has been investigated focusing on gas sensing properties [30-31]. The exchange bias effect was explored on the Zn doped NiO [32]. It was observed by Gokul et al., [33] that the ac and dc conductivity of NiO nanoparticles depends on temperature as well as particle size. Another report by Karthik et. al., [34] shows the increase in band gap which is the indication of quantum confinement effect arising from the crystallites. The enhancement of activation energy of Mn doped NiO nanoparticles with dopant concentration were reported by S. P. Raja et al., [35]. A number of reports are available on the study of different elements doping in NiO sample [36-43]. However, dielectric and transport properties of Zn doped NiO has rarely been attempted and yet to be explored. The requirement of materials with high dielectric constant in the field of microelectronics is very important for developing of new dielectric materials and therefore, motivate us to study the dielectric properties of Zn doped NiO nanomaterial.

In the present work, the synthesis, structural and morphological characterization of $Ni_{1-x}Zn_xO$ ($0 \leq x \leq 0.05$) nanoparticles are reported. The dopant (Zn) content

dependence of ac conductivity (σ_{ac}), dc conductivity (σ_{dc}) and dielectric properties of $Ni_{1-x}Zn_xO$ ($0 \leq x \leq 0.05$) are investigated in the temperature range $303 \leq T \leq 423$ K.

7.2 Experimental Details

$Ni_{1-x}Zn_xO$ ($0 \leq x \leq 0.05$) samples were prepared using chemical precipitation method [44]. $Ni(CH_3COO)_2.4H_2O$ and $Zn(CH_3COO)_2.2H_2O$ selected as a source of nickel and zinc, respectively, were taken in stoichiometric ratio for different doping content (x). 2 ml aqueous solution of $Zn(CH_3COO)_2.2H_2O$ was added into $Ni(CH_3COO)_2.4H_2O$ in 32 ml of de-ionized water solution with continuous magnetic stirring and heating at 80^0C. A clear green solution of $Ni(CH_3COO)_2.4H_2O$ was appeared as deep green colour after adding aqueous solution of $Zn(CH_3COO)_2.2H_2O$. 2 ml of PEG was added into precursor solution drop wise under continuous stirring followed by addition of 0.5 M aqueous solution of NaOH of 70 ml. A white voluminous precipitate appeared at the bottom and clear green solution at the top of beaker. This precipitation was washed out using de-ionized water and ethanol for several times to remove the impurities like NaOH. Finally, the product was dried and annealed at 550^0C for 5 hrs.

$Ni_{1-x}Zn_xO$ samples were characterized by X-ray diffraction (XRD) using CuK_α radiation with wavelength 1.5406 Å. The morphology and grain size distribution of nanoparticles were studied by Field Emission Scanning Electron Microscope

(FESEM, model: JEOL, JSM-7610F) and Transmission Electron Microscope (TEM). The optical transmission spectra were measured in the wavelength range 200-800 nm using UV-Vis spectrophotometer (Shimadzu, UV 2401PC). For transport properties measurement, $Ni_{1-x}Zn_xO$ powder was pressed into small cylindrical pellet having a diameter of 13 mm and thickness about 1 mm by applying a uniaxial force of 5 tons for ten minutes using a hydraulic press. Then it is sintered at 100°C for 2 hours. This optimum condition of pellet preparation is obtained to achieve the density of $Ni_{1-x}Zn_xO$ close to that of bulk NiO. Extreme care was taken to ensure that the pelletisation of all the samples was done under identical conditions. Silver paint on both sides of pellet was used as electrodes for dielectric measurement.

7.3 Results and Discussions

7.3.1 Structural and Morphological Studies

Structural characterization of Zn doped NiO nanoparticles are done by using XRD. **Figure 7.1(a)** illustrates the diffraction peaks of $Ni_{1-x}Zn_xO$ ($0.0 \leq x \leq 0.05$) which exhibit a single phase rock salt structure following JCPDS file (Card No. 040835, Space Group. Fm3m). We could not detect any impurity phase, although x-ray diffraction cannot detect minor additional phase, which is less than ~1 %. Here, absence of any impurity phase infers the successful incorporation of Zn into the NiO lattice either by replacing a Ni^{2+} ion or by inserting into the Ni^{2+} vacancy

site. The dimension (D) of $Ni_{1-x}Zn_xO$ nanoparticles is estimated by using Scherrer's formula [45] given by

$$\boldsymbol{\beta \cos\theta = \frac{0.89\lambda}{D} + 2\varepsilon \sin\theta} \text{.....(7.1)}$$

Where β is full width half maxima (FWHM), λ is wavelength of CuK_α radiation (1.5406 Å) and ε is micro strain. It is seen that FWHM of the most intense peak increases with increase in doping concentration and found to be 0.48, 0.55 and 0.80 for x = 0.0, 0.03 and 0.05, respectively, as shown in **Figure 7.1(b)**. We further note that the intensity of the peak increases systematically with increase in x. This happens for using larger amount of sample for higher x to enhance the intensity of XRD peak for better analysis. The average particle size of $Ni_{1-x}Zn_xO$ nanoparticles for x = 0.0 and 0.05 are 26 and 22 nm, respectively. The gradual incorporation of Zn^{2+} in the lattice results the decrease in particle size as shown in **Figure 7.1(c)**. The regular shift of the XRD peak position with Zn doping towards lower θ is also depicted in **Figure 7.1(b)**. This result reveals the gradual increase of unit cell volume of $Ni_{1-x}Zn_xO$ with the increase of Zn content as illustrated in **Figure 7.1(d)**. Thus, it supports the substitution of Ni^{2+} having ionic radius 0.55 Å by a comparatively larger ion Zn^{2+} having ionic radius 0.60 Å [46]. Moreover Zn^{2+} may be incorporated into NiO lattice by substituting the Ni^{2+} vacancy site. Thus, incorporation of Zn^{2+} may take part in the process of reduction of oxygen vacancy.

The FESEM images of $Ni_{1-x}Zn_xO$ nanoparticles for x = 0.0 and 0.05 are shown in **Figure 7.2(a)** and **Figure 7.2(b)**, respectively, and corresponding particle size distributions are shown in their inset accordingly. The particle size obtained from FESEM is commensurate with the XRD results of $Ni_{1-x}Zn_xO$ nanoparticles. The TEM images of $Ni_{1-x}Zn_xO$ nanoparticles for x = 0.0, 0.05, as shown in **Figure 7.3(a)** and **Figure 7.3(d)**, infer the size of particles 24 nm and 20 nm, respectively. In addition, **Figure 7.3(b)** and **Figure 7.3(e)** reveals the presence of (111) and (200) diffraction planes of $Ni_{1-x}Zn_xO$ with interplanar spacing 0.24 and 0.20 nm for x = 0.0 and x = 0.05, respectively. **Figure 7.3(c)** and **Figure 7.3(f)** shows the SEAD pattern of $Ni_{1-x}Zn_xO$ nanoparticles for x = 0.0 and 0.05, respectively.

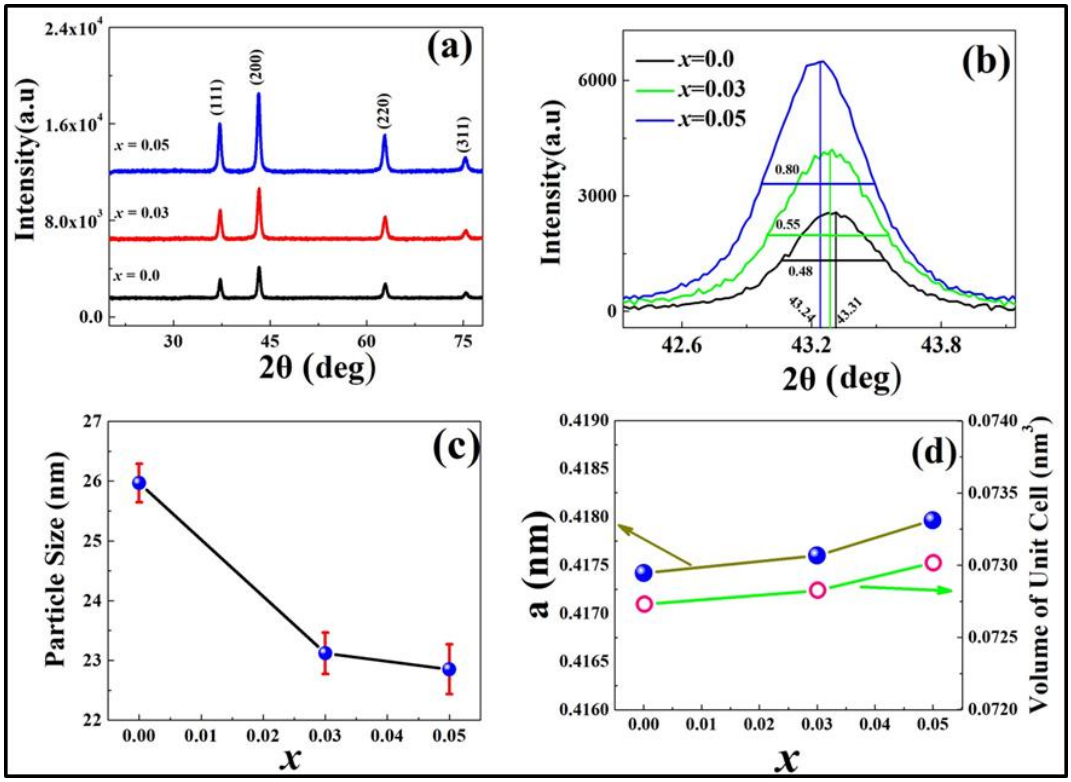

Figure 7.1: (a) X-ray diffraction pattern for $Ni_{1-x}Zn_xO$ with x = 0.0, 0.03 and 0.05. (b) Zoomed view X-ray diffraction pattern of (200) peak for $Ni_{1-x}Zn_xO$ with x = 0.0, 0.03 and 0.05. (c) Particle size variation with x. (d) variation of lattice parameter and volume of unit cell with x.

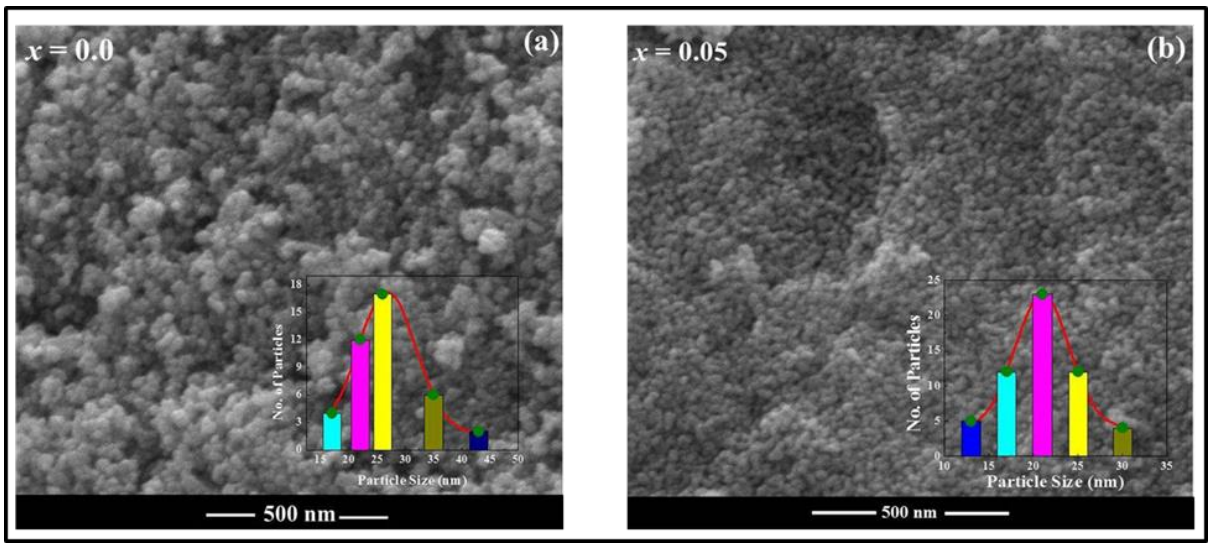

Figure 7.2: FE-SEM image and corresponding particle size distributions of (a) NiO and (b) $Ni_{0.95}Zn_{0.05}O$.

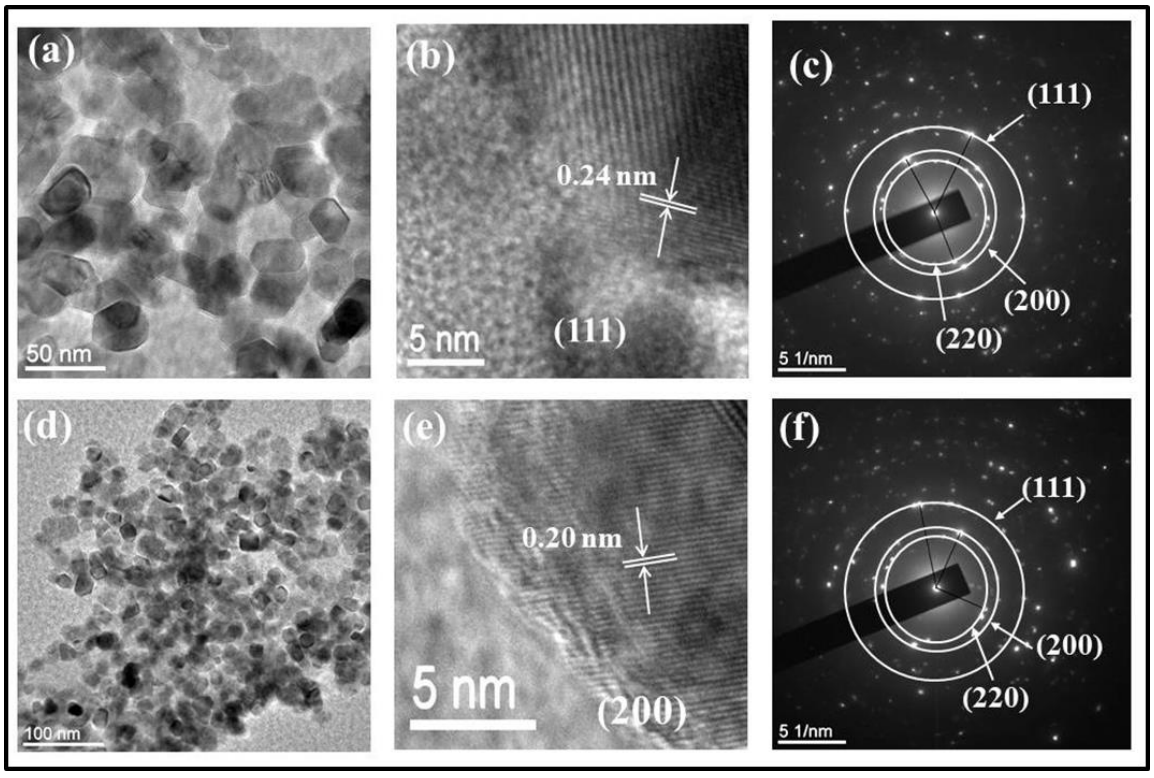

Figure 7.3: TEM images for (a-c) NiO and (d-f) $Ni_{0.95}Zn_{0.05}O$.

7.3.2 Optical Properties

Dopant induced variation of optical band gap of $Ni_{1-x}Zn_xO$ nanoparticle is investigated by UV-Vis absorption studies. For direct band gap systems, the absorption coefficient is related to incident photon energy by Tauc relation [8] represented as

$$(\alpha h\nu)^2 = A(h\nu - E_g) \ldots\ldots\ldots\ldots\ldots\ldots (7.2)$$

Where E_g is the band gap of sample. From the plot of $(\alpha h\nu)^2$ versus $h\nu$ as shown in **Figure 7.4**, the band gap of $Ni_{1-x}Zn_xO$ is estimated. The monotonous enhancement of band gap from 4.01 eV to 4.07 eV with increase in *x* is shown in the inset of **Figure 7.4**.

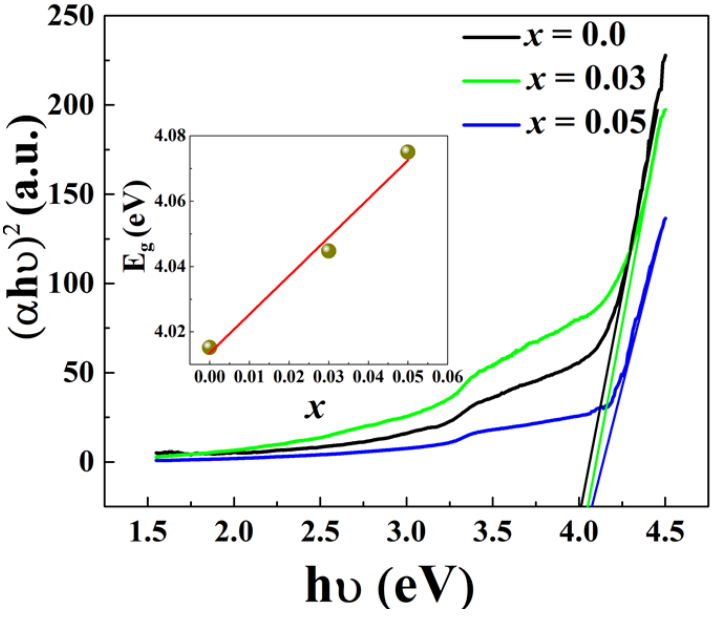

Figure 7.4: Tauc's plot of $Ni_{1-x}Zn_xO$ ($0.0 \leq x \leq 0.05$) nanoparticles. Inset shows the variation of band gap with x.

This result is consistent with the gradual decrease of the particle size with increase in dopant content and it occurs due to the quantum confinement [47]. The energy level spacing of electronic states of atom increases with reduction in dimensionality of particle in the nanoscale, which may be interpreted due to the quantum confinement [48]. The increment of band gap of NiO with increasing Zn doping concentration are also reported by U.K Panigrahi et. al., [27].

7.3.3 Dielectric and Transport Properties

Dielectric constant and loss tangent are the most significant parameters in order to understand the dielectric behavior of materials. Dielectric loss of a material is the instinctive loss of electromagnetic energy into heat. Dielectric measurements of $Ni_{1-x}Zn_xO$ ($0.0 \leq x \leq 0.05$) are performed in the temperature range 303 - 423 K at different frequency (f) of the ac source. Dielectric constant (ε_r) is defined as $\boldsymbol{\varepsilon_r = \frac{l \times C_p}{A \times \varepsilon_0}}$, where ε_0 is dielectric constant at vacuum, C_p is the capacitance, l and A are thickness and cross-sectional area of the pellet, respectively. The ac conductivity is given by

$$\boldsymbol{\sigma_{ac} = (2\pi f \varepsilon_0 \varepsilon_r \tan \delta)} \text{.....} \textbf{(7.3)}$$

Where tan δ is dielectric loss. Dielectric dispersion behavior at 303 K (**Figure 7.5(a)**) depicts that ε_r decreases rapidly with increasing frequency in low frequency region (~ 100 Hz) and beyond ~ 10^5 Hz, it becomes almost independent of frequency as observed commonly [49-50]. Gradual incorporation of Zn^{2+} in the lattice causes the enhancement of ε_r at high frequency (~ 2 MHz) as

demonstrated in the inset of **Figure 7.5(a)**. But at low frequency, the dielectric constant of the doped system changes reversely. The dielectric properties of a material depend upon different types of polarization, that is, dipolar, electronic, atomic, and space charge polarization. At low frequency, the dielectric constant increases with decreasing frequency which can be explained by Maxwell-Weigner model [51]. According to this model, dielectric medium consists of conductive grains separated by resistive grain boundaries. The charge carriers under external field can easily migrate through grains at low frequency and get accumulated at grain boundaries, which results a large polarization known as space charge polarization or interface polarization and hence high dielectric constant [52-55]. As the frequency increases the space charge polarization diminishes gradually; hence, the electronic and atomic contribution dominates. In the present case, the dielectric constant becomes almost constant at higher frequency indicating the dominance of electronic and atomic contribution. Enhancement of the dielectric constant with Zn doping may be attributed to the electrical heterogeneity of the Zn doped NiO.

In the low frequency region, as both the space charge polarization at grain boundary and sample electrode interface come to play, it is generally difficult to isolate them. In the present case, particle size of $Ni_{1-x}Zn_xO$ decreases with increase in x resulting increase in grain boundary. Still ε_r of $Ni_{1-x}Zn_xO$ at low frequency is the least for the most doped (x = 0.05) system. This may indicate

that the sample electrode interface polarization dominates over the grain boundary effect at low frequency. It is noteworthy to mention that electrode interface polarization is an extrinsic effect as it may depend on the type of electrode, roughness of the electrode, etc. Nevertheless, a regular decrease in dielectric value is observed at low frequency with increase in Zn^{2+} doping. This may be correlated with the gradual reduction of conductivity with the increase in Zn^{2+} doping as discussed below.

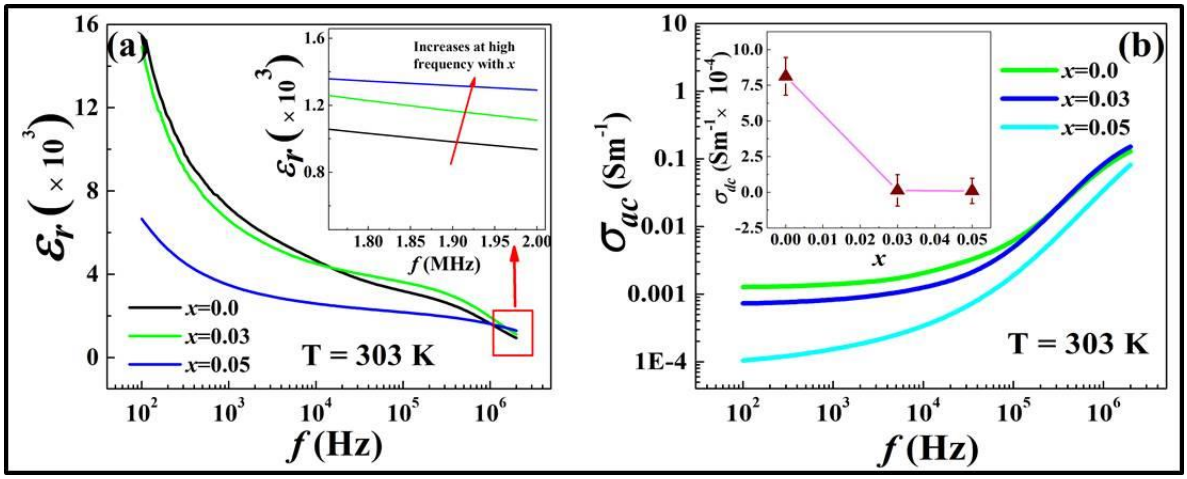

Figure 7.5: (a) Frequency variation of ε_r with its zoomed view at high frequency region in the inset. (b) Frequency variation of σ_{ac} and the inset indicates σ_{dc} versus x plot.

Figure 7.5(b) indicates the variation of σ_{ac} of $Ni_{1-x}Zn_xO$ ($0.0 \leq x \leq 0.05$) with f at 303 K. The σ_{ac} increases gradually with increasing frequency for all x. The frequency dependence of σ_{ac} is explained by Jonscher's power law [56] or ''universal dielectric response'' (UDR) law, given by

$$\boldsymbol{\sigma_{ac} = \sigma_{dc} + A\,\omega^{s}} \text{.....(7.4)}$$

Where σ_{dc} is the limiting zero frequency conductivity, A is pre-exponential constant, $\omega = 2\pi f$ is the angular frequency and s is the power law exponent where

$0 < s < 1$. The variation of σ_{dc} with x is shown in the inset of **Figure 7.5(b)**. It illustrates that dc conductivity decreases with increase of Zn doping into NiO matrix. The frequency independent conductivity i.e., dc conductivity is generally attributed by long-range migration of charge carriers.

Biju et al., [57] reported that the conductivity of NiO nanoparticles are found to be largely enhanced over that of NiO single crystals and this enhancement in conductivity is attributed to the high density of Ni^{2+} or oxygen vacancy in the nanoparticles. Here incorporation of Zn^{2+} in the NiO lattice gradually decreases the conductivity. This may be associated with the reduction of oxygen vacancies via defect compensation mechanism [58]. Moreover, the regular decrease in conductivity with increase in Zn^{2+} doping in $Ni_{1-x}Zn_xO$ can be attributed to the decrease in particle size with increasing x. Reduction of particle size leads to the increase in surface to volume ratio and hence large scattering. The lowering of conductivity with increase of Zn as dopant is also revealed from impedance spectroscopy. Impedance spectroscopy is a powerful tool in separating out the grain and grain boundary effects. The plot of imaginary impedance versus real component (shown in **Figure 7.6(a)**) appearing in the form of arc of a semicircle, is known as Nyquist plot. The plots contain a large semicircular arc with nonzero intercept on the Z' axis in the lower frequency range (away from origin) representing the contribution of grain boundaries [58]. The nature of the curves indicates that capacitance (C_{gb}) and resistance (R_{gb}) of the grain boundary are in

parallel. The intercept of the semicircular arc on the real axis gives the value of R_{gb}. The impedance data are fitted using EIS Spectrum Analyzer software with suitable equivalent circuit [59] from which the impedance parameters, C_{gb} and R_{gb} are estimated. The inset of **Figure 7.6(a)** shows the variation of C_{gb} and R_{gb} with x along with the equivalent circuit of the system. The energy dissipation in the dielectric system is estimated from loss factor (tan δ). **Figure 7.6(b)** shows the variation of dielectric loss with frequency at 303 K in the frequency range 100 Hz – 2 MHz. Inset of **Figure 7.6(b)** illustrates the significant decrease of dielectric loss with increase of dopant content (x) even at high frequency. Enhancement of dielectric constant accompanied with lowering dielectric loss due to Zn doping makes $Ni_{0.95}Zn_{0.05}O$ a potential candidate for high frequency device.

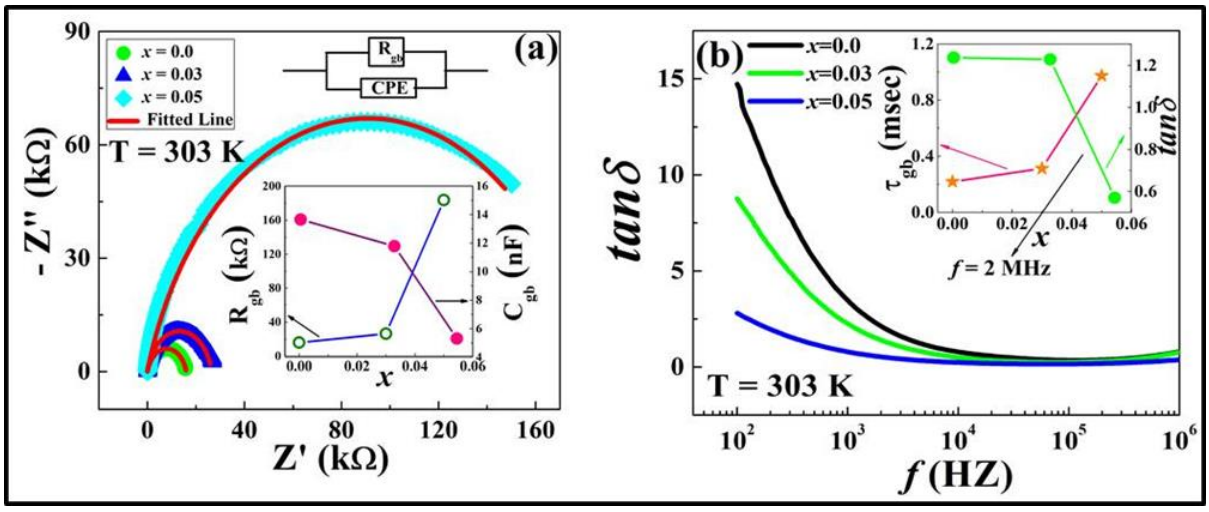

Figure 7.6:.(a) The Nyquist plot of $Ni_{1-x}Zn_xO$ ($0.0 \leq x \leq 0.05$) and variation of impedance parameters with x in the inset. (b) Frequency variation of loss for different doping content (x) and variation of relaxation time (τ_{gb}) and loss at 2 MHz with x in the inset.

Absence of peak in dielectric loss plot reveals the large relaxation time (τ_{gb}) which is estimated as $\boldsymbol{\tau_{gb} = R_{gb} \times C_{gb}}$. The variation of τ_{gb} with x is shown in the inset

of **Figure 7.6(b)**. In order to investigate the temperature dependence of dielectric, transport properties and relaxation mechanism, two representative members of $Ni_{1-x}Zn_xO$ with x = 0.0 and 0.05 corresponding to the highest and lowest conductivity at 303 K among the series members, are selected for further study. The temperature variation of σ_{ac} for x = 0.0 and 0.05 in the temperature range 303 ≤ T ≤ 423 K are depicted in **Figure 7.7(a)** and **Figure 7.7(b)**, respectively. Both members exhibit the increase of conductivity with increase in temperature.

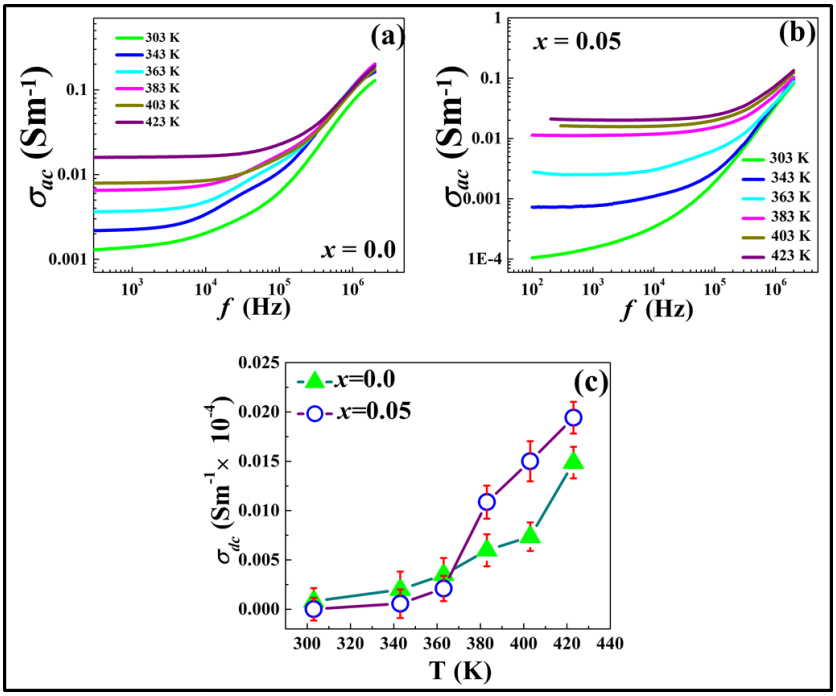

Figure 7.7: Frequency variation of σ_{ac} for (a) x = 0.0 and (b) x = 0.05 at different temperatures and the temperature variation of σ_{dc} for x = 0.0 and 0.05 in the Fig.7.7(c) are shown.

Beyond 365 K, σ_{dc} of x = 0.05 becomes more than that of x = 0.0 as shown in **Figure 7.7(c)**. This cross over may indicate the lowering of the barrier at the grain boundaries facilitating the charge transport. The activation energy of the conduction process induced by long range hopping of oxygen vacancy [60-61]

has been estimated using the Arrhenius law given by $\boldsymbol{\sigma_{dc} = \sigma_0 exp\left(\frac{-E_a}{k_B T}\right)}$, where E_a is the activation energy, k_B is Boltzmann constant, T is temperature and σ_0 is pre-exponential factor. Activation energy is calculated from the slope of "ln σ_{dc} vs 1000/T" plot as shown in **Figure 7.8(a)**. and **Figure 7.8(b)** for x = 0.0 and 0.05, respectively.

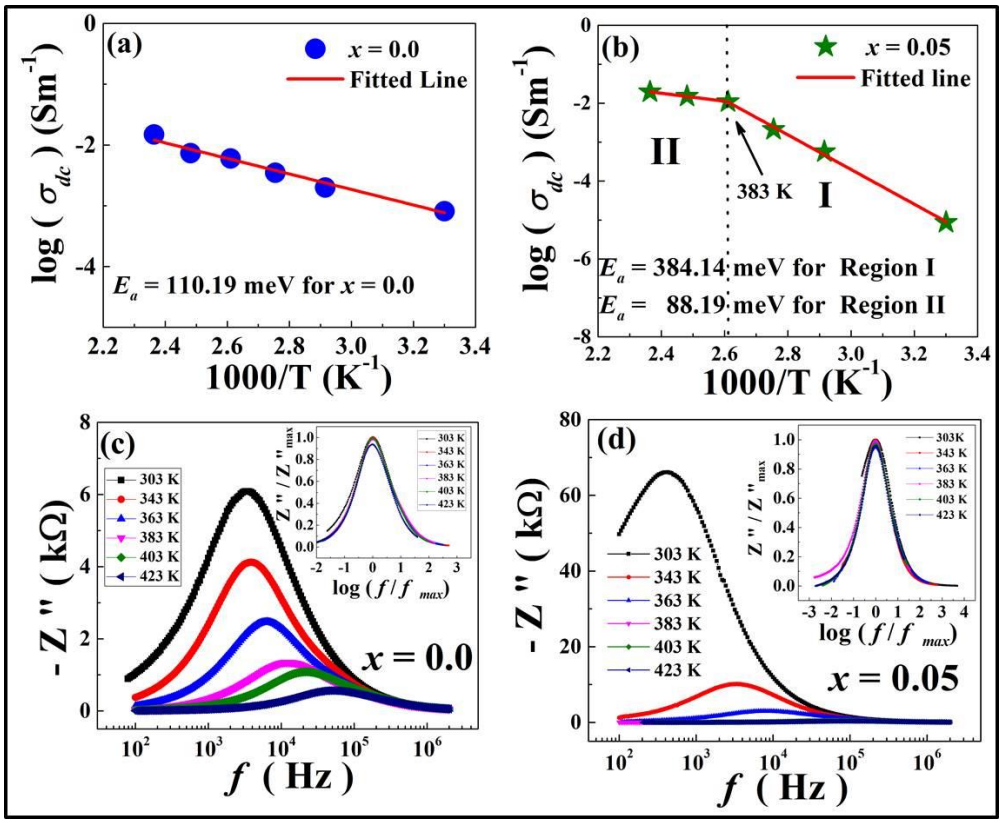

Figure 7.8: (a) and (b) log (σ_{dc}) versus 1000/T for x = 0.0 and x = 0.05, respectively. (c) and (d) frequency variation of –Z" at different temperature with Z"/Z"$_{max}$ versus log (f/f$_{max}$) in the corresponding inset for x = 0.0 and x = 0.05, respectively.

In case of undoped NiO , the activation energy is found to be 110.2 meV, while that of $Ni_{0.95}Zn_{0.05}O$ are 384.14 meV and 88.19 meV in the temperature range 303-383 K and 383-423 K, respectively. Increase in activation energy due to increasing Zn doping in the temperature region 303 ≤ T ≤ 383K, may indicate the

reduction of oxygen vacancies. [60, 62]. Biju et al., [57] reported that the activation energy of NiO nanoparticles is ~ 600 meV which is quite large compared to this report. The difference in activation energy could be due to the difference in the density of polarons associated with the Ni^{2+} [57] and distortion of unit cell volume due to Zn^{2+} doping.

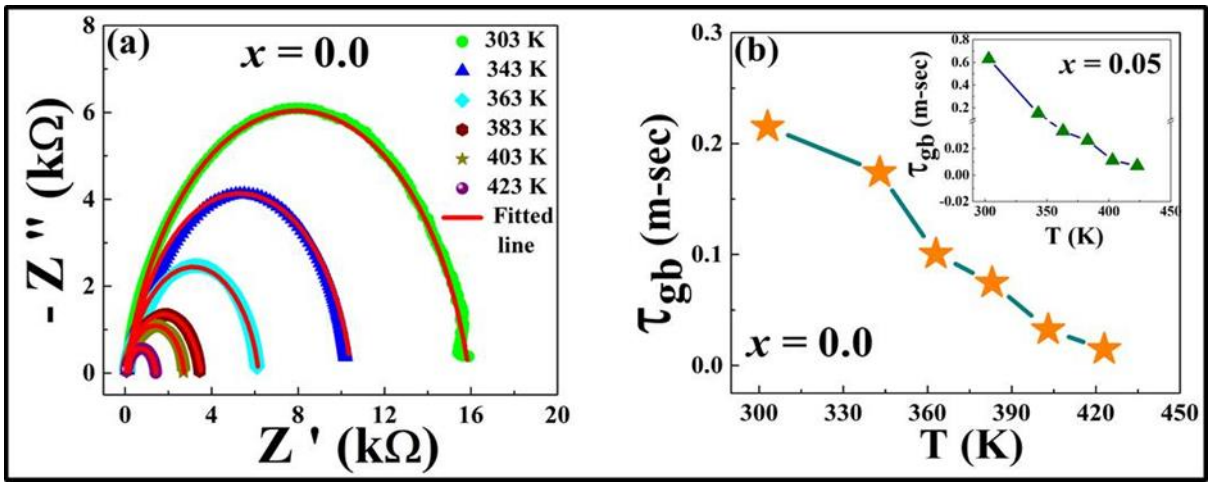

Figure 7.9: (a) Nyquist plots for x = 0.0 at different temperatures. (b) The temperature variation of relaxation time for x = 0.0 and inset of (b) shows the temperature variation of relaxation time for x = 0.05.

The relaxation mechanism may be investigated from the frequency dependence of real (Z') and imaginary (Z'') part of the electrical impedance at different temperature. The frequency dependence of Z'' at different temperatures as presented in **Figure 7.8(c)** and **Figure 7.8(d)** for x = 0.0 and 0.05, respectively, exhibit a peak at a particular frequency (f_{max}). With increasing temperature, peaks shift to higher frequency due to the reduction of the relaxation time indicating short-range hopping conductivity of oxygen vacancy [58, 63]. This type of temperature dependence of relaxation time is common as observed in most crystalline semiconductor [64-66]. The Z''/Z''_{max} versus log (f/f_{max}) plots are

shown in the inset of **Figure 7.8(c)** and **Figure 7.8(d)** for x = 0.0 and 0.05, respectively, for various temperatures. Coincidence of all the plots reveals the temperature independent relaxation mechanism. Nyquist representations at different temperatures for x = 0.0 are shown in **Figure 7.9(a)**. The impedance data are fitted using suitable equivalent circuit [67-70] in EIS Spectrum Analyzer software. It is seen that single semicircles are appeared for different temperatures and radius of semicircles decrease with increasing temperature. This indicates the decrease in resistance of grain boundary with increasing temperature as expected from conductivity result. Nyquist plots for x = 0.05 are found to be similar to that of x = 0.0. Resistances and capacitances of the grain boundary at different temperatures are estimated from impedance data fitting. Gradual decrease of relaxation time with increase in temperature for both for x = 0.0 and 0.05 is evident in **Figure 7.9(b)**.

7.4 Summary and Conclusions

$Ni_{1-x}Zn_xO$ ($0.0 \leq x \leq 0.05$) nanoparticles are synthesized by chemical precipitation method to study the doping induced effect on the dielectric and transport properties. The structural and morphological characterizations of samples are executed using XRD, FE-SEM and TEM. XRD results support the incorporation of Zn^{2+} into the NiO lattice either by the replacing of Ni^{2+} ion or by placing in the Ni^{2+} vacancy site. Thus incorporation of Zn^{2+} may take part in the process of reduction of oxygen vacancy. It is seen that the average grain size decreases with

Zn doping content (x). Optical band gap (E_g) as estimated from UV-Vis measurements reveal blue shift with increase of Zn as dopant content. AC conductivity (σ_{ac}), dielectric constant (ε_r) and dielectric loss (tan δ) of $Ni_{1-x}Zn_xO$ ($0 \leq x \leq 0.05$) are studied as a function of frequency (f). DC conductivity (σ_{dc}), estimated from Jonscher Power Law or universal dielectric response fit of ac conductivity at 303 K decreases with inclusion of Zn in the NiO lattice. The contributions of dc conduction and universal dielectric response to the relaxation may be associated with long-range motion of the doubly-ionized oxygen vacancies and short-range hopping of oxygen vacancies. The reduction of σ_{dc} with increase in Zn^{2+} doping may be attributed to the reduction of oxygen vacancy via defect compensation mechanism. Temperature dependence of σ_{dc} of $Ni_{1-x}Zn_xO$ ($0.0 \leq x \leq 0.05$) indicates the semiconducting nature. Cross over of dc conductivity (σ_{dc}) of $Ni_{0.95}Zn_{0.05}O$ to that of NiO is observed ~ 365 K. This cross over may indicate the lowering of the barrier at the grain boundaries facilitating the charge transport. The dielectric loss decreases significantly with increase of dopant content (x) at high frequency. Enhancement of dielectric constant accompanied with lowering dielectric loss due to Zn doping makes $Ni_{0.95}Zn_{0.05}O$ a potential candidate for high frequency device.

7.5 References

1. R. Roy, R.A. Roy, D.M. Roy, Alternative perspectives on "Quasi-Crystallinity": non-uniformity and nanocomposites. Materials Letters 4, 323-328 (1986)
2. S. Kanchana, M. Jay Chithra, S. Ernest, K. Pushpanathan, Violet emission from Fe doped ZnO nanoparticles synthesized by precipitation method. Journal of Luminescence 176, 6-14 (2016)
3. M. Jay Chithra, M. Sathya, K. Pushpanathan, Effect of pH on crystal size and photoluminescence property of ZnO nanoparticles prepared by chemical precipitation method. Acta. Metall. Sin. (Engl. Lett.) 28(3), 394-404 (2015)
4. C. Shi, Y. Zhu, Q. Xu, N. Zhang, T. Xie, Z. Wang, H. Fan, Morphology modulation and gas sensitivity improvement of indium oxide semiconductor nanomaterials. J. Mater. Sci.: Mater. Electron. 31, 5047-5053 (2020)
5. I.M. El-Nahhal, S.M. Zourab, F.S. Kodeh, A.A. Elmanama, M. Selmane, I. Genois, F. Babonneau, Nano-structured zinc oxide-cotton fibers: synthesis, characterization and applications. J. Mater. Sci.: Mater. Electron. 24, 3970-3975 (2013)

6. G. Liu, M. Peng, W. Song, H. Wang, D. Zou, An 8.07% efficient fiber dye-sensitized solar cell based on a TiO2 micron-core array and multilayer structure photoanode. Nano Energy 11, 341-347 (2015)
7. W.T. Chang, Y.C. Chen, K.S. Kao, Y.H. Chu, C.C. Cheng, Design and fabrication of a double-sided piezoelectric transducer for harvesting vibration power. Thin Solid Films 529, 39-44 (2013)
8. A. Mondal, S. Sarkar, N. Giri, S. Chatterjee, R. Ray, Magnetic phase separation in diluted magnetic system: Zn1-xFexO. Acta Metall. Sin. (Engl. Lett.) 30(6), 521-527 (2017)
9. A. Mondal, N. Giri, S. Sarkar, R. Ray, Magnetic properties of $Zn_{1-x}Ni_xO$. AIP Conference Proceedings 1953, 120017 1-4 (2018)
10. C. Li, Y. Liu, L. Li, Z. Du, S. Xu, M. Zhang, X. Yin, T. Wang, A novel amperometric biosensor based on NiO hollow nanospheres for biosensing glucose. Talanta 77, 455-459 (2008)
11. K. Kaviyarasu, P.A. Devarajan, Synthesis and characterization studies of cadmium doped MgO nanocrystals for optoelectronics application. Advances in Applied Science Research 2(6), 131-138 (2011)
12. A. Franco Jr., H.V.S. Pessoni, Enhanced dielectric constant of Co-doped ZnO nanoparticulate powders. Physica B: Condensed Matter 476, 12-18 (2015)

13. C. Thangamani, K. Pushpanathan, Optical and magnetic behavior of NiZnO nanoparticles. Journal of Chemical and Pharmaceutical Sciences. special issue 11, 111-113 (2015)
14. I. Hotovy, J. Huran, L. Spiess, S. Hascik, V. Rehacek, Preparation of nickel oxide thin films for gas sensors applications. Sensors and Actuators B 57, 147-152 (1999)
15. C. Thangamani, K. Pushpanathan, Optical and dielectric behavior of NiO: Zn quantum dots. J. Chem. Pharm. Res. 8(8), 749-757 (2016)
16. S.G. Danjumma, Y. Abubakar, S. Suleiman, Nickel oxide (NiO) devices and applications: a review. International Journal of Engineering Research & Technology (IJERT) 8(4), 461-467 (2019)
17. X. Wang, J. Song, L. Gao, J. Jin, H. Zheng, Z. Zhang, Optical and electrochemical properties of nanosized NiO via thermal decomposition of nickel oxalate nanofibres. Nanotechnology 16, 37-39 (2005)
18. K. Deevi, V.S.R. Immareddy, Synthesis and characterization of optically transparent nickel oxide nanoparticles as a hole transport material for hybrid perovskite solar cells. J. Mater. Sci.: Mater. Electron. 30, 6242-6248 (2019)
19. B. Kowsalya, V.V. Anusha Thampi, V. Sivakumar, B. Subramaniun, Electrochemical detection of chromium(VI) using NiO nanoparticles. J. Mater. Sci.: Mater. Electron. 30, 14755-14761 (2019)

20. H. Sato, T. Minami, S. Takata, T. Yamada, Transparent conducting p-type NiO thin films prepared by magnetron sputtering. Thin Solid Films 236, 27-31 (1993)

21. W. Wei, X. Jiang, L. Lu, X. Yang, X. Wang, Study on the catalytic effect of NiO nanoparticles on the thermal decomposition of TEGDN/NC propellant. J. Hazard Mater. 168, 838-842 (2009)

22. Y. Wang, J. Zhu, X. Yang, L. Lu, X. Wang, Preparation of NiO nanoparticles and their catalytic activity in the thermal decomposition of ammonium perchlorate. Thermochimica Acta 437, 106-109 (2005)

23. G.A. Sawatzky, J.W. Allen, Magnitude and origin of the band gap in NiO. Physical Review Letters 53(24), 2339-2342 (1984)

24. A. Alejandre, F. Medina, P. Salagre, A. Fabregat, J.E. Sueiras, Characterization and activity of copper and nickel catalysts for the oxidation of phenol aqueous solutions. Applied Catalysis B: Environmental 18, 307-315 (1998)

25. F. Li, H. Chen, C. Wang, K. Hu, A novel modified NiO cathode for molten carbonate fuel cells. J. Electroanal. Chem. 531, 53-60 (2002)

26. K. Sathishkumar, N. Shanmugam, N. Kannadasan, S. Cholan, G. Viruthagiri, Influence of Zn2+ ions incorporation on the magnetic and pseudo capacitance behaviors of NiO nanoparticles. Mat. Sci. Semicon. Proc. 27, 846-853 (2014)

27. U.K. Panigrahi, P.K. Das, P.D. Babu, N.C. Mishra, P. Mallick, Structural, optical and magnetic properties of Ni1-xZnxO/Ni nanocomposite. SN Applied Sciences 1:438 (2019). [https://doi.org/10.1007/s42452-019-0461-0]

28. J. Al Boukhari, L. Zeidan, A. Khalaf, R. Awad, Synthesis, Characterization, Optical and Magnetic Properties of Pure and Mn, Fe and Zn doped NiO Nanoparticles. Chemical Physics 29 July, 2018 [https://doi.org/10.1016/j.chemphys.2018.07.046]

29. F.R. Marcos, C.V. Manzano, J.J. Reinosa, J.J. Romero, P. Marchet, M.S.M. González, J.F. Fernández, Mechanism of $Ni_{1-x}Zn_xO$ formation by thermal treatments on NiO nanoparticles dispersed over ZnO. J. Phys. Chem. C 115, 13577-13583 (2011).

30. J. Wang, X. Wei, P. Wangyang, Gas-sensing devices based on Zn-doped NiO two-dimensional grainy films with fast response and recovery for ammonia molecule detection. Nanoscale Research Letters 10:461, 1-9 (2015).

31. J. Wang, L. Wei, L. Zhang, J. Zhang, H. Wei, C. Jiang, Y. Zhang, Zinc-doped nickel oxide dendritic crystals with fast response and self-recovery for ammonia detection at room temperature. J. Mater. Chem. 22, 20038-20047 (2012).

32. N. Giri, S. Das, S. Sarkar, A. Mondal, S. Giri, R. Ray, Doping induced tailoring of exchange bias effect in granular $Ni_{1-x}Zn_xO$ film. Physica B: Condensed Matter 570, 229-231 (2019).

33. B. Gokul, P. Matheswaran, K.M. Abhirami, R. Sathyamoorthy, Structural and dielectric properties of NiO nanoparticles. J. Non-Cryst. Solids 363, 161-166 (2013)

34. K. Karthik, G.K. Selvan, M. Kanagaraj, S. Arumugam, N.V. Jaya, Particle size effect on the magnetic properties of NiO nanoparticles prepared by a precipitation method. J. Alloys Compd. 509, 181-184 (2011)

35. S.P. Raja, C. Venkateswaran, Study of magnetic and electrical properties of nanocrystalline Mn doped NiO. J. Nanosci. Nanotechnol. 11, 2747-2751 (2011)

36. M. Yang, H. Pu, Q. Zhou, Q. Zhang, Transparent p-type conducting K-doped NiO films deposited by pulsed plasma deposition. Thin Solid Films 520, 5884-5888 (2012)

37. T. Dutta, P. Gupta, A. Gupta, J. Narayan, Effect of Li doping in NiO thin films on its transparent and conducting properties and its application in heteroepitaxial p-n junctions. J. Appl. Phys. 108, 083715-1-7 (2010)

38. N.S. Das, B. Saha, R. Thapa, G.C. Das, K.K. Chattopadhyay, Band gap widening of nanocrystalline nickel oxide thin films via phosphorus doping. Physica E: Low dimension. Syst. Nanostruct. 42, 1377-1382 (2010)

39. Z.G. Yang, L.P. Zhu, Y.M. Guo, Z.Z. Ye, B.H. Zhao, Preparation and band-gap modulation in MgxNi1-xO thin films as a function of Mg contents. Thin Solid Films 519, 5174-5177 (2011)

40. R. Sharma, A.D. Acharya, S. Moghe, S.B. Shrivastava, M. Gangrade, T. Shripathi, V. Ganesan, Effect of cobalt doping on microstructural and optical properties of nickel oxide thin films. Mater. Sci. Semicond. Proc. 23, 42-49 (2014)

41. W.L. Jang, Y.M. Lu, W.S. Hwang, W.C. Chen, Electrical properties of Li-doped NiO films. Journal of the European Ceramic Society 30, 503-508 (2010)

42. D.D. Dogan, Y. Caglar, S. Llican, M. Caglar, Investigation of structural, morphological and optical properties of nickel zinc oxide films prepared by sol-gel method. J. Alloys Compd. 509, 2461-2465 (2011)

43. R. Noonuruk, W. Techitdheera, W. Pecharapa, Characterization and ozone-induced coloration of ZnxNi1-xO thin films prepared by sol-gel method. Thin Solid Films 520, 2769-2775 (2012)

44. N. Giri, A. Mondal, S. Sarkar, R. Ray, Structural and dielectric properties of Zn1-xAlxO nanoparticles. AIP Conf. Proc. 1953, 050011-1-4 (2018)

45. G.K. Williamson and W.H. Hall, X-ray Line Broadening from Filed Aluminium and Wolfram. Acta Metall. 1, 22-31 (1953).

46. A. Mondal, N. Giri, S. sarkar, S. Majumdar, R. Ray, Tuning the photocatalytic activity of ZnO by TM (TM= Fe, Co, Ni) doping. Materials Science in Semiconductor Processing 91, 333-340 (2019)

47. T. Takagahara, K. Takeda, Theory of the quantum confinement effect on excitons in quantum dots of indirect-gap materials. Phys. Rev. B 46, 15578-15581 (1992)

48. Kirti Vishwakarma, A review on variation in band energy of quantum dot with size. International Journal for Technological Research in Engineering volume 6, Issue 11, July-2019, ISSN 2347 - 4718. [https://ijtre.com/images/scripts/2019061117.pdf]

49. S. Sarkar, A. Mondal, K. Dey, R. Ray, Defect driven tailoring of colossal dielectricity of reduced graphene oxide. Mater. Res. Bull. 74, 465-471 (2016)

50. D. O'Neill, R.M. Bowman, J.M. Gregg, Dielectric enhancement and maxwell-wagner effects in ferroelectric superlattice structures. Appl. Phys. Lett. 77, 1520-1522 (2000)

51. R. Zamiri, A. Kaushal, A. Rebelo, J.M.F. Ferreira, Er doped ZnO nanoplates: synthesis, optical and dielectric properties. Ceram. Int. 40(1), 1635-1639 (2014)

52. Y. Li, L. Fang, L. Liu, Y. Huang, C. Hu, Giant dielectric response and charge compensation of Li- and Co- doped NiO ceramics. Materials Science and Engineering B 177, 673-677 (2012)

53. L. Liu, Y. Huang, C. Su, L. Fang, M. Wu, C. Hu, H. Fan, Space-charge relaxation and electrical conduction in $K_{0.5}Na_{0.5}NbO_3$. Appl. Phys. A 104, 1047-1051 (2011)

54. Y. Huang, D. Shi, Y. Li, G. Li, Q. Wang, L. Liu, L. Fang, Effect of holding time on the dielectric properties and non-ohmic behavior of $CaCu_3Ti_4O_{12}$ capacitor-varistors. J. Mater. Sci: Mater. Electron 24, 1994-1999 (2013)

55. L. Liu, H. Fan, L. Wang, X. Chen, P. Fang, Dc-bias-field-induced dielectric relaxation and ac conduction in $CaCu_3Ti_4O_{12}$ ceramics. Philosophical Magazine 88(4), 537-545 (2008)

56. A.K. Jonscher, The 'universal' dielectric response. Nature 267, 673-679 (1977)

57. V. Biju, M.A. Khadar, DC conductivity of consolidated nanoparticles of NiO. Mater. Res. Bull. 36, 21-23 (2001)

58. J. Deng, X. Sun, S. Liu, L. Liu, T. Yan, L. Fang, B. Elouadi, Influence of interface point defect on the dielectric properties of Y doped $CaCu_3Ti_4O_{12}$ ceramics. J. Advc. Dielectrics 6(1), 1650009 1-9 (2016)

59. J.C. Ronfard-Haret, J. Kossanyi, J.L. Pastol, Electroluminescence of the Er3+ion and electric conduction in polycrystalline ZnO: Mn, Bi, Er sintered pellets. J. Phys. Chem. Solids 62, 565-578 (2001)

60. S. Zheng, D. Shi, L. Liu, G. Li, Q. Wang, L. Fang, B. Elouadi, Oxygen vacancy-related dielectric relaxation and electrical conductivity in La-doped $Ba(Zr_{0.9}Ti_{0.1})O_3$ ceramics. J. Mater Sci: Mater Electron 25, 4058-4065 (2014)

61. Y. Huang, L. Liu, D. Shi, S. Wu, S. Zheng, L. Fang, C. Hu, B. Elouadi, Gaint dielectric permittivity and non-linear electrical behavior in $CaCu_3Ti_4O_{12}$ varistors from the molten-salt synthesized powder. Ceramics International 39, 6063-6068 (2013)

62. F. Han, S. Ren, J. Deng, T. Yan, X. Ma, B. Peng, L. Liu, Dielectric response mechanism and suppressing high-frequency dielectric loss in Y_2O_3 grafted $CaCu_3Ti_4O_{12}$ ceramics. J. Mater. Sci: Mater. Electron 28(22), 17378-17387 (2017)

63. J. Deng, L. Liu, X. Sun, S. Liu, T. Yan, L. Fang, B. Elouadi, Dielectric relaxation behavior and mechanism of $Y_{2/3}Cu_3Ti_4O_{12}$ ceramic. Materials Research Bulletin 88, 320-329 (2017)

64. A. Benali, M. Bejar, E. Dhahri, M.F.P. Graça, L.C. Costa, Electrical conductivity and ac dielectric properties of La0.8Ca0.2-xPbxFeO3 (x =

0.05, 0.10 and 0.15) perovskite compounds. J. Alloys Compd. 653, 506-512 (2015)

65. N. Chihaoui, M. Bejar, E. Dhahri, M.A. Valente, M.P.F. Graça, L.C. Costa, Dielectric relaxation of the Ca2MnO4-δ system. J. Alloys Compd. 577S, S483-S487 (2013)
66. A. Omri, M. Bejar, E. Dhahri, M. Es-Souni, M.A. Valente, M.P.F. Graça, L.C. Costa, Electrical conductivity and dielectric analysis of La0.75(Ca,Sr)0.25Mn0.85Ga0.15O3 perovskite compound. J. Alloys Compd. 536, 173-178 (2012)
67. D.W. Davidson, R.H. Cole, Dielectric relaxation in glycerol, propylene glycol, and n-propanol. J. Chem. Phys. 19, 1484-1490 (1951)
68. S. Havriliak, S. Negami, A complex plane representation of dielectric and mechanical relaxation processes in some polymers. Polymer 8, 161-210 (1967)
69. K.S. Cole, R.H. Cole, Dispersion and absorption in dielectrics I. alternating current characteristics. J. Chem. Phys. 9, 341-351 (1941)
70. K.S. Cole, R.H. Cole, Dispersion and absorption in dielectrics II. direct current characteristics. J. Chem. Phys. 10, 98-105 (1942)

8 Structural and Dielectric Properties of $Zn_{1-x}Al_xO$ nanoparticles

8.1 Introduction

Zinc Oxide (ZnO) is a metal oxide semiconductor having wide direct band gap (3.37 eV) and large exciton binding energy (60 meV) making it a potential candidate for various applications such as opto-electronic devices, transparent high power and high frequency electronic devices, piezo-electronic transducers. It is one of the n-type metal oxide semiconductor due to the presence of native donor defects such as oxygen vacancies and Zn interstitials. Transport properties of ZnO can be tailored by incorporating the defects in it. Several attempts have been made to introduce defects by doping extrinsic n-type dopants like Al, Ga, B, In, etc [1-5], which exhibit improved conductivity as well as optical transparency. These n-type doping makes ZnO a potential candidate for application as transparent conducting electrodes, solar cells, optoelectronics etc. Improved optical properties and dc conductivity of Al doped ZnO thin film had been reported by Al-Ghamdi et al. [6]. However, basic understanding of role of the defect needs detail ac conductivity and dielectric studies. Here, we have reported the dopant (Al) content dependence of ac conductivity (σ_{ac}), dielectric constant (ε_R), dielectric loss (tan δ) of $Zn_{1-x}Al_xO$ ($0 \leq x \leq 0.11$) at room temperature.

8.2 Experimental Details

AZO sample were prepared using chemical precipitation method [7]. $Zn(CH_3COO)_2.2H_2O$ and $Al(NO_3)_3.9H_2O$ selected as a source of zinc and aluminium, respectively, were taken in stoichiometric ratio for different doping concentration x = 0.0, 0.01, 0.03, 0.04, 0.05, 0.10. 25 ml aqueous solution of $Al(NO_3)_3.9H_2O$ was added drop wise into $Zn(CH_3COO)_2.2H_2O$ in 50 ml de-ionised water solution with continuous magnetic stirring and heating at 70 ^{0}C. 1 gm of PVP in 100 ml de-ionised water was added slowly into the precursor solution. In order to maintain homogeneity of mixture, magnetic stirring were continued for 2 hrs. Next, 0.75 M aqueous solution of NaOH was added dropwise. A white voluminuous precipitate appeared just after NaOH addition. NaOH presents in precipitate as impurity. It was washed out using deionised water and ethanol several times. Finally, the product was dried in hot air oven at 90 ^{0}C for 3 hrs.

AZO samples were characterized by X-ray diffraction (model: Rigaku TTRAX III) using CuK_α radiation with wavelength 1.5406 Å. The morphology and grain size distribution of nanoparticles were investigated by field emission scanning electron microscope (FESEM, model: JEOL, JSM-7610F) images. For measurement of transport properties, the obtained $Zn_{1-x}Al_xO$ powder were pressed into pellet of 1cm diameter and~5 mm thickness, and sintered at 80 ^{0}C for 2 hours in order to get thermal stability. Gold foils with 1 cm diameter were used as

electrodes for measuring the σ_{ac}, ε_R and tan δ. These measurements were carried out at room temperature using an impedance analyzer (model: Agilent 4294A Precision Impedance Analyzer).

8.3 Results and Discussions

8.3.1 Structural Properties: XRD, FESEM Studies

The X-ray diffraction patterns of $Zn_{1-x}Al_xO$ are shown in **Figure 8.1(a)**. Each peaks indicate different (h k l) planes of pure ZnO having single-phase Wurtzite structure following JCPDS file (Card No. 36-1451, space group p63mc).The dimension (D) of different AZO samples is estimated by using Scherrer's formula [8] given by

$$\boldsymbol{\beta \cos \theta = \frac{0.89\lambda}{D} + 2\varepsilon \sin \theta} \text{.....(8.1)}$$

Where ε is the microstrain, β is full width half maxima (FWHM), λ is the wavelength of the CuK_α radiation.

Figure 8.1(b) demonstrates that particle size of $Zn_{1-x}Al_xO$ decreases with increase of Al doping for $x \leq 0.03$. However, farther doping does not lead to any change in particle size. The lattice parameters a and c estimated from Reitveld refinements (inset of **Figure 8.1(b)**) does not reveal any significant change with Al^{3+} doping. The FESEM images explicate the morphology and size of the particles. The FESEM image of $Zn_{1-x}Al_xO$ nanoparticle is shown in **Figure 8.2(a)** and corresponding particle size distribution is shown in **Figure 8.2(b)**. The particle

size obtained from FESEM is commensurate with XRD results for different AZO nanoparticles.

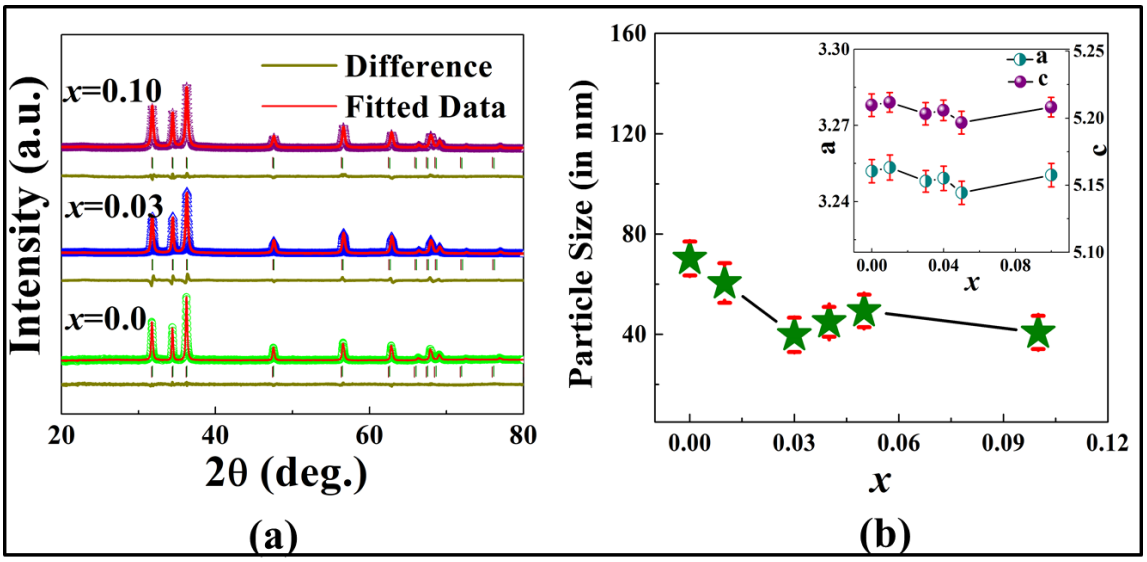

Figure 8.1: Rietveld analysis of XRD for x = 0.0, 0.03, 0.10 are shown in (a), particle size variation with x is shown in (b), variation of lattice parameters with x is shown in inset of (b).

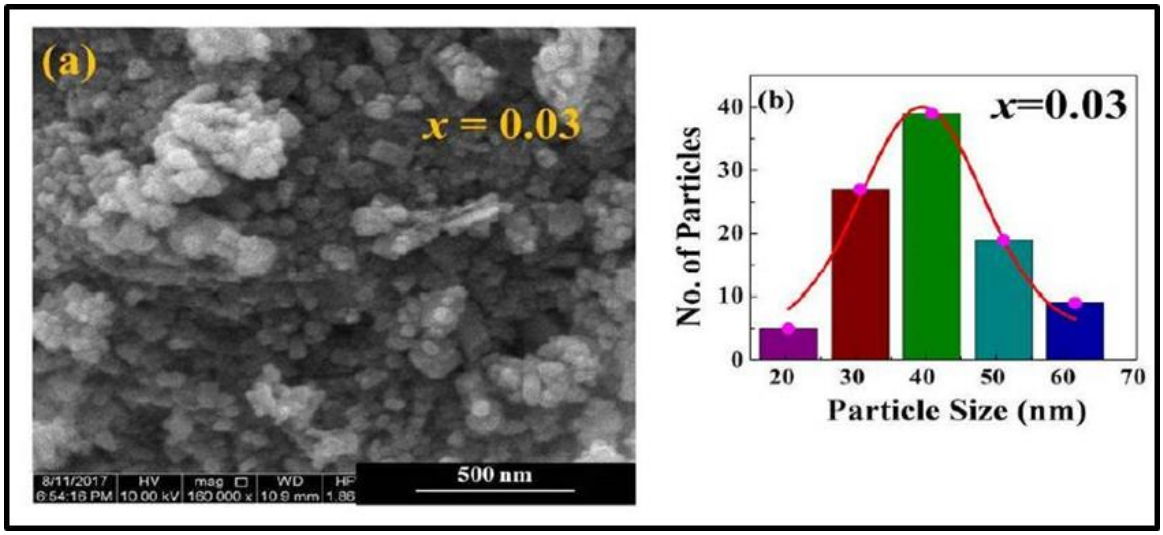

Figure 8.2: FE-SEM image of $Zn_{1-x}Al_xO$ (x = 0.03) is shown in (a) and corresponding particle distribution is shown in (b).

8.3.2 Transport Properties

Dielectric measurements of undoped ZnO and AZO nanoparticles are performed as a function of ω at 300 K. The working formula for ac conductivity is given by:

$$\boldsymbol{\sigma_{ac} = \omega \varepsilon_0 \varepsilon_R \tan \delta} \text{.....(8.2)}$$

Where ω is frequency, ε_0 is dielectric constant at vacuum, tan δ is dielectric loss.

$$\boldsymbol{\varepsilon_R = \frac{(l * C_p)}{(A * \varepsilon_0)}} \text{.....(8.3)},$$

is dielectric constant of the medium where C_p is the capacitance, l and A are thickness and cross-sectional area of pellet, respectively. Dielectric dispersion behavior (**Figure 8.3(a)**) depicts that ε_R decreases rapidly with increasing frequency in the low frequency region (~100 Hz) and becomes almost frequency independent beyond ~10^5 Hz. This can be explained by Maxwell-Weigner model [9]. According to this model, dielectric medium consists of a conducting grains separated by resistive grain boundaries. Based on this model Gupta et al. suggested that each nano grain behaves like a nano dipole [10]. Therefore as the grain size decreases number of nano dipole per unit volume increases and hence the dielectric constant increases.

At low ω, space charge polarization and low conductivity of grain boundary are the main reasons of high ε_R. In the high frequency limit ε_R becomes frequency independent as hopping between medium and dopant ions (Zn^{2+}, Al^{3+}) cannot follow the high frequency field and thus lag behind it [11]. Inset of **Figure 8.3(a)** demonstrates that in the low frequency region ε_R initially increases with doping

exhibiting maximum ~ x = 0.03 followed by the decrement with larger doping. The enhancement in ε_R may be due to the fact that Al^{3+} ion induces free charge carriers in the system, hence the high polarisability of conductive particles can be responsible for the increase in dielectric constant. This enhancement of dielectric constant is consistent with the increase of both ac and dc conductivity as discussed later. Moreover, this enhancement of dielectric constant is in harmony with the grain size which becomes minimum ~ x = 0.03. But beyond this threshold limit (i.e., x = 0.03 in this case) incorporation of more dopant (Al^{3+}) may cause partial reduction of oxygen vacancies which in turn reduces the conductivity as well as dielectric constant.

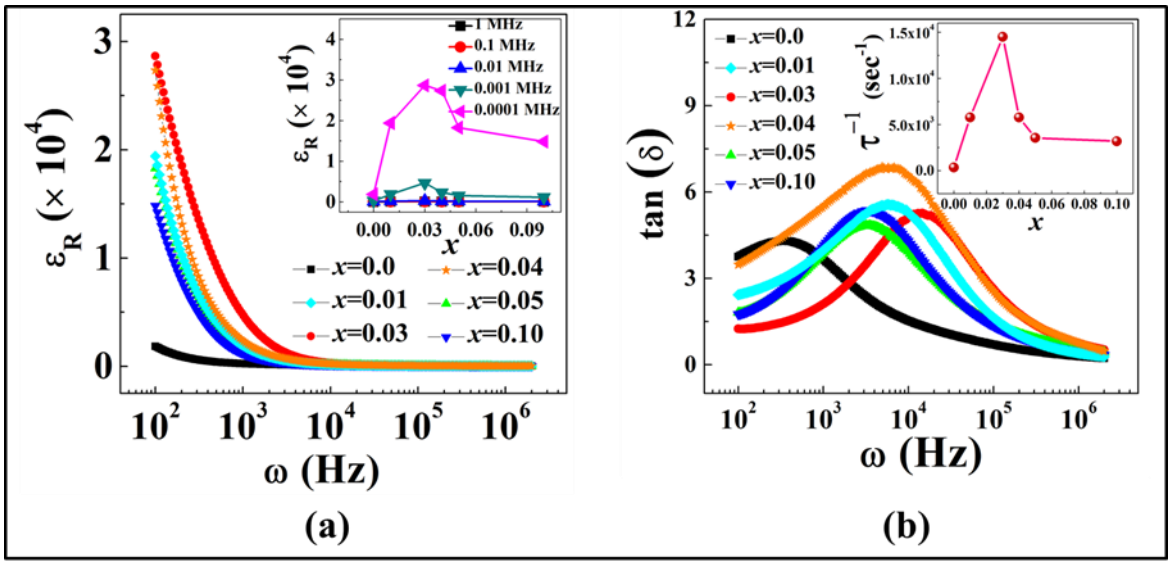

Figure 8.3: Variation of ε_R with frequency are shown in (a) and with x are shown in inset of (a) for $Zn_{1-x}Al_xO$ ($0.0 \leq x \leq 0.10$), tan δ vs ω plot for x = 0.0, 0.03, 0.10 are shown in (b) and τ^{-1} vs x is shown in inset of (b).

Figure 8.3(b) shows the variation of dielectric loss of $Zn_{1-x}Al_xO$ ($0 \leq x \leq 0.10$) at room temperature with frequency in the range 100 Hz – 2 MHz. The dielectric

loss dispersion exhibits a peak at a particular frequency (ω_p) for both undoped ZnO and AZO nanoparticles. This characteristic peak referred to relaxation peak, arises when the natural frequency of the localized dipole matches with the frequency of external applied ac electric field. Inset of **Figure 8.3(b)** shows that ω_p which is a measure of inverse of relaxation time (τ^{-1}) of Debye relaxation increases with Al^{3+} doping and becomes maximum ~ x =0.03.

Figure 8.4(a) indicates the variation of σ_{ac} of $Zn_{1-x}Al_xO$ ($0.0 \leq x \leq 0.10$) with frequency at room temperature. Inset of **Figure 8.4(a)** shows that the incorporation of Al^{3+} into ZnO lattice increases the σ_{ac} and becomes maximum at x = 0.03 beyond which it decreases.

Inclusion of Al^{3+} ions into Zn^{2+} site leads to increase of charge carriers which improve in conductivity for $x \leq 0.03$. Whereas, farther doping may reduce the oxygen vacancies partially and thus reduces the conductivity. At high frequency, charge carriers can easily move across grain boundary because of which conductivity increases. **Figure 8.4(b)** shows the variation of complex impedance with real impedance for different AZO samples. The nature of semi-circular curves indicates that capacitance and resistance of grain are in parallel. It is seen that the diameters of semi-circles decrease with x till x = 0.03 and increases thereafter. This diameter is a measure of the grain resistance approximately. Thus cole-cole plot also agrees well with the inference of conductivity measurements.

The dc conductivity (σ_{dc}) can be calculated from the power law relation [12]:

$$\sigma_{ac}(\omega, T) = \sigma_{dc}(T) + A(T)\omega^{s} \text{.....(8.4)}$$

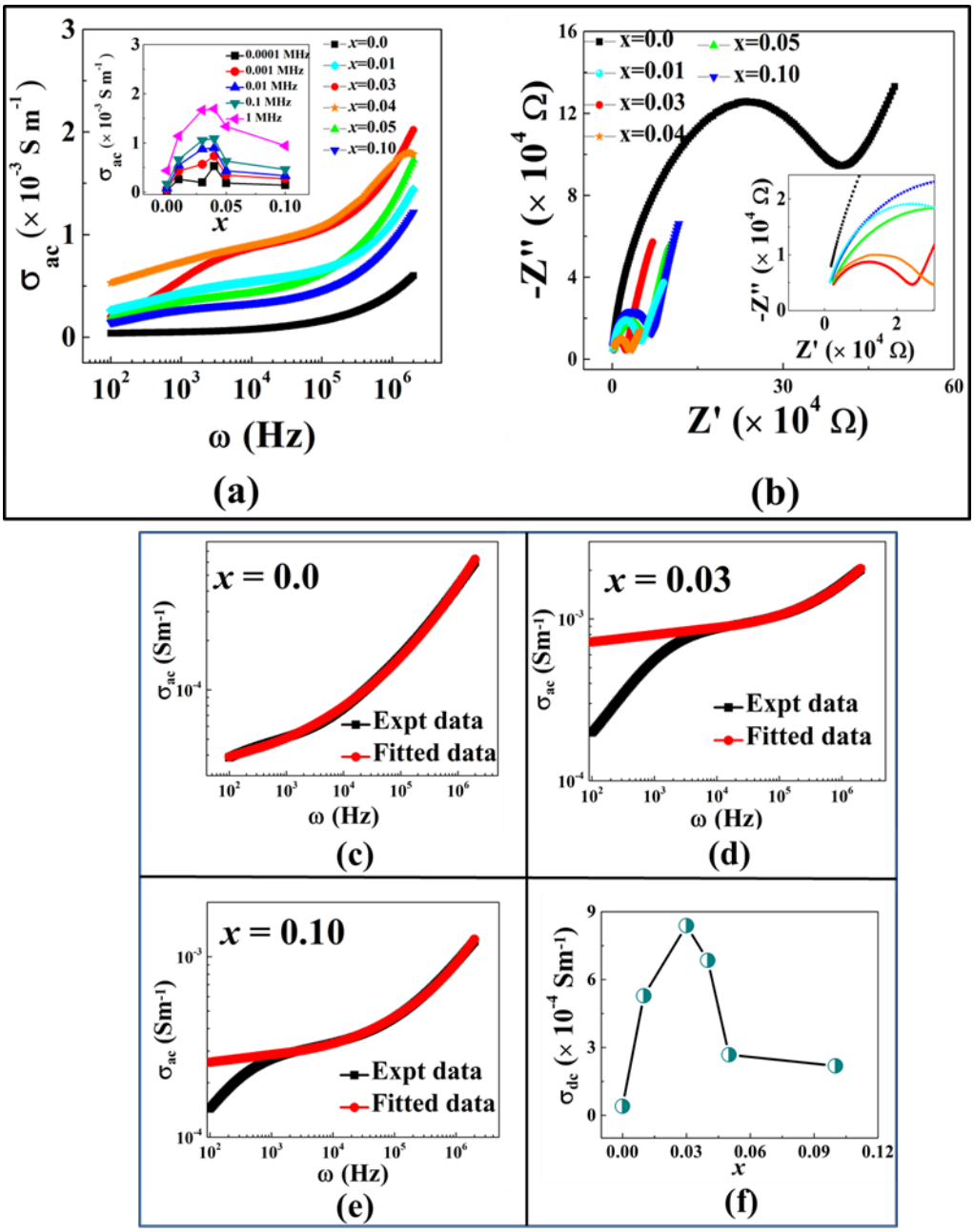

Figure 8.4: Variation of σ_{ac} with frequency are shown in (a) and with x are shown in inset of (a) for $Zn_{1-x}Al_xO$ ($0.0 \leq x \leq 0.10$), Z' vs –Z'' with its zoomed view are shown in (b), σ_{ac} vs ω plot fitted by power law for x = 0.0, 0.03, 0.10 are shown in (c), (d), (e) and σ_{dc} vs x is shown in (f).

This dc conductivity can be estimated by extrapolating the fitted curve of σ_{ac} vs ω plot. The best fitted curve of σ_{ac} vs ω is shown in **Figure 8.4(c), Figure 8.4(d),**

Figure 8.4(e) for x = 0.0, 0.03, 0.10 respectively. It is noteworthy that **Figure 8.4(f)** illustrates similar nature of variation of σ_{dc} with doping (x) as σ_{ac} and dielectric constant ε_R.

8.4 Conclusions

Al doped ZnO nanoparticles ($Zn_{1-x}Al_xO$) with different doping concentration $0 \leq x \leq 0.10$ have been synthesized by chemical precipitation method. X-ray diffraction studies of $Zn_{1-x}Al_xO$ confirm hexagonal Wurzite structure without any secondary phase formation. Dielectric studies at room temperature reveal the change of dielectric constant with Al^{3+} doping. 3% Al is found to be the optimum dopant concentration at which dielectric constant, ac conductivity and dc conductivity become maximum. Moreover, for x = 0.03 dielectric relaxation time becomes minimum. Beyond x = 0.03, doping of Al^{3+} may reduce the oxygen vacancy partially which in turn reduces the conductivity as well as dielectric constant and increase the relaxation time.

8.5 References

1. T. Minami, H. Nanto and S. Takata, Jpn. J. Appl. Phys. 23, L280-L282 (1984).
2. A. Sarkar, S. Ghosh, S. Chaudhuri and A. K. Pal, Thin Solid Films 204, 255-264 (1991).

3. J. Steinhauser, S. Faÿ, N. Oliveira, E. Vallat-Sauvain and C. Ballif, Appl. Phys. Lett. 90, 142107 (2007).
4. V. Bhosle, A. Tiwari and J. Narayan, J. Appl. Phys. 100, 033713 (2006).
5. K. Das, P. Misra and L. M. Kukreja, J. Phys. D: Appl. Phys. 42, 165405 (2009).
6. A. A. Al-Ghamdi, O. A. Al-Hartomy and M. El Okr, Spectrochimica Acta Part A: Molecular and Biomolecular Spectroscopy 131, 512–517 (2014).
7. S. Udayakumar, V. Renuka and K. Kavitha, Journal of Chemical and Pharmaceutical Research 4(2), 1271-1280 (2012).
8. G. K. Williamson and W. H. Hall, Acta Metall. 1, 22–31 (1953).
9. D. O. Neill, R. M. Bowman and J. M. Gregg, Appl.Phys.Lett. 77, 1520–1522 (2000).
10. M. K. Gupta and B. Kumar, J. Alloys and Compound 509, L208-L212 (2011).
11. R. Zamiri, A. Kaushal, A. Rebelo and J. M. F. Ferreira, Ceramics International 40, 1635-1639 (2014).
12. R. D. Gould and A. K. Hassan, Thin Solid Films 223, 334–340 (1993).

9 Exchange bias and Magnetic Memory effect in the hole doped $Nd_{0.78}Sr_{0.22}CoO_3$ nanoparticles

9.1 Introduction

The exchange bias effect (EB) is of great importance to promote potential applications in permanent magnet and high-density magnetic storage devices [1, 2]. Therefore, the phenomenon of exchange bias has been visited and revisited several times [3- 10] over the years, beginning with Meiklejohn and Bean (1956). The exchange bias effect appears due to the pinning mechanism at the interface between two magnetic components with significantly different anisotropy. The typical manifestation of the EB effect is the displacement of the magnetic hysteresis loop and the enhancement of coercivity due to magnetic field cooling effect. Numerous reports on EB phenomenon [3-11] are published for artificial interfaces in layered system and magnetic nanoparticles having distinguishable surface anisotropy from that of the core [12-14]. On the other hand, a handful systems having spontaneous magnetic phase separation within a single crystallographic phase exhibiting the EB phenomenon have also been reported. Mixed-valent manganites and cobaltites with perovskite structure are the most prevailing examples of this kind where ferromagnetic droplets are spontaneously embedded in an antiferromagnetic back ground or spin glass/cluster glass like

matrix or ferrimagnetic background creating spontaneous FM/AFM [15] or FM/SG (or CG) [16-17] or FM/FI [18] interface.

An interesting phase diagram has been proposed by Stauffer et al. [19] for the hole doped cobaltite $Nd_{1-x}Sr_xCoO_3$ for different degree of hole doping. In the low doping regime ($0 < x < 0.18$) the SG or CG state has been proposed as ground state. With further increase in hole doping ferrimagnetic (FI) and ferromagnetic (FM) ordering is observed in different temperature region for $0.20 \leq x \leq 0.60$.

In the present work we have restricted the doping of hole near the boundary of these two regimes and synthesized the hole doped $Nd_{0.78}Sr_{0.22}CoO_3$ nanoparticles whose features are expected to be noticeably different from its bulk counterpart [11, 20]. Nanoparticles exhibit the exotic features because of its surface anisotropy, large surface to volume ratio and particle size distribution [12]. The EB effect is found to be present in the perovskite $Nd_{0.78}Sr_{0.22}CoO_3$ nanoparticles which may arise because of the presence of two magnetic phases. The ZFC magnetization indicates ferromagnetic (FM) transition followed by a disordered magnetic phase with lowering of temperature even though ferrimagnetic ground state is expected [20] in the corresponding bulk counterpart. Magnetic memory effect found in this system corroborates the possible signature of disordered magnetic phase. Moreover, the large surface area of the nanoparticles promotes the uncompensated (UC) spin at the surface of nanoparticles which introduces different anisotropy in the system around 4.5 K. Coexistence of different

magnetic anisotropy contributes to the exchange bias effect. The temperature (T) and cooling field (H_{cool}) dependence of exchange bias field (H_{EB}) are in tune with the thermal variation of magnetization.

9.2 Experimental Details

9.2.1 Synthesis

$Nd_{1-x}Sr_xCoO_3$ with x = 0.22 is prepared by standard sol-gel technique [16, 18]. The Nd_2O_3, SrO and Co powder taken in stoichiometric ratio, are dissolved in hydrated nitric acid for preparing metal nitrate solution. Citric acid is then added in proper amount and the solution is stirred rigorously for two days in order to get homogeneous mixture. Proper amount of citric acid is estimated by considering that only two of the metal ions take part in chemical bonding with one molecule of citric acid. This metal citrate precursor is dried and annealed at 873 K for 6 hrs. The final heat treatment of the sample is done in the form of pellet in two steps at 1073 and 1273 K for 12 hrs followed by slow cooling at a rate of 0.7 K / min.

9.2.2 Characterization: Structural, Morphological and magnetization

Crystal structure is studied at room temperature using a powder X-ray diffractometer (XRD) (Bruker D8 Advance) with the Cu K_α radiation. Rietveld refinements were performed by using MAUD software. The full width at half

maximum (FWHM) of the most intense peak obtained from Rietveld refinements was used to calculate the average particle size. The morphology of the nanoparticles is studied by field emission scanning electron microscopy (FE-SEM) images using the microscope, JEOL (model: JSM-7610F). The particle size distribution in FESEM has been done by using Image-J software. The dc magnetization (M) is measured using a commercial vibrating sample magnetometer, 7T mini VSM, Cryogenics Ltd to study the magnetic properties of the sample. Magnetization (M) measurements as a function of temperature were carried out under the zero field cooled (ZFC) and field cooled (FC) mode. Furthermore, the slow relaxation dynamics and memory effects in the thermal variation of magnetization measured in ZFC protocol have been investigated. Temperature dependence of the FC magnetization were measured with an applied magnetic field of 100 Oe, while that of the ZFC magnetization were measured with an applied field of 100 and 200 Oe. The magnetic hysteresis (M-H) loops measured between ±70 kOe at different temperature in the range 2 K – 100 K under different cooling field in the range 2 kOe – 50 kOe.

9.3 Results and Discussions

9.3.1 Crystal structure and morphology: XRD and FESEM studies

The X-ray diffraction pattern of $Nd_{0.78}Sr_{0.22}CoO_3$ using CuK_α radiation is shown in **Figure 9.1**. All the peaks in the diffraction pattern could be indexed by the

orthorhombic structure as reported earlier [19, 21]. Thus, the XRD data confirm the absence of any detectable impurity phase and thereby the crystallographically single phase structure at room temperature is obtained. Rietveld refinement technique [22] is used to analyze the XRD data by assuming orthorhombic structure with Pnma space group and the lattice parameters are estimated as 5.36 (a), 7.58 (b) and 5.37 (c) Å which are consistent with that of earlier report [21]. The Rietveld refinement fitted graph of $Nd_{0.78}Sr_{0.22}CoO_3$ and the difference from the experimental data are shown in **Figure 9.1**. The particle size (*D*) and microstrain (ε) of $Nd_{0.78}Sr_{0.22}CoO_3$ nanoparticles are estimated by using Williamson and Hall's [23] modified Scherrer's formula given by

$$\beta \cos\theta = 0.89\lambda/D + 2\varepsilon \sin\theta \quad \text{.....(9.1),}$$

Taking under consideration of the prominent XRD peaks having uniquely defined FWHM a linear fit of $\beta \cos\theta$ versus $\sin\theta$ plot is shown in the inset of **Figure 9.1**. The average particle size and the microstrain (ε) of $Nd_{0.78}Sr_{0.22}CoO_3$ nanoparticles are estimated to be 89 nm and 3.26×10^{-3}, respectively. Morphology and size of $Nd_{0.78}Sr_{0.22}CoO_3$ nanopaticles are investigated from FESEM image as shown in **Figure 9.2**. Size of $Nd_{0.78}Sr_{0.22}CoO_3$ nanoparticles follows Gaussian distribution (inset of **Figure 9.2**) with maximum number of particles in the range around 92 nm which is consistent with the XRD results.

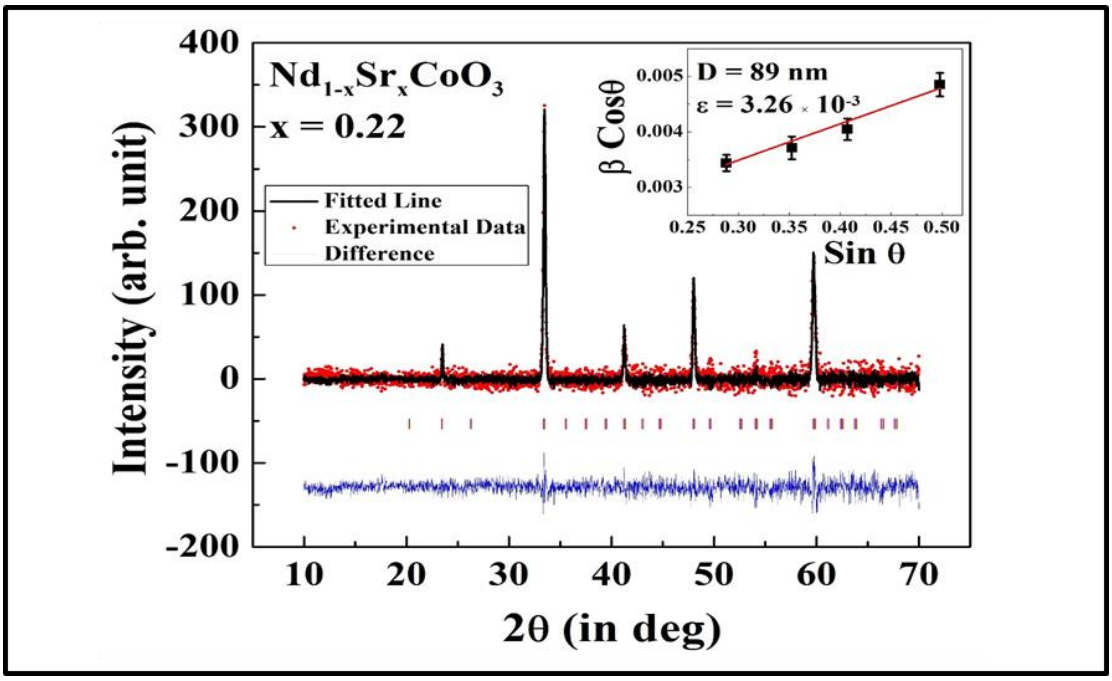

Figure 9.1: X-ray diffraction pattern of $Nd_{0.78}Sr_{0.22}CoO_3$ nanoparticles fitted with rietveld analysis. Inset shows Williamson-Hall plot.

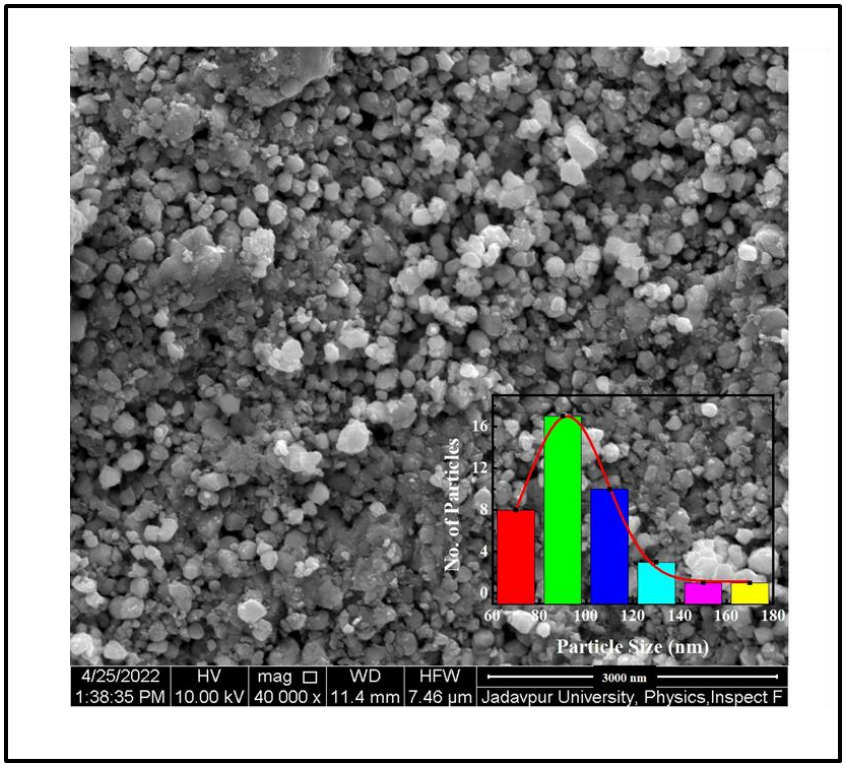

Figure 9.2: FESEM images of $Nd_{0.78}Sr_{0.22}CoO_3$ nanoparticles. Inset indicates the size distribution of $Nd_{0.78}Sr_{0.22}CoO_3$ nanoparticles following Lorentz distribution shown by continuous fitted line.

9.3.2 Magnetic Properties

9.3.2.1 Temperature dependence of dc magnetization

The magnetic properties of the $Nd_{0.78}Sr_{0.22}CoO_3$ nanoparticles are probed by dc magnetization studies. The temperature variation of magnetization (M) under the zero field cooled (ZFC) and field cooled (FC) protocol is shown in **Figure 9.3**. In order to measure ZFC magnetization, the sample is cooled down to 1.6 K in absence of magnetic field and the magnetization is measured in heating cycle at 100 Oe magnetic field. For the measurement in FC mode, the sample is cooled under the same field and magnetization is measured during heating from 1.6 K to 300 K. The FC magnetization deviates from ZFC magnetization around 155 K, as depicted in the figure by an arrow.

The thermal variation ZFC magnetization depicts a peak around ~36 K (T_g) followed by an upturn around 4.5 K as evident in **Figure 9.3 inset**. To reveal the origin of the ZFC peak, the temperature dependence of the ZFC magnetization is measured at different applied magnetic fields (H = 100 Oe and 200 Oe) as shown in **Figure 9.3 inset**. The peak at T_g is found to shift slightly toward the low temperature for higher magnetic field. Such a dependence of ZFC peak position on the magnetic field may designate the presence of a metastable state. It may be a signature of a disordered magnetic phase [13] although the reported experimental data including the neutron and ^{59}Co NMR clearly indicate the FI phases at low temperature in $Nd_{1-x}Sr_xCoO_3$ for $x \geq 0.20$ [21]. In the present case,

the disordered phase may arise because of the nanostructure of the system. The magnetic memory effect observed in this system measured in ZFC mode may be attributed to the disordered magnetic phase as discussed later in Section 9.3.2.2. A significant upturn in the ZFC magnetization below 4.5 K is illustrated in **Figure 9.3 inset** with decrease in temperature down to 1.6 K. This feature becomes more prominent with the increase of measuring magnetic field. This sharp increase of ZFC magnetization indicates the signature of a dominant ferromagnetic (FM) component in the low temperature region.

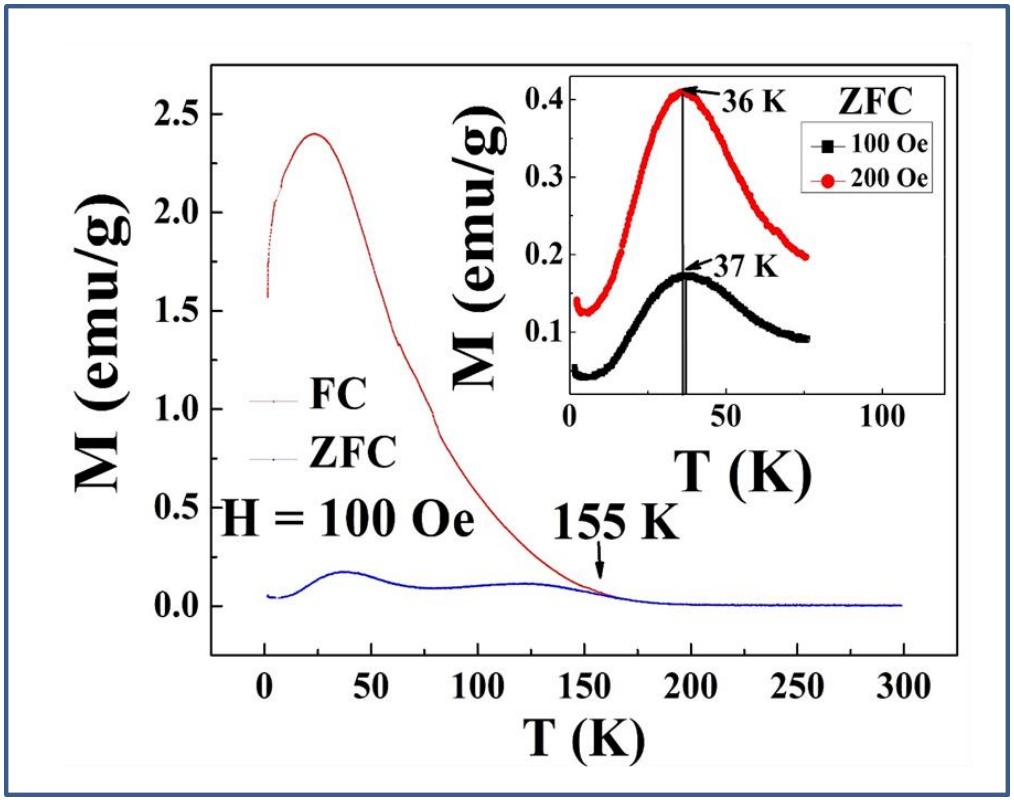

Figure 9.3: Thermal variation of the magnetization of $Nd_{0.78}Sr_{0.22}CoO_3$ nanoparticles measured in FC and ZFC mode at 100 Oe. Inset highlights the low temperature regime of ZFC magnetization measured at 100 Oe and 200 Oe as discussed in the text.

This FM component may be attributed to the uncompensated (UC) spins at the surface of $Nd_{0.78}Sr_{0.22}CoO_3$ nanoparticles as discussed in the recent reviews [24]. Appearance of UC-spins typically may bring in a new anisotropy which is different from the core anisotropy. Coexistence of different magnetic anisotropies leads to the exchange bias (EB) effect due to field cooling which is discussed later in the section 9.3.2.3.

9.3.2.2 Magnetic memory effect: characterization of disordered magnetic phase

The slow relaxation dynamics and memory effects in the thermal variation of magnetization measured in ZFC protocol are the ascertaining signatures of the disordered magnetic system. Memory effects observed in the relaxation dynamics are summarized in **Figure 9.4**. It illustrates the isothermal magnetic relaxation at 30 K recorded in 100 Oe for t_1 = 6000 sec after zero field cooling from 250 K which is well above the disorder transition (T_g) temperature. After lapse of t_1, the magnetic field is switched off, the temperature decreases down to 25 K and relaxation is measured again in zero field for t_2 = 6000 sec. Finally, the temperature is restored to 30 K in zero field and the relaxation is further recorded in 100 Oe for t_3 = 6000 sec. To explain the result, the magnetization measured during the aging period t1 and t3 is plotted sequentially in the inset of **Figure 9.5**, leaving out the data for time evolution during t2. Inset of **Figure 9.4** clearly indicates that the magnetization measured during the time period t_3 appears as a

perfect continuation to the curve measured during t_1. This clearly shows that state of the system before temporary cooling is recovered when temperature returns as if the system retains its memory of the previous state. This can be approximated by the stretched exponential function [25, 26],

$$M(t) = M_0 + M_g \left[1 - exp\left(-(t/t_0)\right)^{\beta}\right] \text{.....(9.2)}$$

Where, M_0 and M_g are involved with ferromagnetic and glassy components, respectively. t_0 is the time constant and the dispersion parameter β represents the distribution of relaxation dynamics.

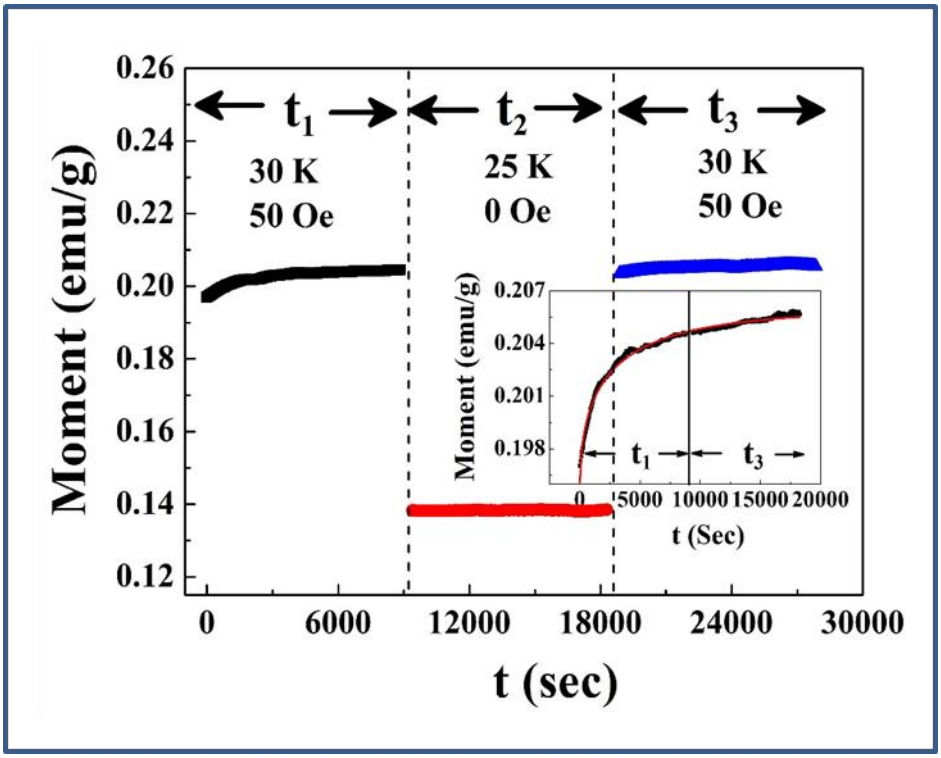

Figure 9.4: Magnetic relaxation at 30 K in 100 Oe for t_1 and t_3 after cooling down from 250 K in ZFC mode with an intermediate measurement time t_2 in zero field at 25K.

For single energy barrier the value of β is 1 whereas β value lies in the range $0 < \beta < 1$ for the system with distribution of energy barriers. Here, the best fit gives

M_0 = 0.19609 emu/g and β = 0.553, as shown in inset of **Figure 9.4**. The non-zero value of M_0 indicates the presence of ferromagnetic component [25, 26] attached in the relaxation dynamics and value of β points the distribution of anisotropy barriers, as generally found in disordered magnetic systems.

9.3.2.3 Exchange Bias Effect

To investigate the exchange bias (EB) effect sample is cooled down to 2 K from 300 K under different cooling field (H_{cool}) ranging from 2 kOe – 50 kOe. Magnetic hysteresis (M-H) loops measured between ±7 T at different temperature in the range 2 K – 100 K, under H_{cool} = 50 kOe are shown in **Figure 9.5**. The shift of the magnetic hysteresis loop measured at 2K under H_{cool} = 2 kOe and 50 kOe as highlighted in the inset of **Figure 9.5**, is a typical manifestation of an exchange bias effect. The shift along the field-axis defined as the exchange bias field (H_{EB}) and the coercive field (H_c) have been estimated as $H_{EB} = (H_C^+ + H_C^-)/2$ and $H_C = (H_C^+ - H_C^-)/2$ respectively, where H_C^+ (H_C^-) represents the positive (negative) coercive field. The remanence asymmetry defined as EB magnetization (M_{EB}) [18] is also calculated as $M_{EB} = (M_E^+ + M_E^-)/2$, where M_E^+ (M_E^-) represents positive (negative) remanent magnetization. M_{EB}/M_S estimated at 2 K for H_{cool} = 50 kOe is $\sim 0.5 \times 10^{-2}$, where M_S is the saturation of magnetization. This value is comparable to that of $Nd_{0.80}Sr_{0.2}CoO_3$ [18]. Thermal variation of H_{EB}, M_{EB}/M_S and H_C measured under H_{cool} = 50 kOe are shown in **Figure 9.6**. With the lowering of temperature H_{EB} increases sharply exhibiting highest value at 2 K as

uncompensated (UC) FM phase is observed below 4.5 K. Temperature dependence of the asymmetry parameters are typical for the exchange biased systems viz., $Nd_{1-x}Sr_xCoO_3$, where EB effect vanishes above FI or spin freezing transition temperature [18, 19]. In the present system, the rigid UC spins apply a coupling force on the disordered spins at the interface and a layer of pinned or frozen FM spins are created at the interface when the system is cooled in non-zero field. The pinned or frozen FM spins give rise to the unidirectional shift of the hysteresis loops and reveal the EB effect. Thermal variation of M_{EB}/M_S is similar to that of H_{EB} as expected.

The H_{cool} dependence of H_{EB} and M_{EB}/M_S are shown in the **Figure 9.7**. The value of H_{EB} increases sharply with H_{cool} up to 10 kOe and then linearly increases till 50 kOe. H_{cool} dependence of H_C, as seen in the inset of **Figure 9.7(a)** is almost similar to that of H_{EB}, where the sharp increase of H_C is associated with the increase of H_{EB}. Moreover, the inset of **Figure 9.7(b)** depicts the linear dependence of M_{EB}/M_S with H_{EB} as reported in bulk $Nd_{0.78}Sr_{0.22}CoO_3$[18]. The coexistence of two different magnetic phase viz. FM/FI interface was responsible for exhibiting the exchange bias effect in the bulk $Nd_{0.80}Sr_{0.2}CoO_3$ system [18], while the cause of exhibiting the same effect in $Nd_{0.78}Sr_{0.22}CoO_3$ nanoparticles is entirely different. Detail dc magnetization studies along with memory effect suggest the existence of UC spins at the surface of the nanoparticles below 4.5 K and magnetic disordered phase below 36 K. The interface of these two magnetic

phases with different anisotropy illustrates the exchange bias effect at low temperature in the nanoparticle of $Nd_{0.78}Sr_{0.22}CoO_3$. This exchange bias effect may be tuned by controlling the size and shape of the nanoparticles as UC spin are residing at the surface of the nanoparticles.

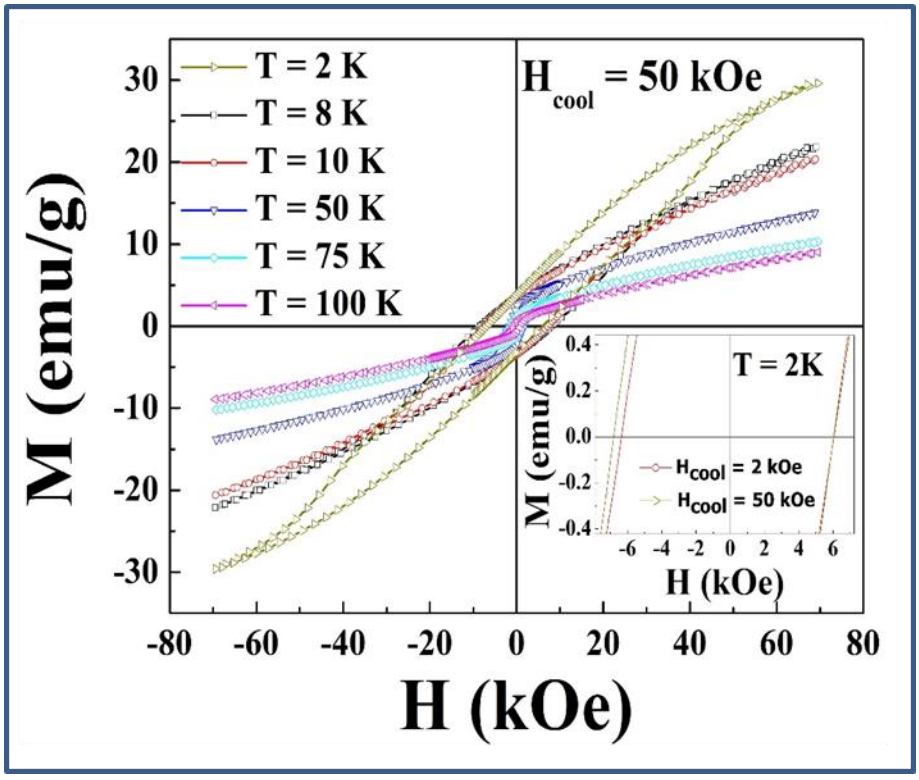

Figure 9.5: Magnetic hysteresis loops measured at 2 K, 8 K, 10 K, 50 K, 75 K and 100 K after cooling the sample from 300 K under H_{cool}= 50 kOe. Inset highlights the shift of central part of M–H loop measured at 2K under the cooling field H_{cool} = 2 kOe and 50 kOe.

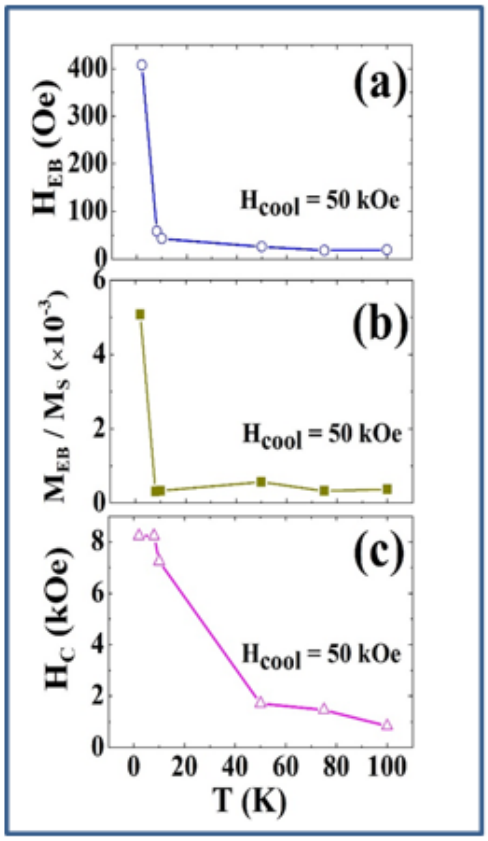

[Fig. 9.6]

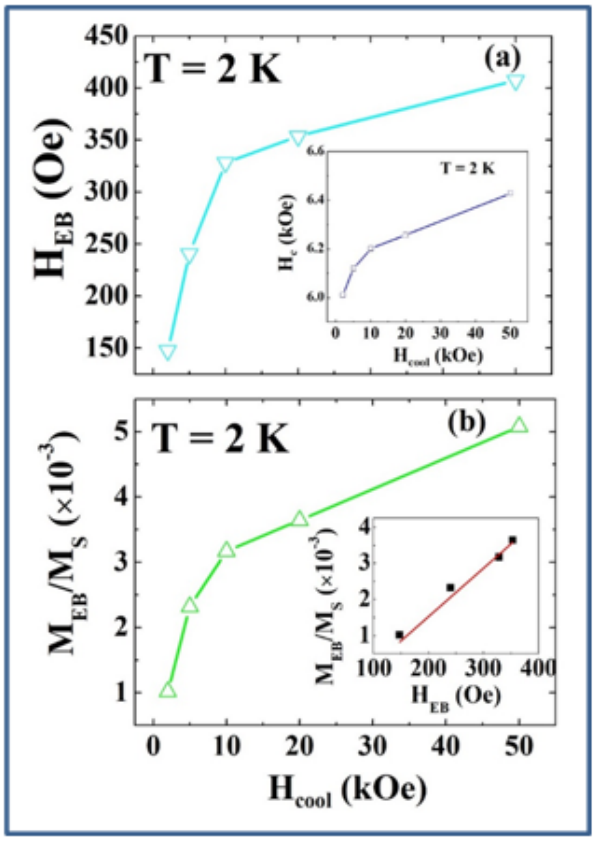

[Fig. 9.7]

Figure 9.6: Thermal variation of (a) exchange bias field (H_{EB}) (b) relative vertical shift (M_{EB}/M_S) and (c) coercivity (H_C) of $Nd_{0.78}Sr_{0.22}CoO_3$ nanoparticles measured under cooling field H_{cool} = 50 kOe. M_{EB} and M_S are the exchange bias magnetization and saturation magnetization.

Figure 9.7: Cooling field (H_{cool}) dependence of (a) exchange bias field (H_{EB}) and (b) relative vertical shift (M_{EB}/M_S) of $Nd_{0.78}Sr_{0.22}CoO_3$ nanoparticles measured at 2 K. Solid lines represent the guide line to eye. The H_{cool} dependence of coercivity (H_C) and the plot of M_{EB}/M_S versus H_{EB} are shown in the inset of (a) and (b), respectively. The solid straight line in the inset of the (b) shows the linear fit.

9.4 Conclusions

Hole doped $Nd_{0.80}Sr_{0.2}CoO_3$ nanoparticles are synthesized by sol-gel citrate precursor technique. Structural and morphological characterizations performed by X-ray diffraction and FESEM images reveal the average size of the

nanoparticles of ~ 89 nm. The thermal variation ZFC magnetization reveals a disordered magnetic phase below ~36 K. This phase is corroborated by magnetic memory as observed at 30 K. This disordered phase may arise because of the nanostructure of the system. Further lowering of temperature down to 1.6 K illustrates a significant upturn in the ZFC magnetization below 4.5 K. This sharp enhancement of ZFC magnetization indicates the signature of a dominant ferromagnetic (FM) component which may be attributed to the uncompensated (UC) spins at the surface of $Nd_{0.78}Sr_{0.22}CoO_3$ nanoparticles. Occurrence of the UC-spins typically may bring in a new anisotropy which is different from the core anisotropy. Coexistence of the different magnetic anisotropies leads to the exchange bias effect. The exchange bias effect (H_{EB}) sharply increases with the lowering of temperature below 8 K as expected.

9.5 References

1. Review: F.S. Luborsky, Electro-Technology (Sept. 1962) 107.
2. M. Ohkoshi, K. Tamari, M. Harada, S. Honda and T. Kusuda, Microstructure and Exchange Anisotropy of Co-CoO Sputtered Films with Perpendicular Magnetization, *IEEE Transl. J. Magn. Jpn.*, 1985, **1**, 37-38.
3. W. H. Meiklejohn and C. P. Bean, New Magnetic Anisotropy, *Phys. Rev.*, 1956, **102**, 1413-1414.
4. R. L. Stamps, Mechanisms for Exchange Bias, *J. Phys. D: Appl. Phys.*, 2000, **33**, R247-R268.

5. M. Kiwi, Exchange Bias Theory, *J. Magn. Magn. Mater.*, 2001, **234**, 584-595.
6. J. Nogués, J. Sort, V. Langlais, V. Skumryev, S. Suriñach, J. S. Muñoz, and M. D. Baró, Exchange Bias in Nanostsructures, *Phys. Rep.*, 2005, **422**, 65-117.
7. J. Nogués, J. Sort, V. Langlais, V. Skumryev, S. Suriñach, J. S. Muñoz, and M. D. Baró, Exchange Bias in Ferromagnetic Nanoparticles Embedded in an Antiferromagnetic Matrix, *Int. J. Nanotechnol.*, 2005, **2**, 23-42.
8. J. Nogués and I. K. Schuller, Exchange Bias, *J. Magn. Magn. Mater.*, 1999, **192**, 203-232.
9. S. Giri, M. Patra and S. Majumdar, Exchange Bias Effect in Alloys and Compounds, *J. Phys.: Condens. Matt.*, 2011, **23,** 073201(23pp).
10. Xiao-xiong Wang, Shan Gao, Xu Yan, Qiang Li, Jucheng Zhang, Yun-ze Long, Ke-qing Ruan, and Xiao-guang Li, Giant spontaneous exchange bias obtained by tuning magnetic compensation in Samarium ferrite single crystal, *Phys. Chem. Chem. Phys.*, 2018, **20**, 3687-3693.
11. A. Punnoose, H. Magnone, M. S. Seehra and J. Bonevich, Bulk to Nanoscale Magnetism and Exchange Bias in CuO Nanoparticles, *Phys. Rev. B.*, 2001, **64**, 174420:1-8.

12. T. N. Shendruk, R. D. Desautels, B. W. Southern and J. Van. Lierop, The Effect of Surface Spin Disorder on the Magnetism of γ-Fe_2O_3 Nanoparticle Dispersions, *Nanotechnol.*, 2007, **18**, 455704(6pp).
13. S. Sarkar, A. Mondal , N. Giri and R. Ray, Spin Glass like Transition and the Exchange Bias Effect in Co_3O_4 Nanoparticles Anchored onto Graphene Sheets, *Phys. Chem. Chem. Phys.*, 2019, **21**, 260-267.
14. S. Das, N. Giri, S. Sarkar, A. Mondal, S. Majumdar, S. Giri and R. Ray, Uncompensated Grain Boundary Spin Driven Exchange Bias Effect in Granular NiO Film, *Solid State Commun*.**,** 2019, **298**, 113642(5pp).
15. T. Qian, G. Li, T. Zhang, T. F. Zhou, X. Q. Xiang, X. W. Kang and X. G. Li, Exchange Bias Tuned by Cooling Field in Phase Separated $Y_{0.2}Ca_{0.8}MnO_3$, *Appl. Phys. Lett.*, 2007, **90**, 012503-1-3.
16. K. De, R. Ray, R. N. Panda, S. Giri, H. Nakamura, and T. Kohara, The Effect of Fe Substitution on Magnetic and Transport Properties of $LaMnO_3$, *J. Magn. Magn. Mater.*, 2005, **288**, 339-346.
17. X. J. Liu, Z. Q. Li, A. Yu, M. L. Liu, W. R. Li, B. L. Li, P. Wu, H. L. Bai and E. Y. Jiang, Magnetic, Electrical Transport and Electron Spin Resonance Studies of Fe-doped Manganite $LaMn_{0.7}Fe_{0.3}O_{3+\delta}$, *J. Magn. Magn. Mater.*, 2007, **313**, 354-360.
18. M. Patra, M. Thakur, S. Majumdar and S. Giri, The Exchange Bias Effect in Phase Separated $Nd_{1-x}Sr_xCoO_3$ at the Spontaneous

Ferromagnetic/Ferrimagnetic Interface, *J. Phys.: Condens. Matt.*, 2009, **21**, 236004(8pp).

19. D. D. Stauffer and C. Leighton, Magnetic Phase Behavior of the Ferrimagnetic Doped Cobaltite $Nd_{1-x}Sr_xCoO_3$, *Phys. Rev. B.*, 2004, **70**, 214414-1-7.
20. N. A. Frey, S. Peng, K. Cheng and S. Sun, Magnetic Nanoparticles: Synthesis, Functionalization, and Applications in Bioimaging and Magnetic Energy Storage, *Chem. Soc. Rev.*, 2009, **38**, 2532-2542.
21. A. Ghoshray, B. Bandyopadhyay, K. Ghoshray, V. Morchshakov, K. Bärner, I. O. Troyanchuk, H. Nakamura, T. Kohara, G. Y. Liu and G. H. Rao, Phase separation in $Nd_{1-x}Sr_xCoO_3$ using ^{59}Co NMR, *Phys. Rev. B.*, 2004, **69**, 064424:1-8.
22. R. A. Young, "Introduction to the Rietveld method, In R. A. Young (ed.)", *The Rietveld Method*, Oxford University Press, New York, 1993, pp. 1–38.
23. P. Dutta, M. S. Seehra, S. Thota and J. Kumar, A comparative study of the magnetic properties of bulk and nanocrystalline Co_3O_4, *J. Phys.: Condens. Mat.*, 2008, **20**, 015218-1-8.
24. R. H. Kodama and A. E. Berkowitz, in *Surface Effects in Magnetic Nanoparticles*, edited by D. Fiorani, Springer US, Boston, MA, 2005, 189-216.

25. M. Ulrich, J. García-Otero, J. Rivas and A. Bunde, Slow relaxation in ferromagnetic nanoparticles: Indication of spin-glass behavior, Phys. Rev. B., 2003, **67**, 024416:1-4.

26. S. Biswas, Sk. Sabyasachi, A. Bhaumik and R. Ray, Magnetic Memory Effects in Fe/γ -Fe_2O_3 Nanostructures, *IEEE Trans. Magn.*, 2014, **50(3),** 2301107.

10 Summary and Conclusions

In summary, the dielectric, transport and magnetic properties are investigated for pure and doped metal oxides nanomaterial and films. The granular nickel oxide (NiO) film, Zn doped NiO ($Ni_{1-x}Zn_xO$) ($0 \leq x \leq 0.05$) film and 22% Sr doped $NdCoO_3$ ($Nd_{0.78}Sr_{0.22}CoO_3$) polycrystalline sample are prepared in order to investigate the magnetic properties such as exchange bias phenomena, training effect, etc. Dielectric and transport properties are studied for the semiconducting nanomaterials such as Al doped ZnO (AZO; $Zn_{1-x}Al_xO$; $0.0 \leq x \leq 0.10$) and Zn doped NiO ($Ni_{1-x}Zn_xO$) ($0 \leq x \leq 0.05$). Granular NiO and $Ni_{1-x}Zn_xO$ film are prepared by sol-gel dip-coating technique on a silicon wafer substrate, while the polycrystalline sample $Nd_{0.78}Sr_{0.22}CoO_3$ is prepared by chemical citrate route or sol-gel route. AZO ($Zn_{1-x}Al_xO$; $0.0 \leq x \leq 0.10$) and $Ni_{1-x}Zn_xO$ ($0.0 \leq x \leq 0.05$) nanoparticles are synthesized by chemical precipitation method.

Structural investigations of both the films (granular NiO and $Ni_{1-x}Zn_xO$) and polycrystalline ($Nd_{0.78}Sr_{0.22}CoO_3$) have been performed by X-ray diffraction (XRD). The surface topology of films (NiO and $Ni_{1-x}Zn_xO$) has been probed by atomic force microscopy (AFM). The crystallite sizes obtained from AFM are found to be consistent with that of XRD studies for both the samples. For NiO film, thermal variation of zero field cooled (ZFC) magnetization measured at 500 Oe shows a broad peak around T_p = 156 K, which behaves like a blocking temperature of the weakly interacting antiferromagnetic nanoparticles or a spin-

glass like transition of the interacting antiferromagnetic nanoparticles. It should be pointed out that the absence of FC memory effect nullifies the possibility of spin glass state. A significant rise in thermal variation of FC and ZFC magnetization below 25 K infer the existence of FM component, which is due to the uncompensated (UC) spins residing at the grain boundaries. The systematic and significant shift in the magnetic hysteresis loops observed is basically the manifestation of exchange bias effect (EB). It is seen that the EB field varies significantly both with temperature as well as cooling field. It vanishes around 156 K (T_p), which is associated with the disappearance of coercivity. Since EB effect involves the pinning mechanism at the interface between two magnetic domains having significant difference in magnetic anisotropy, the vanishing EB effect around T_p indirectly indicates that the difference of magnetic anisotropy weakens above T_p. Training effect is also observed at 6 K which is analyzed by a recursive formula in the framework of spin configurational relaxation model. The observed exchange bias phenomenon in the granular NiO film is a rare consequence, which attracts the research community.

In case of $Ni_{1-x}Zn_xO$ film, thermal variation of FC and ZFC magnetization reveals the blocked state of $Ni_{0.95}Zn_{0.05}O$ below 155 K and the presence of uncompensated (UC) spins for $Ni_{0.97}Zn_{0.03}O$. The UC spin component may bring a new anisotropy which is quite different from the core anisotropy. The systematic shift of the magnetic hysteresis loop of $Ni_{1-x}Zn_xO$ film is measured in

field cooled mode, which is the fingerprint of exchange bias (EB) effect. It is found that the EB field depends strongly on the dopant (Zn) concentration *x* but not on the crystallite size. The formation of the granular film is an important observation where the granules can be realized as an assembly of nanoparticles of 16 nm average crystallite size for x=0.03. The pinning mechanism at the interface between antiferromagnetic core and shell consisting of uncompensated spins in the granular $Ni_{1-x}Zn_xO$ film is proposed in this work.

In case of hole doped $Nd_{0.78}Sr_{0.22}CoO_3$ nanoparticles, sample is synthesized by sol-gel citrate precursor technique. Structural and morphological characterizations performed by X-ray diffraction and FESEM images reveal the average size of the nanoparticles of ~ 89 nm. The thermal variation of ZFC magnetization reveals a disordered magnetic phase below ~36 K. This phase is corroborated by magnetic memory as observed at 30 K. This disordered phase may arise because of the nanostructure of the system. Further lowering of temperature down to 1.6 K illustrates a significant upturn in the ZFC magnetization below 4.5 K. This sharp enhancement of ZFC magnetization indicates the signature of a dominant ferromagnetic (FM) component which may be attributed to the uncompensated (UC) spins at the surface of $Nd_{0.78}Sr_{0.22}CoO_3$ nanoparticles. Occurrence of the UC-spins typically may bring in a new anisotropy which is different from the core anisotropy. Coexistence of the different magnetic anisotropies leads to the exchange bias effect. The exchange

bias effect (H_{EB}) sharply increases with the lowering of temperature below 8 K as expected.

AZO ($Zn_{1-x}Al_xO$; $0 \leq x \leq 0.10$) nanoparticles have been characterized by means of XRD method and FE-SEM. XRD studies confirm its hexagonal Wurtize structure without having any secondary phase formation. The grain size of AZO is found to be dependent on doping concentration. Ac conductivity (σ_{ac}), dielectric constant (ε_r) and dielectric loss (tan δ) are investigated as a function of frequency (ω) and doping concentration (x) at room temperature. It is found that the 3% Al is optimum dopant concentration at which dielectric constant, ac conductivity and dc conductivity become maximum. Moreover, the dielectric relaxation time becomes minimum for $x = 0.03$. Interestingly, it is also observed that increasing the doping concentration (beyond $x = 0.03$) of Al^{3+} may reduce the oxygen vacancy partially which in turn reduces the conductivity as well as dielectric constant and thereby increase the relaxation time.

The structural and morphological characterizations of $Ni_{1-x}Zn_xO$ ($0.0 \leq x \leq 0.05$) nanoparticle are executed by using XRD, FE-SEM and TEM. XRD results support the incorporation of Zn^{2+} into the NiO lattice either by the replacing of Ni^{2+} ion or by placing in the Ni^{2+} vacancy site. The size of the nanoparticles is found to be 26 nm and 22 nm for $x = 0.0$ and 0.05, respectively. It is seen that the average grain size decreases with Zn doping content (x). Optical band gap (E_g) has been estimated from UV-Vis measurement. Regular increase of the optical

band gap with increase in doping concentration (x) is observed which is consistent with the variation of particle size. AC conductivity (σ_{ac}), dielectric constant (ε_r) and dielectric loss (tan δ) of $Ni_{1-x}Zn_xO$ are studied as a function of frequency (f). It is observed that the dielectric constant (ε_r) increases gradually with x at high frequency (2 MHz). The dc conductivity (σ_{dc}) is found to decrease with Zn doping at room temperature. The reduction of σ_{dc} with increase in Zn^{2+} doping may be attributed to the reduction of oxygen vacancy via defect compensation mechanism. Temperature variation of σ_{dc} reveals the semiconducting nature with activation energy (E_a) 110.2 meV for x = 0.0; 384.14 meV and 88.19 meV in the temperature range 303-383K and 383-423 K, respectively, for x = 0.05. A crossover of dc conductivity (σ_{dc}) of $Ni_{0.95}Zn_{0.05}O$ to that of NiO is observed at 383 K. This cross over may indicate the lowering of barrier at the grain boundaries facilitating the charge transport. The temperature dependence of dielectric properties for x = 0.00 and 0.05 are also investigated as a function of f. It is found that the dielectric loss decreases significantly with increase of dopant content (x) at high frequency. Enhancement of dielectric constant accompanied with lowering dielectric loss due to Zn doping makes $Ni_{0.95}Zn_{0.05}O$ a potential candidate for high frequency device as well as for the further miniaturization of microelectronics components in near future.

The science and technology of films and nanomaterials has created a great excitement and expectations. The polycrystalline like Sr doped cobaltates is one

of the important materials which can play an essential role in the development of magnetic electronic devices. Therefore, one can focus on $R_{1-x}A_xCoO3$ system with different rare earth metals (R = Gd, Yb, etc.) and various dopant (A = Ca, Y, etc.) in near future. It would also been interesting to fabricate the cobaltate film (instead of bulk) which acts as a promising thermoelectric material. Granular NiO and $Ni_{1-x}Zn_xO$ films have great importance in applications such as spin valve device, magneto-resistive sensors, etc. AZO nanomaterials can be used in optoelectronics device applications. $Ni_{1-x}Zn_xO$ nanoparticles are suitable for microelectronics device as well as high frequency device. It is to be pointed out that the dielectric properties of studied samples at higher temperature could play an important role in the potential applications of these materials in a wide verity of technologies.